November 2022

Dynamic Study of Inverter-based Resources in Weak Grids

Zhengyu Wang
University of South Florida

Dynamic Study of Inverter-based Resources in Weak Grids

by

Zhengyu Wang

A dissertation submitted in partial fulfillment
of the requirements for the degree of
Doctor of Philosophy
Department of Electrical Engineering
College of Engineering
University of South Florida

Major Professor: Lingling Fan, Ph.D.
Chung Seop Jeong, Ph.D.
Kaiqi Xiong, Ph.D.
Qiong Zhang, Ph.D.
Zhixin Miao, Ph.D.

Date of Approval:
November 21, 2022

Keywords: Renewable Energy Resources, Grid-Following Inverters, Dynamic Modeling,
Stability Analysis

Dedication

To my family, advisors, colleagues, and friends.

Acknowledgments

Firstly, I would like to express my gratitude to my advisor Dr. Lingling Fan for all the instruction, guidance, and support on research and teaching throughout the Ph.D. career of mine in the Smart Grid Power System Laboratory at the University of South Florida. It will not be possible for this work could be done without all of her efforts. I appreciate both Dr. Zhixin Miao and Dr. Lingling Fan for providing me with many opportunities to teach various courses, join different projects, and present in meetings and conferences. And all these experiences enrich the knowledge and skills of mine, which benefit me for life.

Secondly, I sincerely thank the rest of the committee members and chair: Dr. Chung Seop Jeong, Dr. Kaiqi Xiong, Dr. Qiong Zhang, and Dr. Zhenyu Wang for their comments, help, and efforts throughout the dissertation.

I would also like to thank all my colleagues since I joined the research group for all the assistance, support, and collaboration, in particular: Dr. Abdullah Alassaf, Dr. Li Bao, Dr. Minyue Ma, Dr. Miao Zhang, Dr. Mohammed Alqahtani, Dr. Yangkun Xu, Dr. Yin Li, Rabi Kar, Yi Zhou, Ratik Mittal, Rahul Ramakrishna, and Huazhao Ding. Wish you all the best.

Finally, I want to express my appreciation for the consistent understanding, encouragement, and support from my entire family, especially my father, my mother, and my wife.

Table of Contents

List of Tables

List of Figures

Abstract

As the main technology behind renewable energy resources, such as solar PV and wind turbines, inverter-based generation penetration is increasing aggressively. Besides the congestion concerns when interconnecting a large-scale inverter-based resource (IBR) into the power grid, stability issues are commonly existing. The stability events occur more frequently when the resources are in remote area because the transmission line is long and grid strength is weak. One of the most representative and widely observed phenomena of IBR instability is low-frequency oscillation. And this dissertation focuses on investigating the low-frequency oscillations of IBR in weak grids.

The main objectives of the investigation are: 1. capture various types of low-frequency oscillations from unstable IBR behaviors from simulation studies and hardware experiments; 2. conduct stability analysis to identify the root causes of the instability phenomena. For objective 1, test beds are implemented in the electromagnetic-transient (EMT) simulations and in the laboratory with hardware. For objective 2, a series of linear analyses are performed under different IBR operating scenarios.

Moreover, one additional topic is included in this dissertation. Flexible AC transmission (FACT) systems also adopt IBR technology to control the reactive power bank, such as static var compensator (SVC) and static synchronous compensator (STATCOM). Low-frequency oscillations are also observed in the FACT systems. Therefore, the oscillations and stability analysis of SVC are presented as an additional dynamic study example.

Chapter 1: Introduction

1.1 Objective

Renewable energy resources are more popular yet critical than ever due to the urge of reducing the pollution emission from conventional power plants. The penetration of renewables is increasing at a rocket speed world-widely, such as solar Photovoltaic energy, wind energy, and battery energy storage systems. Despite the utilized resources being different, the main technology is common, which is the inverter. Compared to conventional electric machine type of generators, the inverter-based resource (IBR) employs power electronics to convert dc voltage to ac for power delivery. The benefit of IBR is its flexibility in operation as its output can be easily manipulated by the controller. However, one clear disadvantage of IBR is being sensitive about grid operating conditions because of the lack of inertia, which reduces the tolerance of grid dynamics under contingencies and lowers the stability margin.

In addition, the land size of wind farms and solar PV farms is much larger than conventional power plants in order to reach similar generation level. Therefore, large-scale renewable energy resources are usually located in remote area, which are far away from load centers, such as cities or heavy industry load areas. Fig. 1.1 presents the wind farm locations in the state of Texas. To deliver power over such a long distance, long transmission lines are constructed. The longer the line is, the greater its impedance and power dissipation will be. Larger grid impedance reduces the short-circuit ratio (SCR), which indicates the grid strength is weakened. Stability issues of IBR appear more often in weak grid connections.

IBR instability phenomena in weak grid connections majorly includes sub-cycle subsynchronous oscillations (SSOs), over-voltage, and over current [6, 30–32, 41]. These mentioned weak grid stability challenges have been recognized as one of the most significant

concerns in the research and industry field of power systems. The mentioned system instability will not disappear or be fully resolved in the near future because of aggressively growing renewable energy business.

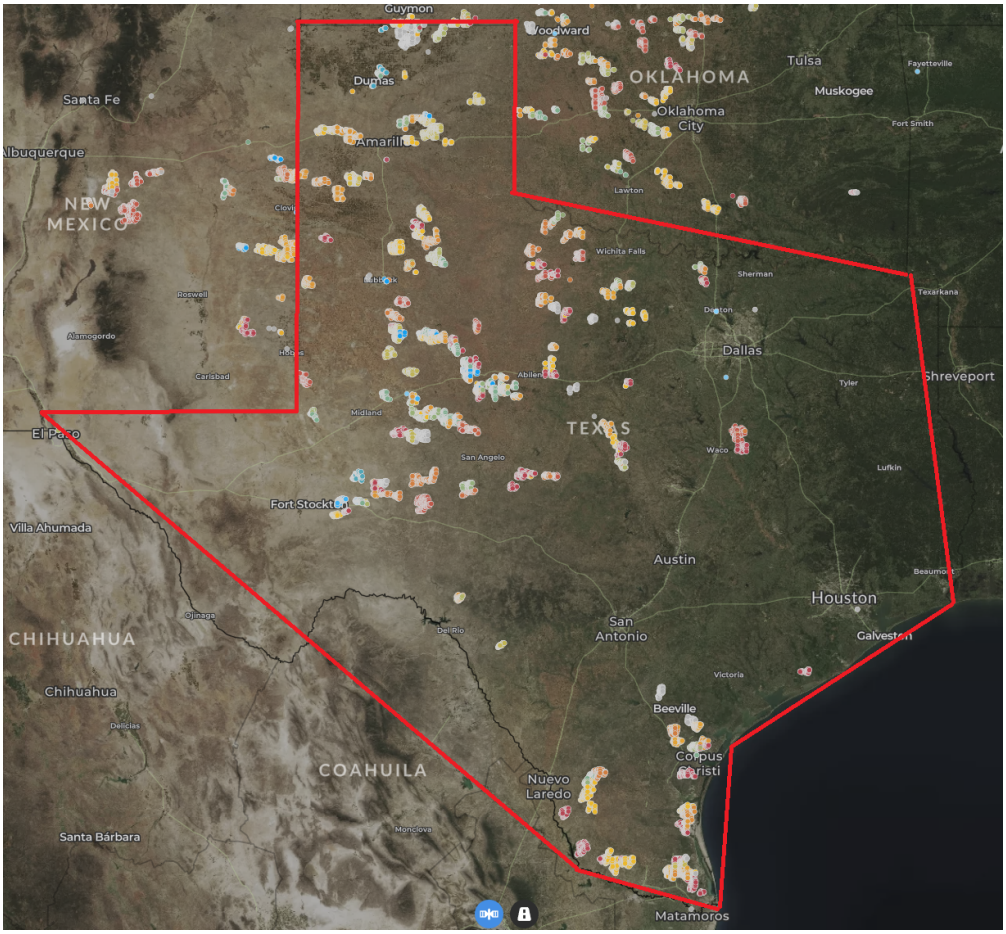

Figure 1.1: Wind farm location in the state of Texas.

Such transient stability phenomena cannot be studied via steady-state modeling or calculation, and it requires detailed dynamic studies, which is also the motivation of this dissertation work. The weak grid SSO of IBR-related dynamic study is the main focus of this dissertation. The work presented in this dissertation includes two major parts: (1) replicating or producing weak grid oscillations in various modeling environments within different test bed implementations; (2) conducting stability analysis of the system based on the developed analytical model. As an outcome, the critical causes of the instability issues are evaluated

and reported. Further, the guidelines to mitigate corresponding oscillation phenomena are also provided.

1.2 Research Approach

In order to explore the mechanism of the stability issue for grid-connected IBR systems, systematic research is conducted from searching for stability phenomena to learning the pattern, and further to the root cause identification. The overall procedure of the research approach used in this dissertation is discussed as follows.

First, the real-world oscillation events are replicated or emulated within the carried-out test beds, such as weak grid oscillation phenomena. While modeling, all the details of the system shall be filtered. But it needs to ensure that the critical dynamics are all included. In addition, the sensitivity study can be performed to conduct a rough look on the factor that greatly impact the system stability.

Second, the linear models to represent the test beds are essential to obtain so that various stability analyses can be performed later. To extract the linear model, two major approaches are applied and presented in this dissertation: 1. implementing a linear analytical model on dq-domain that includes all the dynamics; 2. directly extracting the linear models from measurements via designed input/output pairs. The advantage of method 1 is the derived analytical model is precise. However, such a model requires time-consuming building process and strict model initialization to guarantee flat-run. On the other hand, the measurement-based model extraction method is relatively easier to implement. But, the data treatment and model accuracy are complex. In this dissertation, both approaches are demonstrated and explained in detail.

Third, a series of stability analyses will be performed based on the obtained linear model, including but not limited to Eigenvalue-based analysis, Bode plot-based analysis, Root Locus-based analysis, etc. According to the analysis results, a further sensitivity study

is conducted to gradually approach the root cause of the system's dynamic behavior and trend of stability under corresponding events.

Last but not least, cross-validations between analysis and experiments are required. The system stability trend concluded from the analysis study should help predict the IBR's dynamic behaviors and patterns in the experiments. Verified research results shall be summarized afterward.

1.3 List of Publication

1. Z. Wang, L. Bao, L. Fan, Z. Miao, S. Shah, *From Event Data to Wind Power Plant DQ Admittance and Stability Risk Assessment*, IEEE Transactions on Power Systems, 2022

2. L. Fan, Z. Miao, Z. Wang, *A New Type of Weak Grid IBR Oscillations*, IEEE Transactions on Power Systems, 2022

3. L. Fan, Z. Wang, Z. Miao, S. Maslennikov, *Oscillation Source Detection for Inverter-Based Resources via Dissipative Energy Flow*, IEEE Power Engineering Letters, under review, 2022

4. Z. Wang, L. Fan, Z. Miao, *The Cause of Insufficient Damping in Phase-Locked Loop and its Influence*, IEEE PES General Meeting, submitted, 2022.

5. Z. Wang, L. Fan, Z. Miao, *Stability Analysis of Oscillations in SVCs*, 2022 North American Power Symposium (NAPS), 2022

6. Z. Wang, Z. Miao, L. Fan, *Practical Start-Up Process of Multiple Grid-Tied Voltage-Sourced Inverters in Laboratory*, 2021 North American Power Symposium (NAPS), 2021

7. L. Bao, L. Fan, Z. Miao, Z. Wang, *Hardware Demonstration of Weak Grid Oscillations in Grid-Following Converters*, 2021 North American Power Symposium (NAPS), 2021

8. Z. Wang, Z. Miao, L. Fan, A, Yazdani, *Weak Grid Operation of A Grid-Following Current-Sourced PV Solar System*, 2021 North American Power Symposium (NAPS), 2021

9. Y. Zhou, Z. Wang, Z. Miao, L. Fan, *A Synchrophasor-Based SCADA Testbed*, 2021 North American Power Symposium (NAPS), 2021

10. H. Ding, Z. Wang, L. Fan, Z. Miao, *Modeling and Control of Grid-Following Single-Phase Voltage-Sourced Converter*,2020 North American Power Symposium (NAPS), 2020

11. R. Kolla, Z. Wang, Z. Miao, L. Fan, *Realization of Enhanced Phase Locked Loop using Raspberry Pi and LabVIEW*,2019 North American Power Symposium (NAPS), 2019

12. Z. Wang, L. Fan, Z. Miao, *Data-Drive Dynamic Model Identification for Synchronous Generator*,2019 North American Power Symposium (NAPS), 2019

13. Z. Miao, L. Fan, M. Ma, Y. Li, Z. Wang, *Labs for EGN 3375 Electromechanical Energy Systems at University of South Florida*, 2018 North American Power Symposium (NAPS), 2018

14. Z. Wang, L. Fan, *Space Vector-Based Synchronous Machine Modeling*, 2017 North American Power Symposium (NAPS), 2017

1.4 Outline

The outline of the rest of this dissertation is provided as follows.

Chapter 2 discusses four types of modeling techniques introduced, including EMT simulation modeling, analytical modeling, measurement-based black-box modeling, as well as laboratory-scale hardware modeling. The fundamental study system and reflections in different modeling environments are described in detail. The start-up procedure of the hardware

test bed implemented in the lab is explained since the process is critical and helpful for the audience who will potentially work on similar topics.

Chapter 3 focuses on demonstrating the oscillation-based stability issue in a system with grid-connected IBR in weak grids. The dynamic study explores the weak grid oscillations in various test beds with different parameter setups. The captured oscillations are studied based on the developed analytical model, including implemented dq frame model and extracted linear models from designed event measurements. After, stability analysis is performed on the fine-tuned analytical model. The research outcome is concluded from the cross-validated stability analysis results.

Chapter 4 presents the stability issue in a FACT-integrated system. The oscillation in SVC connected to a long radial network is captured and studied. Instead of creating a complex analytical model, the measurement-based linear model extraction technique is shown to conduct stability analysis. Different analysis approaches have been taken, and the root cause of instability behaviors of SVC in weak grid connection is revealed.

Last but not least, Chapter 5 concludes the dissertation and indicates the future research work.

Chapter 2: Modeling of GFL IBR Integrated System

This chapter[1] presents the modeling techniques developed and applied in this dissertation work.

2.1 Introduction

Electric power system is one of the most critical infrastructures that the human race has built. It has to be huge to serve different types of loads located on entire continents. It has to be reliable to remain stable and deliver high-quality electricity for industrial production and residential life consistently. And it has to diversify to reduce pollution while providing enough power for growing demands. Therefore, it is sophisticated to build and maintain, and it is difficult to physically study. The scale and complexity make the power and energy topics different from other electrical engineering tracks.

Since it is hardly possible to build a power system to conduct IBR-related research and experiments, modeling technology becomes critical. Modeling is usually done in computer simulations or hardware test beds. IBR integrated system modeling is to translate real-world grid-connected IBR systems to various types of test beds in different environments. In this dissertation, all four types of modeling techniques are presented and utilized, including electromagnetic transient (EMT) simulation model in MATLAB/Simulink and PSCAD EMTDC, the analytical dynamic model, measurement-based admittance model, and laboratory-scale experimental hardware model. To visualize, Fig.2.1 shows the mentioned modeling types translated from an IBR-integrated power system.

[1]The majority of this chapter was published in IEEE Transactions on Sustainable Energy [11] and North American Power Symposium conference [44]. Permissions are included in Appendix A.

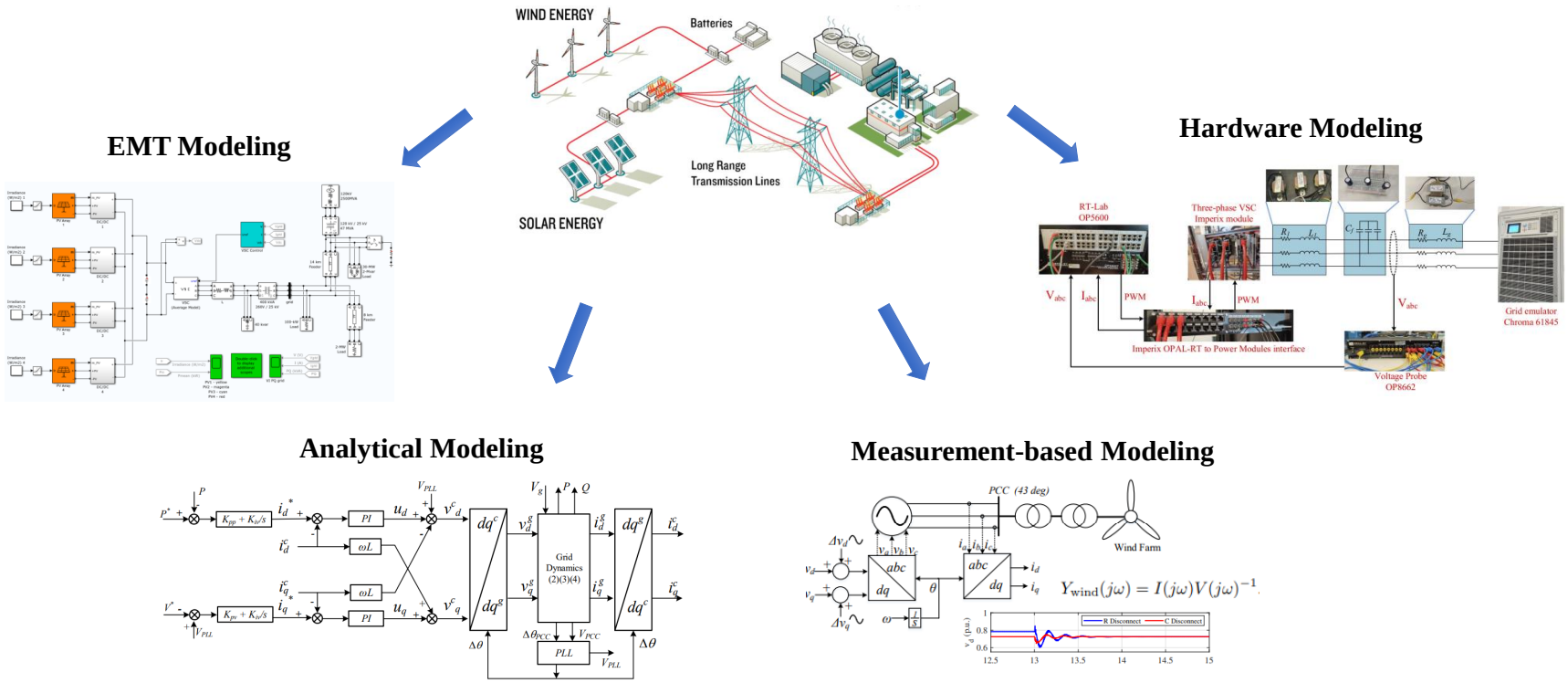

Figure 2.1: Translation of IBR integrated system into four types of models.

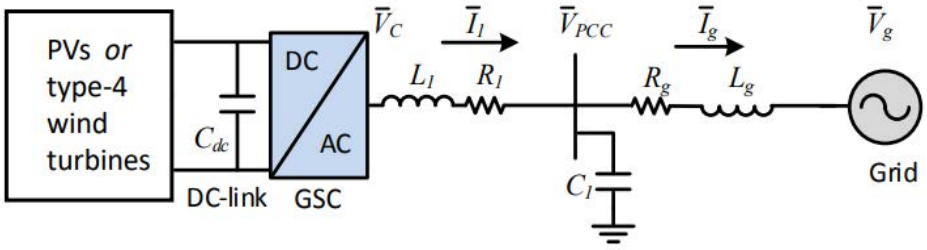

Figure 2.2: Topology of an aggregated IBR connected to the grid.

Among all mentioned modeling techniques, EMT simulation and hardware experiment are the most convincing study approach. However, EMT simulation includes three-phase signals which make the linearization impossible for stability analysis, and hardware experiment is even harder to predict the marginal operating condition. Therefore, analytical modeling and measurement-based modeling are the keys to exploring the inside of the system from research perspective.

Usually, when studying a utility-scale wind farm, solar PV, or battery storage energy system, many generating units with similar specifications are connected to the point of interconnection (POI) bus in parallel. And they are operated under the regulation of the controller. When the operating points of each individual unit are assumed to be identical, then all units can be aggregated as one IBR [36]. This assumption significantly simply the system complexity when modeling. The topology of the fundamental study test bed of one aggregated IBR connected to the grid is shown in Fig. 2.2.

Depending on the synchronization approach of grid-connected IBR, the control schemes are generally divided into two: grid-following (GFL) and grid-forming (GFM). The GFL control adopts a phase-locked loop (PLL) to realize the synchronization of the inverter to the grid voltage. And the GFM relies on the power measurement-based synchronization control (PSC), such as the strategy proposed in [48]. Although GFM has been investigated and indicated as a better alternative, GFL is still the dominate control scheme nowadays. This dissertation focuses on the GFL IBR integrated system dynamic modeling and study.

2.2 EMT Simulation Model

As previously mentioned in the research approach description, dynamic simulation modeling is opposite to steady-state power flow simulation modeling, where the transient behaviors in a short period of time can be captured for analysis. The electromagnetic-transient (EMT) modeling, in addition, is one type of dynamic modeling that covers more details in a wide frequency band, since all the dynamics from each component of the targeted system are included. The pros of the EMT simulation are precision, particulars, and comprehensiveness. And the cons are time-consuming, implementation difficulty, and black-box models with unknown structures. Thus, the EMT simulation model is implemented in the early research stage for exploring potential dynamic phenomena, as well as in the later stage for cross-validating analysis results. There are two major EMT simulations in the academic area: MATLAB/Simulink and PSCAD EMTDC. Both EMT simulation environments are applied in this dissertation work.

Following up the system topology in Fig. 2.2, a typical EMT simulation model must at least include a dc power source, a dc/ac inverter model, a grid voltage source, combinations of passive components, measurement units, and controller model. The listed components are described in the two subsections below.

2.2.1 Circuit Model

Fig. 2.3 shows a screen copy of an example EMT simulation model carried out in MATLAB/Simulink with SimPowerSystem Toolbox, which reflects the simplified grid-connected IBR system demonstrated in Fig. 2.2. A dc voltage source that represents the renewable generator terminal voltage is connected to the dc/ac inverter. The other side of the inverter terminal is three-phase outlet connects to the passive components. The voltage source on the rightmost is used to emulate the power grid as an infinite bus, which maintains voltage magnitude, frequency, and phase angle always unchanged and constant. In the middle of the circuit, a point of common coupling (PCC) bus is introduced to address the measure-

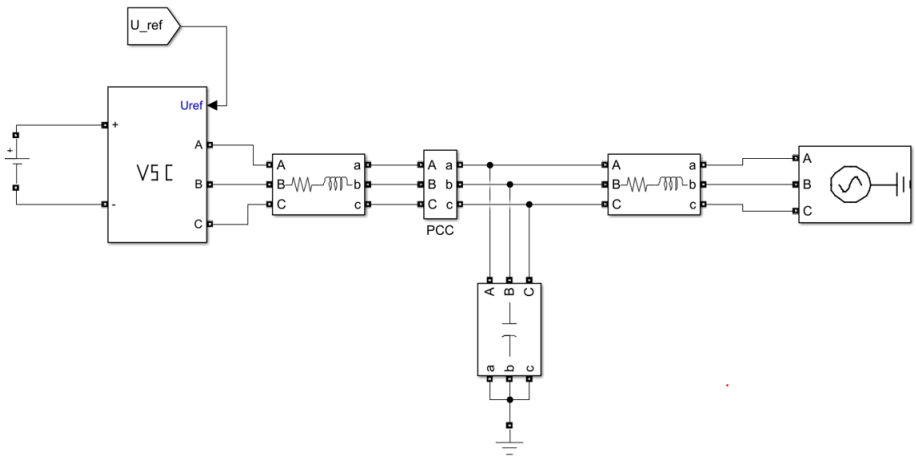

Figure 2.3: Screen copy of an example EMT simulation model.

ment point, as well as the location of the POI bus. The portion on the left-hand side of the PCC bus can be treated as the converter system. And the portion on the right is the transmission system. Between the inverter terminal and the PCC bus, the series-connected resistor and inductor are used to emulate the RL choke filter, where the resistance is usually assumed to be relatively small compared to the inductive impedance value. Between the grid voltage source and the PCC bus, the transmission line is represented by another pair of series-connected resistor and inductor. The R/X ratio that describes the relative sizes of the resistive and inductive impedance of the line is usually set to a smaller value to reduce the real power losses. A reasonable R/X ratio can be 10, for instance. The last piece of passive component is the capacitor connected to the PCC bus, which is also known as shunt compensation. It is implemented to provide voltage support by producing reactive power, and it can also help with system reliability and improve the power quality.

In the power system, engineers use per unit values for all system-level study and planning, where a power base (P_{base}) and a nominal line-line voltage (V_n) are required. Then the impedance base is obtained as $Z_{base} = \frac{v_n^2}{P_{base}}$, and then all passive components can be assigned accordingly. However, for all passive components in the EMT model carried out in MATLAB/Simulink, all values are real values instead of per-unit values. Therefore, the

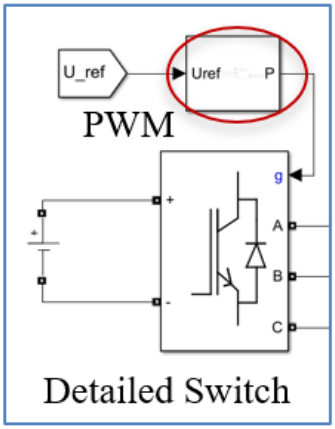

Figure 2.4: Detailed model of inverter block in EMT simulation test bed.

real values used in the EMT simulation model are computed based on the circuit design and designated bases.

On the other hand, the selection of an inverter model is important. In the EMT simulation modeling, we can choose to build a test bed with a detailed inverter model or an average inverter model. The inverter block shown in Fig. 2.3 is an average model inverter block. Fig. 2.4 presents the connection and symbol of the detailed inverter block.

There are two key differences between the detailed model and the average model: 1. detailed model contains all the dynamics from the power electronics inside, whereas the average model ignores the switching dynamics and performs as a pure controllable voltage source; 2. average model can be driven by three-phase reference signals that are generated from the controller, where the detailed switch inverter can only be driven by pulse-width waveform (PWM) gate signals. Hence, a PWM generator is required. Fig. 2.5 presents the PWM generation and comparison between three-phase terminal voltage measurements from the detailed inverter and average inverter model.

As shown in Fig. 2.5, the PWM gate signals are generated by comparing the three-phase ac reference signals from the controller to a triangle carrier waveform. When the reference signals are larger or smaller than the carrier, the switch will turn on and off. Besides, the switching frequency will also be reflected in the frequency of the triangle carrier waveform.

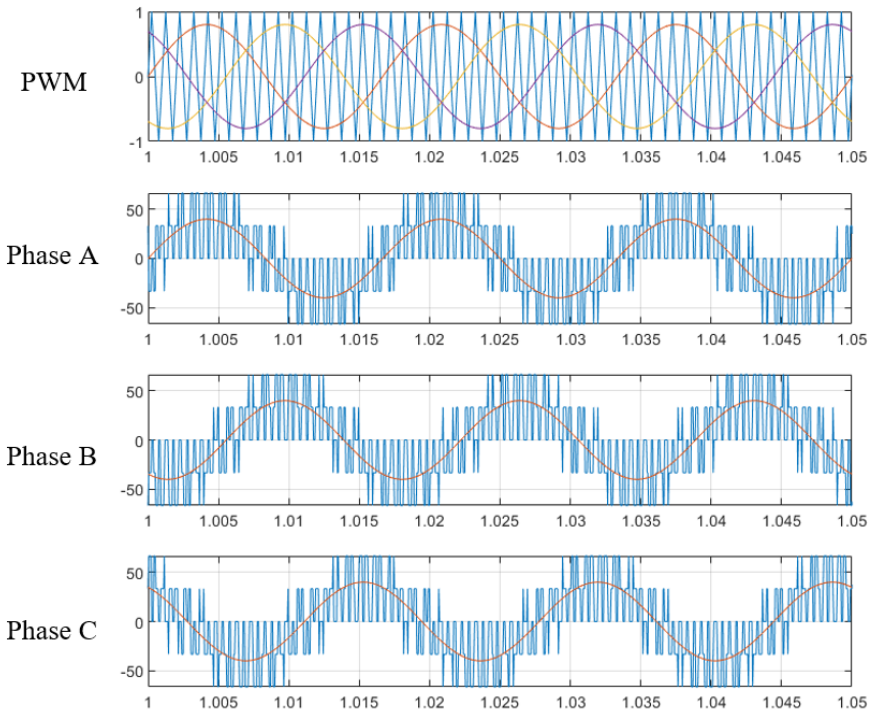

Figure 2.5: PWM generation and terminal voltage comparison.

The higher the switching frequency, the fewer noises the output will have. However, the downside is higher frequency leads to higher switching losses. For high-power utility-scale inverters, the switching frequency is usually under 10 kHz, depending on the power electronics type.

Fig. 2.5 also presents the terminal voltage comparison between the detailed and average inverter models. When balanced three-phase ac reference signals are provided, the average model terminal voltages are in phase with the reference signal with no distortion or harmonics. Oppositely, the detailed model terminal voltages are distorted and in a square wave shape. By plotting three-phase measurements together by phase, it is seen that the average model's output is the fundamental frequency components of the detailed inverter model's output.

In order to clearly address the switching dynamics at a high frequency in the detailed inverter model, the EMT simulation sampling step size must be small. As the average model

carries a lot fewer dynamics and does not require a high sampling rate, the average model takes significantly less amount of time to finish the same period of simulation compared to the detailed model. Thus, the average model is usually used in the first place to quickly examine certain scenarios and avoid the noises from the detailed switching dynamics.

Finally, the dc voltage to ac voltage magnitude converting principle is linear: $V_t = m\frac{V_{dc}}{2}$, where V_t is the single phase terminal voltage magnitude, m is the three-phase modulation (reference) signals, and V_{dc} is the dc voltage. The modulation index magnitude should be kept under 1 so that no over-modulation occurs. In Fig. 2.5, the modulation index is 0.8 and the dc voltage is 100 V. Therefore, the fundamental frequency component's magnitude and average model terminal voltage magnitude are identical to 40 V.

Last but not least, the dc side resource is indicated as PV or wind turbine in Fig. 2.2. The inverter that connected between the resource and transmission network is referred to the grid-side converter (GSC). Mostly, stability issues occur while operating GFL inverters due to the interactions from the grid to the GSC. A full dynamic test bed will include the dynamics in the PV, wind farm, or battery storage with additional components. In one of the later topics, a complete type-4 wind turbine test bed will be presented.

This is the end of the introduction to the circuit model.

2.2.2 Controller Model

The inverter controller is important when operating the grid-connected resources. A GFL inverter controller can be simply separated into two parts: synchronization and decoupled controller. And they are introduced in detail below.

2.2.2.1 Phase-Locked Loop

Different from GFM inverter control, the GFL inverter relies on a synchronization tool for the grid-tied operation, which is known as the phase-locked loop, PLL. As the grid is always alternating at 60 Hz with a time-varying phase angle at the POI, it is important to ensure

the inverter is synchronized with the grid. In an ac network, not only voltage magnitude differences between two nodes decide the current, but also the angle. In a two-bus lossless network, the real power that can be delivered is expressed as follows.

$$P_{12} = \frac{V_1 V_2}{X} \sin(\theta_{12}), \tag{2.1}$$

where P_{12} stands for the real power flows from bus 1 to bus 2, V_1 and V_2 are the bus voltage magnitudes, X is the line impedance, and θ_{12} is the angle difference between bus 1 and bus 2. In fact, in a large power system, the voltage magnitudes of two neighboring buses are very close to each other. And power flow can be adjusted by increasing or decreasing the angle difference instead. Although the theoretical transfer limit is achieved when the angle difference is 90 degrees, it should not be set to 90 degrees in the real world. Because the system will become sensitive and even collapse when the angle difference is too large. Therefore, the GFL controller needs sufficient synchronization to the grid at all times to avoid system instability and inrush current.

Phase-locked loop (PLL), a control system that tracks the input signal's phase angle, is deployed to synchronize the grid-following voltage source converter with the power grid. Fig. 2.6 presents the structure of a basic synchronous reference frame (SRF) PLL, where the superscript c stands for the PLL frame. It includes a Park's transformation block to extract the dq frame components [47], a PI controller to minimize the value of $q-axis$ component to generate frequency deviation, and an integrator that turn estimated frequency to phase angle. The input is the three-phase ac voltages measured at the point of the common coupling (PCC) bus, and the output is the extracted PCC bus voltage phase angle. At steady-state, $v^c_{\mathrm{PCC},d}$ is the voltage magnitude, and $v^c_{\mathrm{PCC},q}$ is 0.

Opposite to the PLL frame, a static grid reference frame is universal, and is built based on the grid voltage angle. Fig. 2.7 shows both dq frame. The benefit of having these virtual

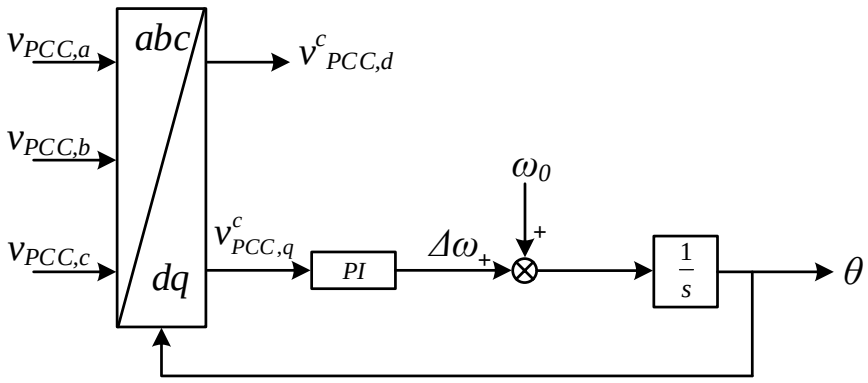

Figure 2.6: Block diagram of the SRF-PLL.

frames, the sinusoidal signals can be converted into dc values, which fits the PID-based controller scheme better.

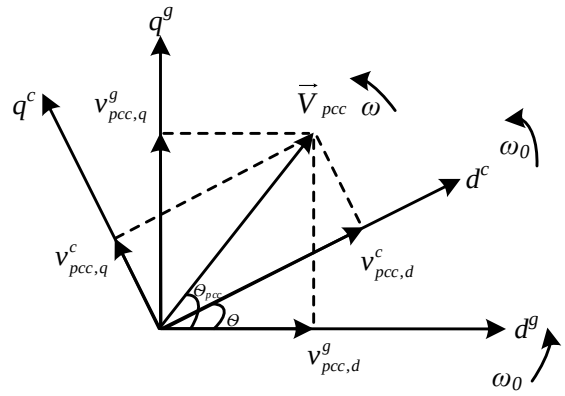

Figure 2.7: dq grid reference frame and PLL reference frame.

Based on Fig. 2.7, it shows the PLL frame in red catching up with the voltage phasor $\bar{v}$ by extracting the phase angle and minimizing the angle difference to the input. At steady-state, the $d-$axis fully assigned with the voltage phasor, which indicates both frequency and phase angle are identical to the PCC bus voltage. Then, the PLL frame is rotating with the voltage phasor and remains relatively static with it, so call locked.

The GFL control is mostly implemented based on the PLL frame. Thus, PLL should be the first layer of the controller. Appropriate PLL tuning is necessary. Fig. 2.8 presents the simple SRF-PLL frequency responses in the Bode plot with different control parameters. The blue curve indicates the SRF-PLL with a proportional gain of 60 and an integral gain

of 1400. And the orange curve addresses the SRF-PLL with a proportional gain of 20 and an integral gain of 467.

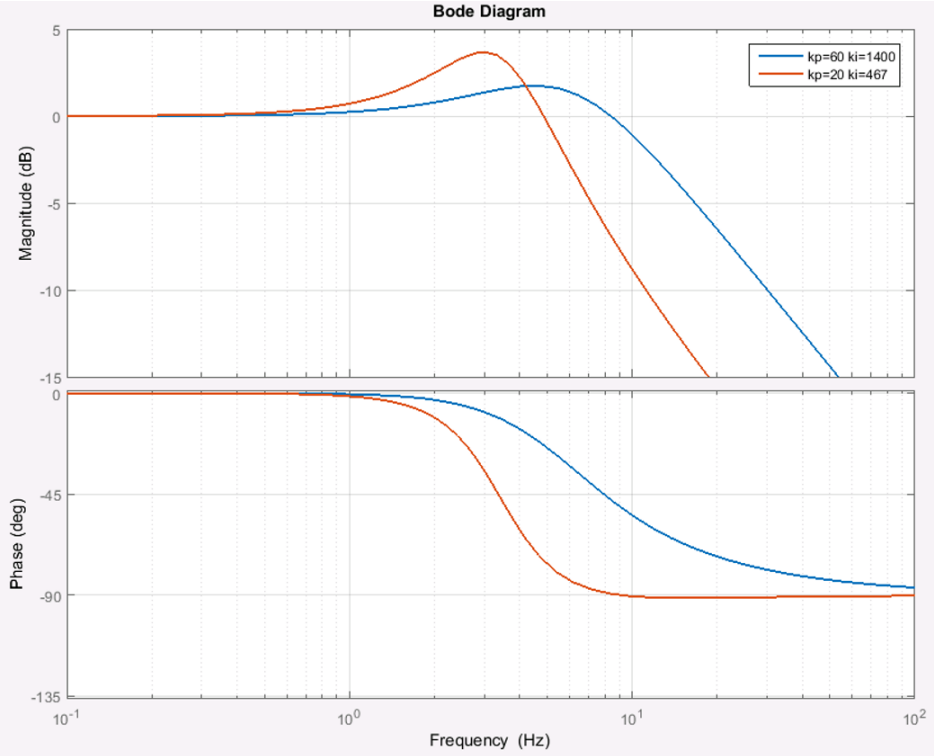

Figure 2.8: Bode plot of SRF-PLL with different bandwidth designs.

According to the frequency responses shown in Fig. 2.8, it is found that the larger control gain leads to higher bandwidth and lower peak in magnitude. High bandwidth indicates a poorer filtering capability. And low magnitude peak presents a better damping performance. To reflect the differences, the time-domain examination of both PLLs is taken and shown in Fig. 2.9. In the comparison, a step change is implemented in the input frequency, and 5^{th} order harmonics are added to the input magnitude.

From Fig. 2.9, it can be clearly observed that time-domain results align with the frequency response analysis described previously. It also addresses that the SRF-PLL does not have the capability to remove or suppress the harmonics. It can only smaller the harmonics' magnitude by lowering the bandwidth, but the side effect is poor damping. Changes made to the parameters only have limited influences.

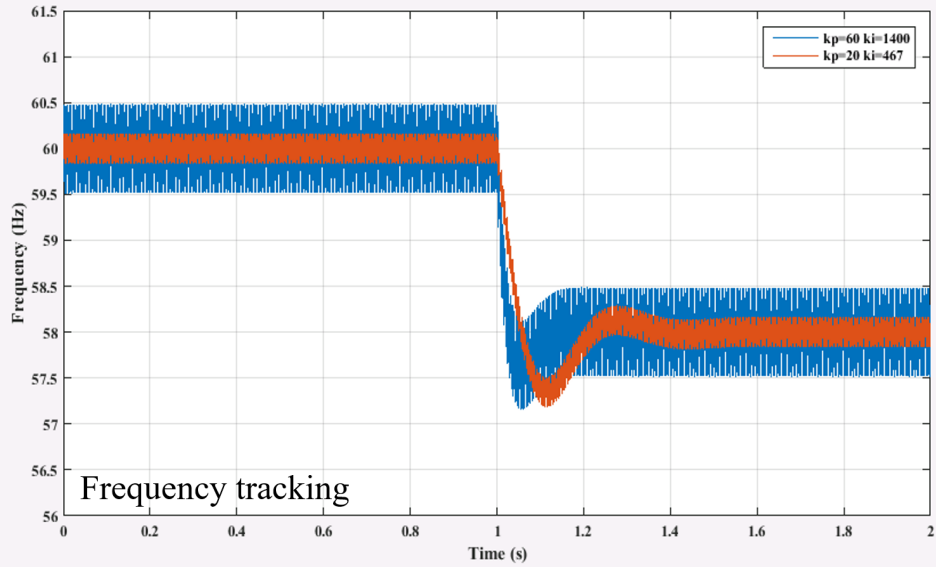

Figure 2.9: Time-domain results of PLL with different bandwidth under frequency step change.

In fact, the real-world PLL has a much more complicated structure that implements more filters to help deal with harmonics and noises. For instance, the three-phase PLL provided in MATLAB/Simulink SimPowerSystems toolbox has a sophisticated structure is shown in Fig. 2.10.

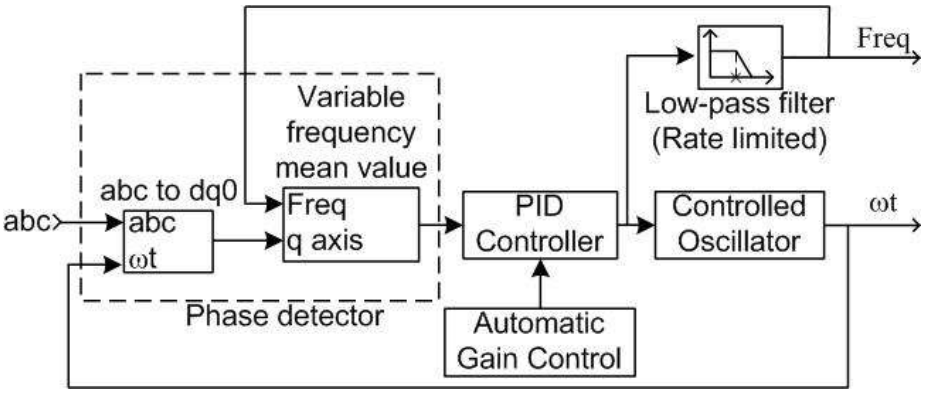

Figure 2.10: Topology of Simscape default three-phase PLL.

Compare to the SRF-PLL, the Simscape PLL structure shown in Fig. 2.10 includes an additional low-pass filter, variable frequency mean block, and automatic gain control. It presents the structure of the low-pass filter used by default, which combines a 2^{nd} order

low-pass filter, a unit delay, and a rate limiter. The damping ratio of the filter is 0.707, and the natural frequency is 25 Hz. The unit delay follows the simulation step size of 25 μs.

Fig. 2.11 presents a comparison of frequency tracking between Simscape PLL and SRF-PLL with identical control gain, where 5^{th} order harmonics are added to the input signals. According to Fig. 2.11, due to the lack of filtering, SRF-PLL tracks the frequency but has no regulation on the harmonics. Beyond, the damping performances are significantly different, where simple SRF-PLL shows better damping than Simscape PLL. Hence, the dynamic responses vary even with the same parameter setup. Moreover, since PLL is the first layer of the control scheme, it is critical to deploy a proper structure.

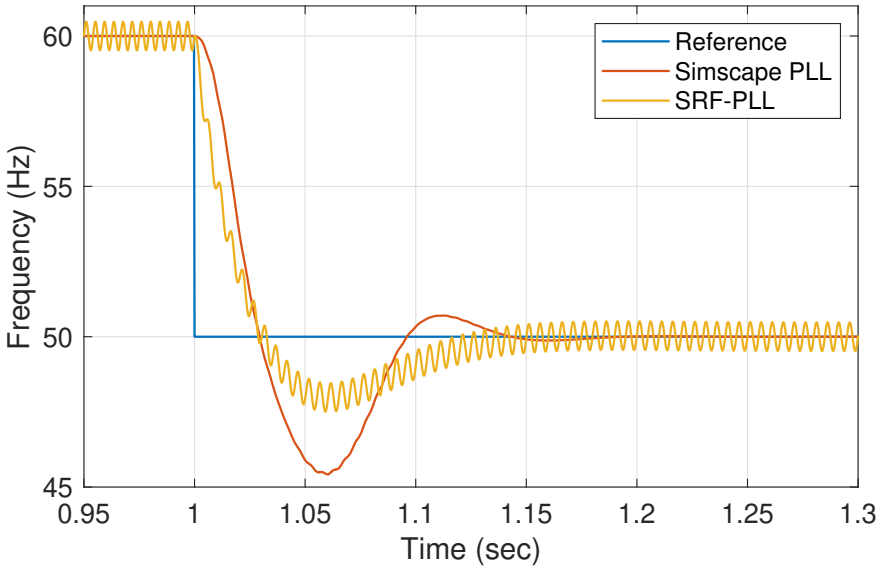

Figure 2.11: Comparison of frequency step response betweeen Simscape PLL and SRF-PLL with 5^{th} order harmonics in the input signal.

2.2.2.2 Vector Control

On the second layer of the controller scheme, there are different control logic can be applied. One of the most common control structures is shown in Fig. 2.12, which can regulate the real power output at the PCC bus and its ac voltage magnitude [47].

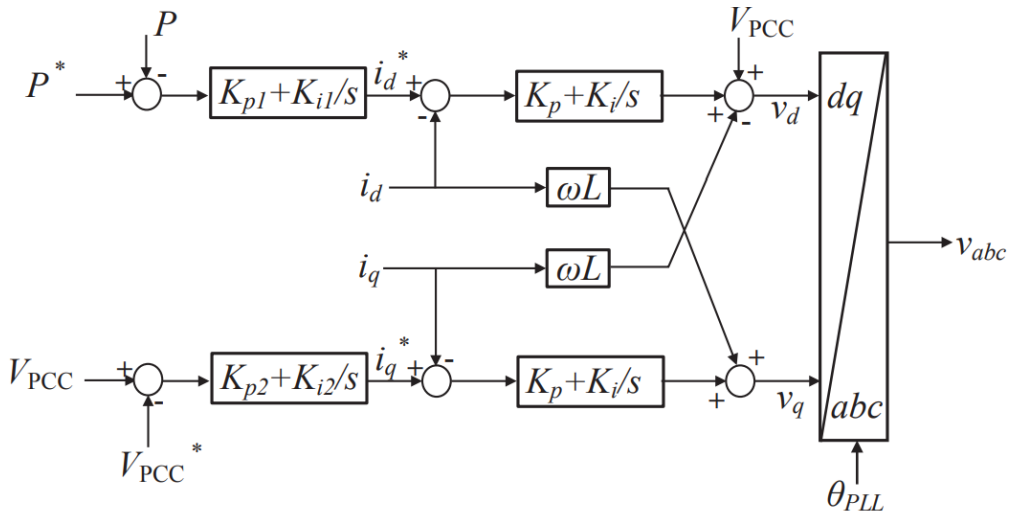

Figure 2.12: Real power and ac voltage control structure.

Such a control scheme has two controller loops: the inner current control loop and the outer vector control loop. The inner control is universal, PI controllers minimize the errors from comparing dq current references generated by the outer loop to the measurements. The output of current inner control will join the computation towards terminal voltage dq components before converting back to the grid reference for inverter control. The computation takes the dq voltage components at the PCC bus as feed-forward. Since the q-axis component at steady state is 0 on PLL reference PLL, it is not presented in Fig. 2.12. The computation also takes the cross-coupling values from choke filters' inductance dynamics, which are expressed on the grid reference frame as follows [11].

$$Ri_d^g + L\frac{di_d^g}{dt} - \omega_0 L i_q^g = v_d^g - V_{PCC,d}^g \tag{2.2}$$

$$Ri_q^g + L\frac{di_q^g}{dt} + \omega_0 L i_d^g = v_q^g - V_{PCC,q}^g, \tag{2.3}$$

where R and L are the choke filter's resistance and inductance. And this explains where the cross-coupling comes from.

Usually, the outer vector control can real power/ac voltage control or real/reactive power control. The equation below illustrates how real and reactive power can be controlled sep-

arately. It shows that real power can be adjusted by $d-$axis current control, and reactive power or voltage can be proportionally controlled by $q-$axis current control. As reactive power and i_q^c are negatively proportionally, it explains why the $q-$axis output control is positive feedback.

$$P = V_{PCC} i_d^c, Q = -V_{PCC} i_q^c \tag{2.4}$$

As aforementioned, the measurements used for the controller are taken at the PCC bus. The PCC bus voltage is used for synchronization, real and reactive power calculation, and control feed-forward. The current measurements are taken at the inverter terminal, which is the current flows into the PCC bus from the inverter. As result, Fig. 2.13 demonstrates time-domain simulation results of a GFL inverter following the control references. At 6 seconds, the real power reference was increased by 0.1 p.u. and the reactive power reference remains unchanged. The simulation measurements show that the real power measurement at the PCC bus can follow the command and increase the generation while keeping the reactive power output the same.

At this point, the introduction of EMT simulation modeling is complete.

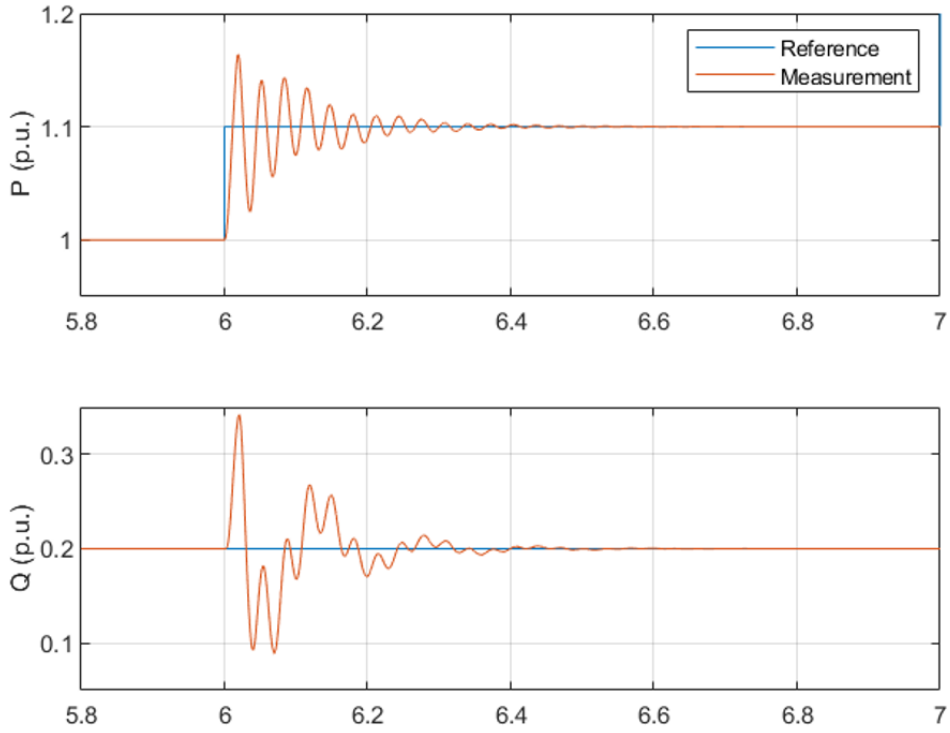

Figure 2.13: Example of GFL operation under real and reactive power control.

2.3 Analytical Dynamic Model

The test bed built in EMT simulation environment involves sinusoidal values, which cannot be used for linearization and further stability analysis. Therefore, an analytical model that replicates the major dynamics in the EMT simulation and is capable of being linearized is essential. In [11], such analytical model is introduced, which is implemented on dq frames only. The test bed structure is shown in Fig. 2.14.

There are two dq-frames involved: grid dq reference frame and PLL dq frame. A phasor diagram explaining the frame conversion is presented in Fig. 2.7. Superscription g and c represents the grid and PLL frames respectively.

Since the analytical model is fully built on dq frames, the conventional SRF-PLL structure needs to be modified to adapt to dq measurements instead of three-phase ac signals. Fig. 2.15 shows the block diagram of the second-order PLL modeled in the analytical model,

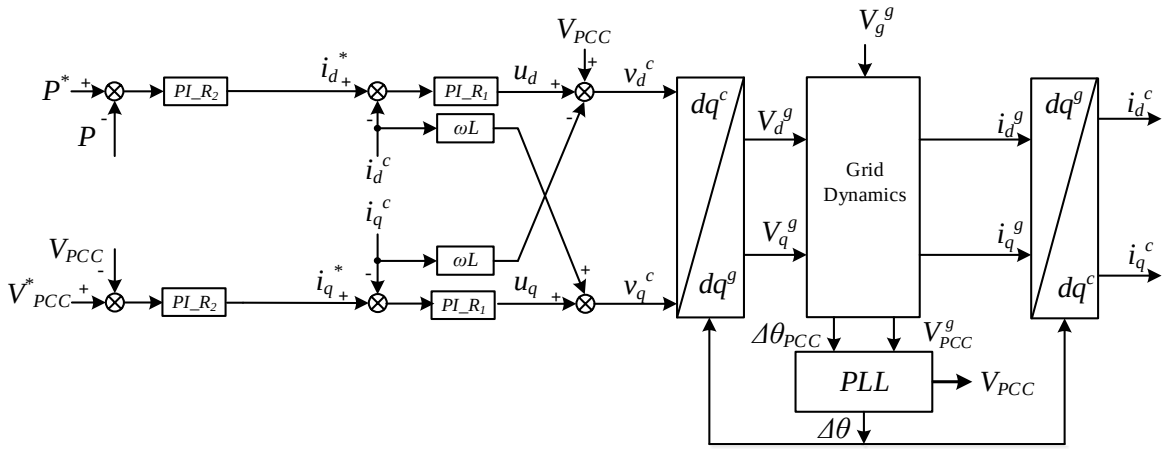

Figure 2.14: Block diagram of dq frame analytical model.

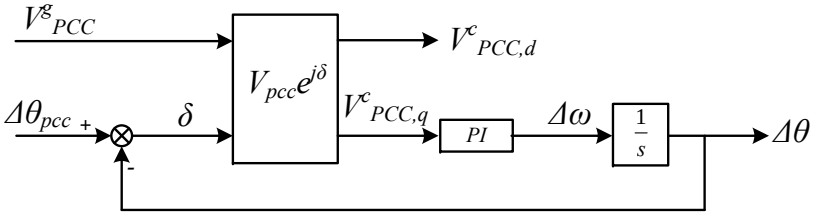

Figure 2.15: Block diagram of PLL in the analytical model.

where the control principle is to generate an angle to align with the angle of v_{PCC} phasor and regulate the $v^{\mathrm{c}}_{\mathrm{PCC,q}}$ value to be 0.

Besides the PLL structure change, no further change is required for the controller side. The grid dynamics are all modeled on the grid reference frame. Thus, the terminal voltage dq components are converted from PLL frame to grid frame, and the measurements are converted from grid frame to PLL frame. All the dynamic equations of the circuit are not presented in this dissertation work, and they can be found in [11].

Prior to perform model linearization, there are two more steps of procedure. First, it needs to be checked if the steady-state operating points are agreeing with the EMT simulation test bed. Second, the dq analytical model must be initialized in order to linearize. If the operating condition at the beginning of the simulation is not flat run, then linearization performed beyond this scenario is incorrect.

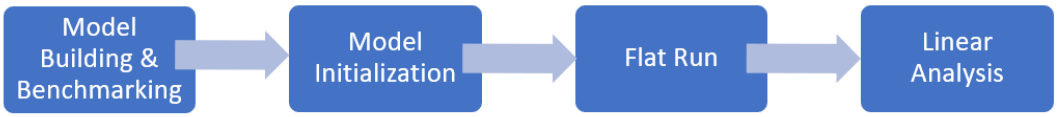

Figure 2.16: Analytical model study procedure.

To initialize the model, all the state variables are required to be assigned initial values correspond to the desired operating point. This step can be realized via iterative power flow calculation [26], such as the Newton-Raphson method, or by formulating a simple optimization problem to solve the circuit analysis [10]. After the analytical model is able to flat start, the state-space model can then be extracted from linearization. Finally, the stability analysis can be performed. Fig. 2.16 presents the study procedure flow chart of using analytical model.

2.4 Measurement-based Black-Box Model

Although the introduction of building analytical model is relatively short, it is still a time-consuming work. On the other hand, it is also difficult to construct a transparent analytical model as some of the IBR informaiton is not accessible, such as inverter-level control algorithms, control parameters, PLL structure, and etc. These setup information is critical when replicating real-world events and conducting further analysis. Therefore, black-box type of modeling technique is naturally adopted as an alternative. The relation from the input to the output of the system can be translated into a linear model in frequency-domain, such as impedance model and admittance model. And the input and output information are the measurements from the test bed or even real-world data records. Such modeling approach is the measurement-based black-box model.

Within fully compiled EMT simulation test bed, first step to approach to the black-box model is creating measurements. Such measurements can be dynamic event data [43], designed harmonics [49], and etc. Second is to obtain the frequency-domain model repre-

sentations. When applying dynamic event data, data fitting tools are required. If harmonic injection approach is taken, then the phasor measurements collected need to be organized and fitted to obtain $s-$domain expression, such as transfer function or state-space model. After evaluating the results, linear model-based stability analysis shall be performed for stability assessments.

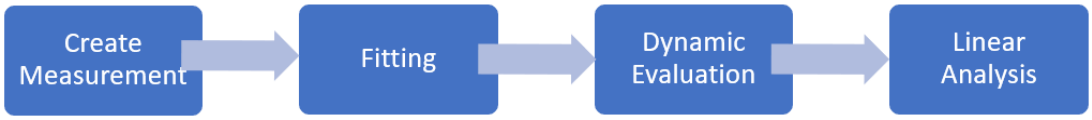

Figure 2.17: Measurement-based black-box model study procedure.

In this dissertation, dynamic event data-based black-box modeling approach will be demonstrated in the later chapter.

2.5 Laboratory-Scale Hardware Model

Hardware model is different from the modeling techniques introduced above, which requires to have hands-on experiences and skills. Putting all pieces of equipment to work together and presenting desired phenomena are much more complicated comparing to building dynamic models.

For physically producing weak grid oscillation stability events that are studied in the simulations before, a laboratory-scale hardware test bed is built. The implementation starts from a single IBR test bed that is similar to the topology shown in Fig. 2.2. Further, another test bed includes two identical inverters connected to the grid in parallel is implemented. The structure is shown in Fig. 2.18

In Fig. 2.18, two GFL inverters are installed to send power to the grid. On the dc side, two individual dc power supplies are directly connected to the DC-link capacitors. On the ac side, the output terminals build up the three-phase voltages and send currents across choke filters. Two current flows merge into one on the point of common coupling (PCC) bus. A

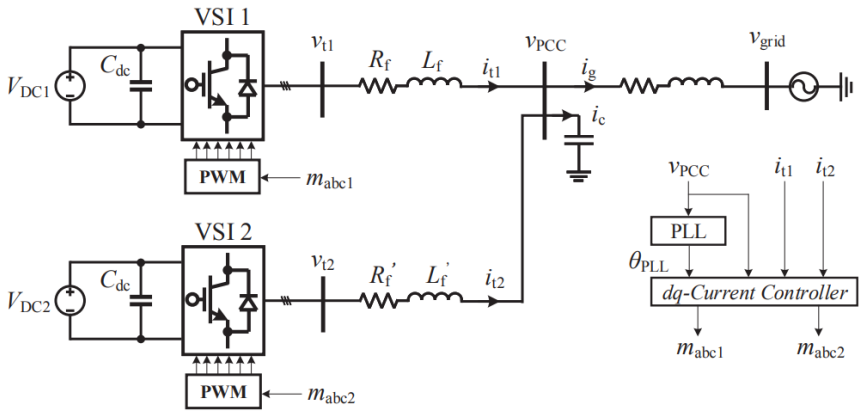

Figure 2.18: System topology single-line diagram.

shunt capacitor is connected to the PCC bus for filtering and reactive power compensation purposes. Three sets of series-connected resistor and inductor are deployed to represent the transmission line impedance.

Table 2.1: Parameters of the Hardware Testbed

Category	Description	Parameter	Value
System	Rated power	P_n	50 VA
	Rated voltage	V_n	20 V L-L RMS
	Nominal frequency	f_n	60 Hz
	DC voltage	V_{dc}	40 V
	Switching frequency	f_{sw}	5 kHz
Passives	Choke inductance	L_f	1.5 mH
	Choke resistance	R_f	70 mΩ
	Choke inductance	L_f'	2.5 mH
	Choke resistance	R_f'	44 mΩ
	Shunt capacitance	C_f	47 μF
	RL line inductance	L_g	1.5 mH
	RL line resistance	R_g	70 mΩ
Controller	Inner current control	$K_{p,I}, K_{i,I}$	1, 10
	Power control	$K_{p,P}, K_{i,P}$	0.25, 25
	AC voltage control	$K_{p,V}, K_{i,V}$	0.25, 25
	PLL	$K_{p,PLL}, K_{i,PLL}$	60, 1400
Filter	Low-pass filter time constant	T_s	5 ms

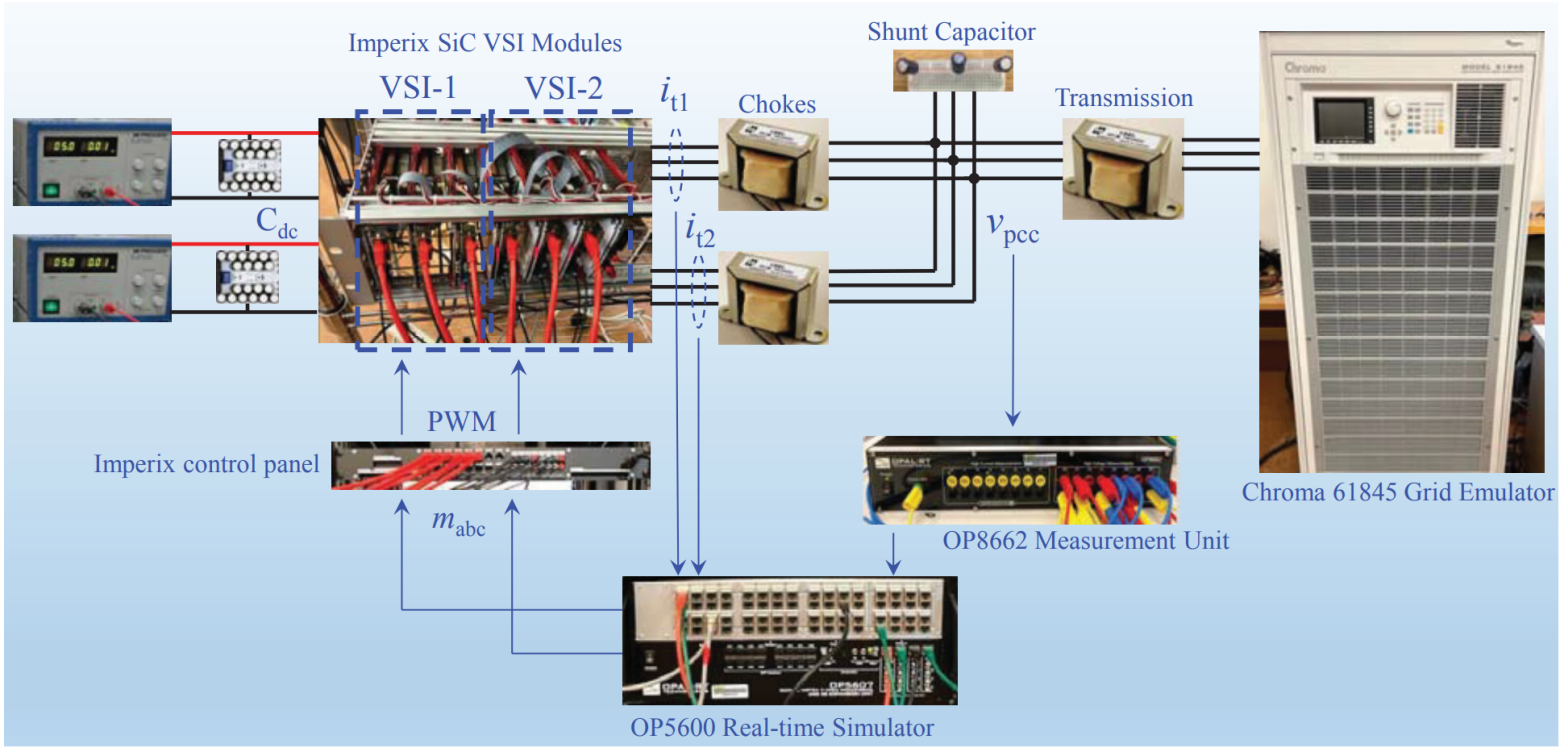

Figure 2.19: System topology single-line diagram.

Fig. 2.19 demonstrates the laboratory-scale system topology with corresponding devices. The dc power supplies connected are B&K Precision 1666 with maximum voltage of 40 V and current of 5 A. The power grid is implemented by Chroma Regenerative Grid Emulator 61845. Two sets of three-phase inverters are grouped by 6 individual Imperix's half-bridge Silicon Carbide (SiC) PEB-8024 power modules.

The terminal output current measurements are collected by the on-board current sensors of each SiC module. The three-phase voltages on the PCC bus are measured by OPAL-RT's OP8662 sensor box. All measurement analog signals are fed into the OPAL-RT's OP5600 Real-time Simulator, where the real-time data acquisition and controllers are implemented. Finally, the gate signals are output by OP5600 via the analog output ports.

For safety reason, the power level and scale are lowered to study the energizing process in case of large reverse power flow and inrush current. The power level will be boosted up in future when startup process is settled. The experimental setup and parameters are shown in Tab. 2.1.

2.5.1 Start-Up of Hardware Test Bed

With everything implemented as shown in Fig. 2.19, the test bed is attempted to be energized. In the initial trials of manually start-up, the experiments failed and large reverse current was observed. After researches and experiments, the critical steps lead to smooth starting up the hardware testbed are concluded as follows.

2.5.1.1 DC-link Capacitor Pre-charging

DC-link capacitor is commonly used for the IBRs to provide more stable DC voltage on the inverter input ports by limiting the fluctuations due to the inverter operations. The usage of the charged DC-link capacitor can also help avoid surge currents through the power electronics devices, which could significantly shorten the inverter lifespan and cause damage on the DC side sources. Therefore, the pre-charging step is essential.

Generally, there are two simple methods of pre-charging the DC-link capacitors when energizing the inverter plants. Either charging from the DC side or from the AC side. Charging from DC side is straightforward, connect and turn on the DC side source while all the power electronics module remain open (off) status. For high DC voltage situation, ramping up the source voltage is recommended. Charging speed depends on the voltage level and capacitor size.

Charging the DC-link capacitor from the AC side is realized by the topology of the inverter. For example, SiC MOSFET-based inverter contains diodes on each switch. With all switches kept in open status, the full-bridge inverter acts as a rectifier. Then, the grid side AC voltage will build up DC voltage and charge the DC-link capacitors. However, this method could cause reverse current flow on the DC side when the DC source is connected at lower voltage. Thus, the DC-link capacitor is pre-charged from the DC voltage source in this paper. If the real-world power grid is applied, then a circuit breaker can be used when pre-charging from the DC side.

2.5.1.2 Synchronization

PLL, as the main synchronization control system in GFL control, has been introduced in the previous part. The requirements of tuning the PLL gains are as follows.

- Fast response speed, usually faster than the current control,
- Proper filtering capability to reduce harmonics and noises,
- Not to create large computation burden to the controller,
- As small oscillation as possible to prevent inverter and controller from saturation.

With the help from the PLL, the PCC bus angle can be tracked down and provided to operator to adjust the energizing process. Chances of unstable scenario can be significantly reduced by avoiding large angle differences when startup.

Energization With the DC-link capacitor pre-charged, the energization is then started with the grid synchronization. Enable the measurement unit and the PLL implemented in the real-time simulator to track down the grid frequency, phase angle, and voltage magnitude. In the beginning, the PWM gate signals are blocked between the controller and switches, and the inverter is not yet energized and connected to the grid. Before enabling the gate signals, proper adjustments and preparations are required to be made manually or automatically for soft energization.

Soft energization of the grid-following inverter system means to adjust the starting operation condition of the inverter to smoothly connect to the grid and inject current with less spikes in the transient. Therefore, the startup current should be as low as possible to produce almost zero power flow while remain on status and synchronized. To adjust the operation, two different methods are performed: (1) open-loop adjustment (manual); (2) close-loop control (automatic). The comparisons from the experimental results are presented.

The root of operating inverters is to adjust the modulation index magnitude, frequency, and phase angle. To generate minimal current when starting up the grid-tied inverter, the modulation should be adjusted based on PCC bus voltage information provided by the PLL.

The relationship among AC side terminal voltage $v_{t,abc}$, dc side voltage V_{dc}, and modulation index magnitude m is $V_t = m\frac{V_{dc}}{2}$, where V_t is the terminal voltage magnitude. Therefore, the modulation index magnitude can be quickly computed and assigned. 60 Hz is usually assumed to be the nominal frequency for the modulation signal. The angle of the PCC bus voltage read from the PLL against the universal 0 degree, ϕ, can be approximately calculated as follows.

$$\phi = \theta_{PLL} - \omega_0 t, \tag{2.5}$$

where $\omega_0 = 2\pi 60$ rad/s. Thus, the modulation index phase angle can now be adjusted manually according to the measurement. This is the basic open-loop adjustment for energizing

grid-tied inverter system. However, as real-world voltage frequency fluctuates, the frequency of the PCC bus is not ideally 60 Hz at all time. The frequency difference creates current drifting issue when performing open-loop adjustment manually.

Open-loop start-up method is sensitive about the time delay of the implementation, which is usually caused by hardware devices and connections. Such issue was not included and documented in most EMT simulations, so the impact is usually ignored. To avoid the influences due to the time delay, a compensation reflected in angle shall be considered.

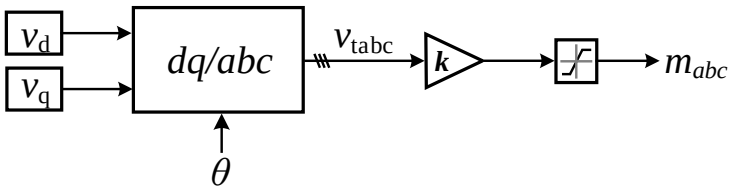

Figure 2.20: Structure of open-loop modulation generation on the converter reference frame.

The open-loop adjustment is realized via the structure shown in Fig. 2.20, where values of v_d and v_q are given based on measurement manually. Angle θ is adjusted according to the PLL's output.

To compare the differences among manual open-loop adjustments for energizing, the following case studies are performed:

- Case 1: $\theta = \omega_0 t + \phi$, use ideal 60 Hz.
- Case 2: $\theta = \theta_{PLL} + \theta_{comp}$, use PLL frequency and angle with compensation of time delay.
- Case 3: $\theta = \theta_{PLL}$, without delay compensation.

Fig. 2.21 presents the comparison of experiment results between Case 1 and 2. The blue lines indicate the energizing condition when ideal 60 Hz frequency is applied, where drifting issue is obvious. And the red lines show the condition when PLL frequency and

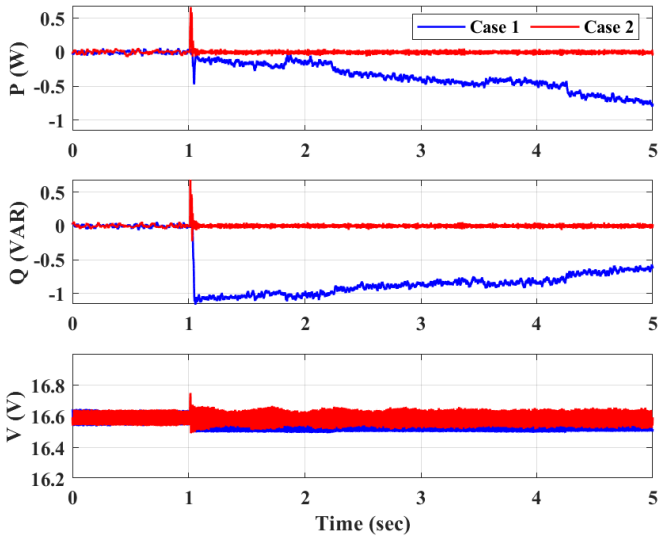

Figure 2.21: Measurements for comparison of different open-loop start-up adjustments.

delay compensation are considered. Therefore, the tracked frequency and phase angle from PLL should always be used when energize grid-tied inverter system.

On the other hand, to present the case when the time delay compensation is not considered, a separate experiment was performed. And the experiment results are presented in Fig. 2.22.

From Fig. 2.22, the energizing operation created a large reverse current flow and reactive power. The modulation magnitude is fully saturated as well. In experiment, the DC power supply was faulty immediately when PWM is unblocked due to the reverse current. Such failure could damage the system if high power level is applied. Therefore, the PLL frequency and time delay compensation should always be implemented if manual open-loop adjustment approach is chosen when energize grid-tied inverter systems.

Although the delay issue is discussed and resolved, the effort to eliminate its impact could stay and change when hardware device combination is changed, which makes the delay compensation also a variable to adjust manually. Therefore, the close-loop control is adopted to resolve the issue automatically.

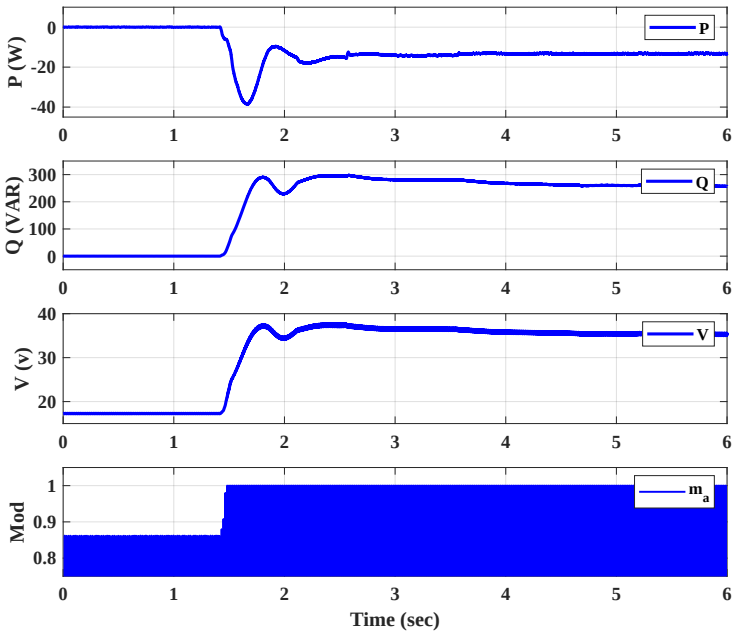

Figure 2.22: Faulty open-loop start-up adjustment.

The close-loop *dq*-frame current controller is implemented as shown in Fig. 2.23. The PI controllers employed minimizes the difference between references and measured current *dq*-components on the converter reference frame. The delay is compensated by the controller automatically.

In [47], the author indicates that the feed-forward compensation can significantly lower the starting up transient amplitude when energizing inverters, which is highlighted in the blue dotted box. In this paper, the feed-forward compensation is examined on the hardware testbed to show the improvement on soft energizing grid-tied inverter system.

Fig. 2.24 presents the experiment results when the inverter is energized under the close-loop current control with and without the feed-forward compensation. To limit the sending current from the inverter at the beginning, the reference values are set as 0 for i_d^* and i_q^*.

As shown in Fig. 2.24, the transient amplitudes with feed-forward compensation implemented are much lower than those without the compensation in the measurements of the real power, reactive power, and voltage magnitude at the PCC bus. Additionally, it shows no need of delay compensation when close-loop current control is adopted.

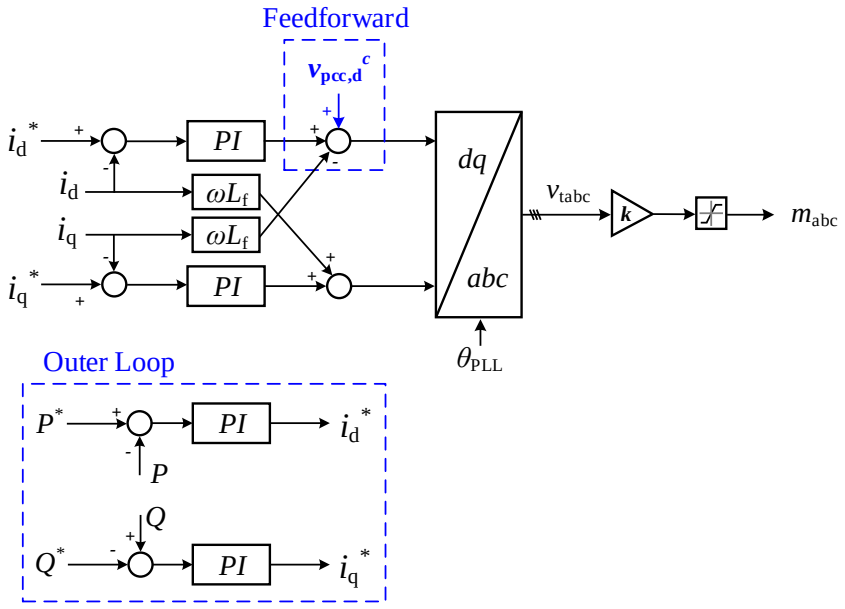

Figure 2.23: Structure of close-loop *dq*-frame current control loop and outer power control loop.

Furthermore, based on experiment results from Fig. 2.24, the outer control loop was added. The outer controller regulates the PCC bus real and reactive power. Similarly, to minimize the current flow when energizing, the reference values for the real/reactive power commands are given as 0. Experiment results are shown in Fig. 2.25.

From the comparison in Fig. 2.25, the startup transient includes large oscillations when the outer control is added. Sudden reverse power flow and oscillations exist. On the other hand, almost no obvious transients can be observed when the inverter is energized with only current inner control implemented.

Therefore, it summarizes that the optimal solution of energizing grid-tied inverter system is to startup under close-loop controller with feed-forward compensation and proper synchronization, which provides much less transient stress to the devices. Additionally, the controller should be implemented as simple as possible. Advanced controller can be added after the inverter is fully energized.

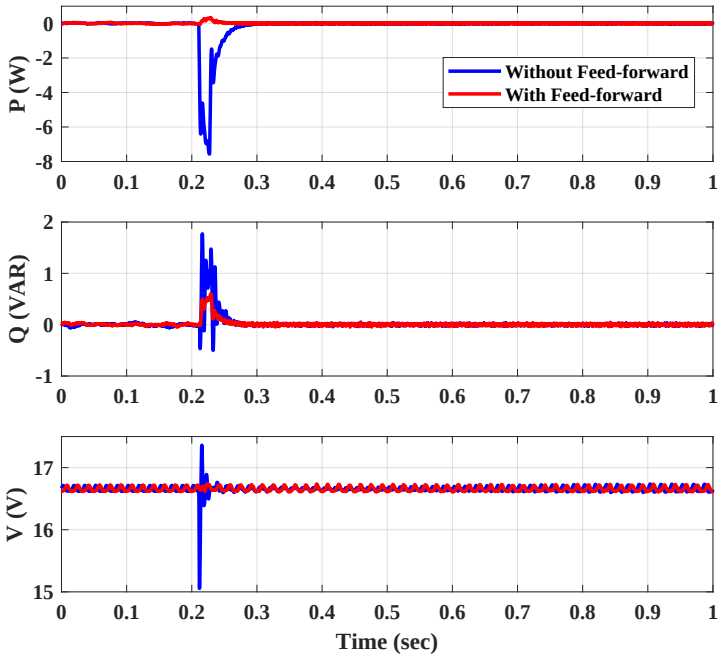

Figure 2.24: Startup transient comparison between energizing the grid-tied inverter under close-loop current control with and without feed-forward compensation.

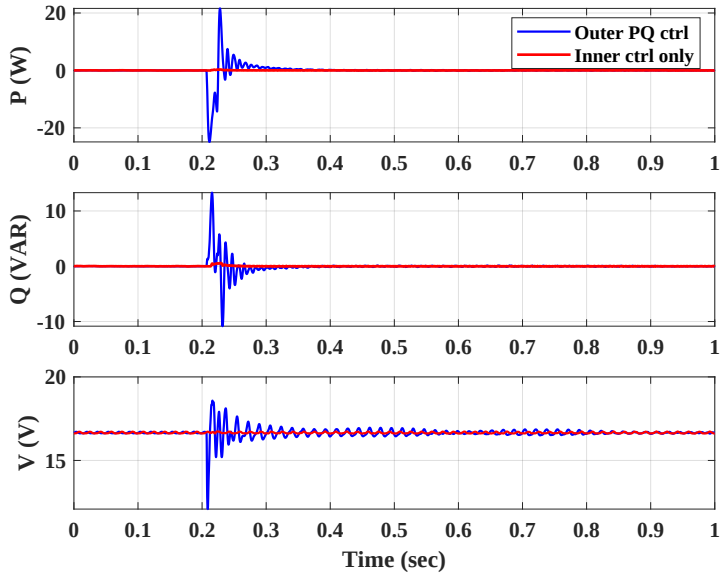

Figure 2.25: Energizing the grid-tied inverter system with PQ outer control loop and current inner control loop.

While the optimal energizing method of starting up single grid-tied inverter system is obtained from experiments, the strategy to soft energize multiple inverters system is presented below.

As shown in Fig. 2.18, both inverters are connected to the grid from the same PCC bus through a RL choke filter. For the hardware implementation, the inverters and DC power supplies are the same. The only difference is the size of the RL choke filters.

Based on the soft energizing method obtained from the previous experiments, the starting up process is similar. First, the DC supplies are turned on to pre-charge the DC-link capacitors for both inverters. Next, the grid emulator is turned on, and the PLL starts to track the voltage on the PCC bus to synchronize. Then, deploy the inverter after enabling the close-loop current control with feed-forward compensation. However, the discussion here is whether both should be turned on simultaneously or sequentially. Two sets of experiments are performed to provide comparison: (1) enable control and unblock PWM signals simultaneously; (2) unblock PWM signals sequentially.

Fig. 2.26 presents the recorded measurements of the total real and reactive power sent from inverter 1 and inverter across the PCC bus, and voltage magnitude in the two experiments. In the first experiment, both inverter are enabled simultaneously, and results are represented by the blue lines. In the second experiment, inverter-2 was enabled prior to inverter-1, and red lines indicate the results. According to the comparison, it shows greater transient responses in both real and reactive power when energizing both inverters simultaneously. The transient changes on the PCC bus voltage magnitude are almost identical. Although such transient may be not critical enough to cause any fault, the method of energizing sequentially should be recommended at all time to minimize the transients.

After trials and experiments, the lessons learned when energizing the grid-tied inverter systems are summarized in three major parts: energizing sequence, synchronization, and control strategy.

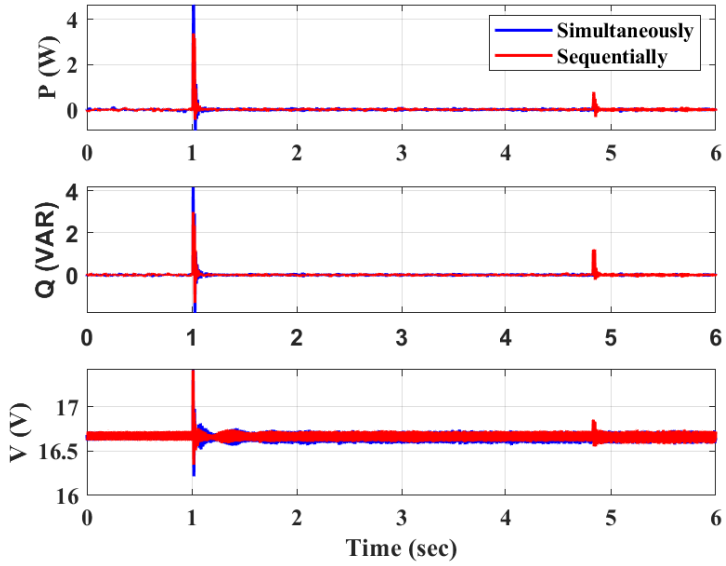

Figure 2.26: Measurements from hardware test bed of multiple inverters system.

The sequence of turning on each devices is important. Correct operation sequence can prevent the system from reverse power flow and fault scenario at the beginning, especially when deciding the dc-link capacitor pre-charging sequence. Wrong sequence or careless starting can push the dc source to fault condition easily. Additionally, energizing sequence also plays a role when starting up multiple inverter systems, where energizing them simultaneously could cause larger transients compare to sequentially.

The second take-away is to achieve and maintain the synchronization with the grid from the beginning of the energizing process. Synchronization tools, such as PLL, will provide the important information when energizing including frequency, phase angle, and voltage magnitude. These are essential when energizing the inverter manually. It worth to be mentioned that the time delay due to hardware implementation should be taken into account when manually energized. On the other hand, the converter reference frame is developed based on the phase angle detected by the synchronization tool, which helps soft energize the inverter automatically with close-loop current control and feed-forward compensation.

Last but not least, the control strategy when energizing is different from simulation. According to the experiment results, the transient could be more than 10 times larger when

directly energizing with the outer control loops. Thus, energizing the inverter system by adopting close-loop current with feed-forward compensation and synchronization is the optimal approach.

This is the end of introduction of the hardware test bed and its energizing approaches. The weak grid stability phenomena created based on the hardware experiments will be demonstrated in later chapter.

The modeling of GFL IBR integrated system ends here.

Chapter 3: Oscillations of IBR in Weak Grids

This chapter[2] presents the weak grid oscillations and their stability analysis produced in different models.

3.1 Introduction

Due to the location of renewable energy resources in the remote area, the long transmission line is required to deliver the power to the load centers from the wind farms and solar PV. Generally, transmission line is inductive. So, the longer this line is, the greater the inductive impedance will be. Short-circuit ratio (SCR) is commonly used to indicate the grid connection strength, where SCR and grid strength are positively proportional. SCR can be simply expressed by line impedance as $SCR = \frac{1}{X_g}$. As the transmission line gets built longer, the impedance is larger, and the SCR gets smaller. When SCR rating is under 2, such grid connection is referred to weak grid.

Many weak grid stability events are introduced in the beginning of this dissertation. Several of them occur when IBR generation is high in weak grids in the form of low-frequency oscillations. This chapter focuses on capturing the low-frequency weak grid oscillations and their stability analyses. All the modeling techniques are involved in this part of study.

In the first case, typical high power weak grid oscillations are presented from EMT simulation first. Then, its stability analysis conducted based on the develop analytical model is shown. In the end, hardware experiment results of this type of weak grid oscillations are demonstrated.

[2]The majority of this chapter was published in IEEE Transactions on Sustainable Energy [11], North American Power Symposium conference [3], IEEE Transactions on Power Systems [43] and [18]. Permissions are included in Appendix A.

In the second case, a detailed EMT test bed of grid-connected type-4 wind farm is carried out via PSCAD EMTDC. Due to the insufficient series-compensation level, a weak grid oscillation was captured after a line tripping event. Measurement-based black-box model is extracted from the designed dynamic event data. Finally, the stability analysis aligns with the observation in the EMT simulation.

In the last case, a newly explored weak grid oscillation that happens when curtailing the generation level is shown and explained. Based on the sensitivity studies from simulation and stability analysis, the PLL structure and current control are found to be the causes.

Detailed studies of each case are presented as follows.

3.2 High Power Weak Grid Oscillations

A single GFL IBR in weak grid system with same topology shown before is targeted. The parameters of the model are presented in the Tab. 3.1.

Table 3.1: Parameters of the Study System for High Power Weak Grid Oscillation

Description	Parameter	Value (SI Unit)	Value (Per Unit)
System	Rated Power, P_n	250 kW	1.0
	Rated Voltage, V_n	260 $V_{LL,rms}$	1.0
	Nominal Frequency, f_n	60 Hz	1.0
	DC-link Voltage, V_{dc}	1000 V	
Passives	DC-link Capacitors, C_{dc}	0.2 F	
	Choke Resistance, R	0.811 $m\Omega$	0.003
	Choke Inductance, L	0.108 mH	0.398
	Choke Impedance, X_L	40.56 $m\Omega$	0.15
	Shunt Capacitor, C	2.45 mF	0.663
	Shunt Impedance, X_C	1.08 Ω	4
	Line Resistance, R_g	20.25 Ω	0.075
	Line Inductance, L_g	0.567 mH	0.00203
	Line Impedance, X_g	0.2025 Ω	0.75
	Control Loop	**Gains**	
Controller	Outer Control	$K_p = 0.4$	$K_i = 40$
	Current Control	$K_{p,I} = 0.4758$	$K_{i,I} = 3.2665$
	PLL	$K_{p,PLL} = 60$	$K_{i,PLL} = 3200$

The EMT model is carried out via MATLAB/Simulink with SimPowerSystems Toolbox. The screenshot of the simulation model is shown in Fig. 3.1. The inverter model selected is detailed IGBT inverter.

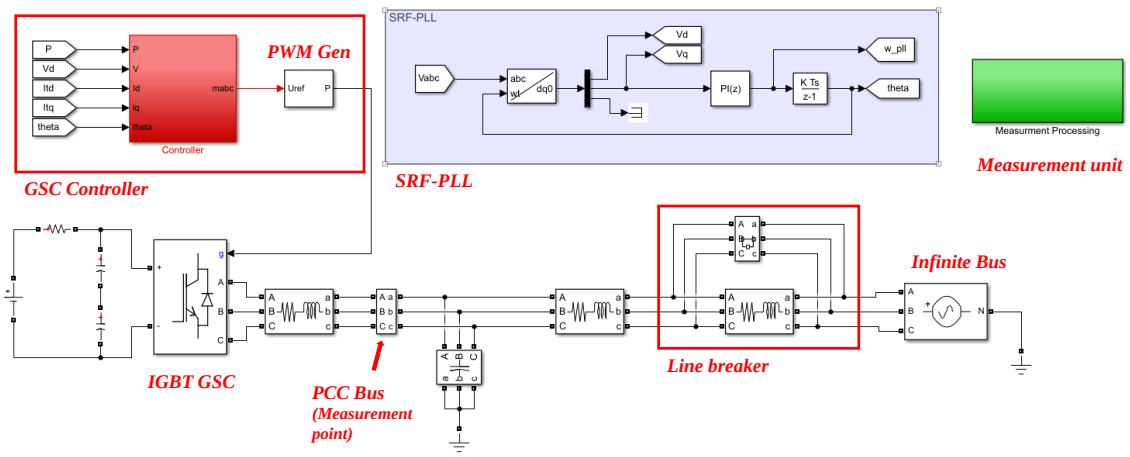

Figure 3.1: Screenshot of the EMT testbed for high power weak grid oscillation.

In this test bed, the PV control is implemented to regulate the PCC bus voltage magnitude and real power. In PV control test bed, the $P_{ref} = 1$ p.u., $V_{ref} = 1$ p.u. and the grid transmission line impedance, $X_g = 0.75$ pu.

3.2.1 Oscillation in EMT Simulations

By increasing the P_{ref} while the grid is relatively weak, the system goes to unstable condition. It is found the unstable margin appears when $P_{ref} = 1.12$ pu. Fig. 3.2 shows the P and V tracking condition when P_{ref} increases from 1.1 to 1.12 pu. From the figure, a 4.5 Hz ripple appears.

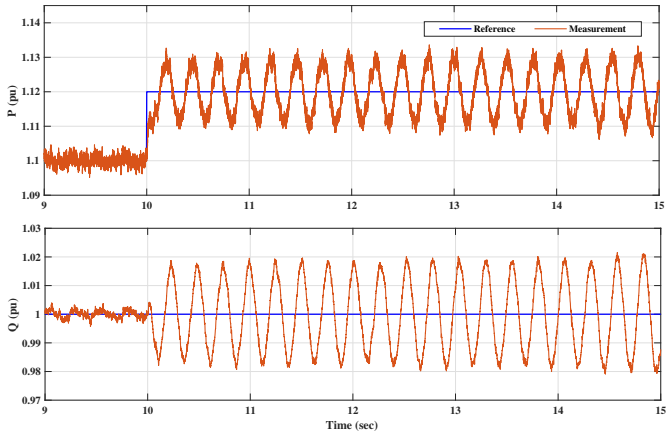

Figure 3.2: EMT simulation results for PV control when P increases from 1.1 to 1.12 pu.

On the other, increasing the line impedance X_g weakens the system when the reference power and voltage magnitude remain the same. From EMT testbed simulation, when the X_g is increased to 0.85 pu, the system is at unstable margin condition. The simulation results are presented in Fig. 3.3.

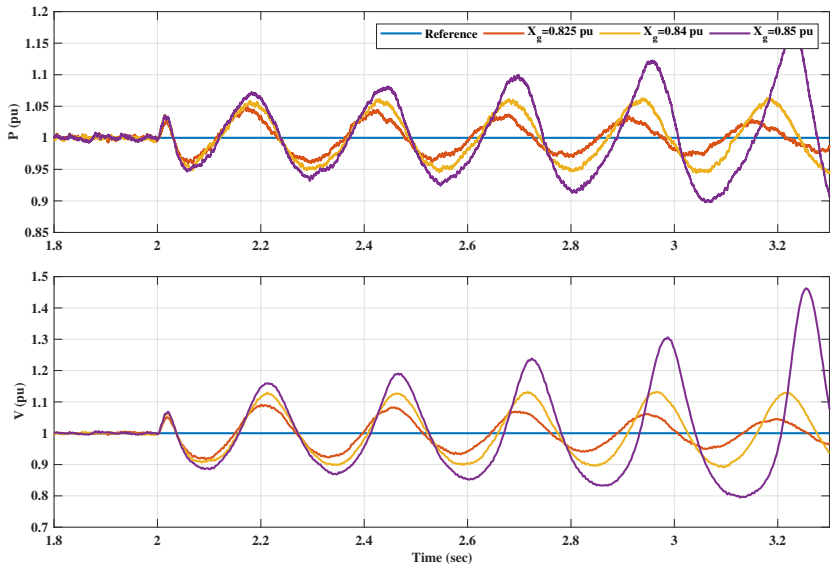

Figure 3.3: EMT simulation results for PV control when X_g increases from 0.75 p.u.

In the EMT testbed, the X_g is increased from 0.75 to 0.825 pu, 0.84 pu, and 0.85 pu separately. The tracking conditions reflect the system stability changes due to X_g increase. The ripple frequency is also about 4.5 Hz.

3.2.2 Eigenvalue Analysis

Analytical model is implemented on dq-frame. Same control strategies are implemented. Eigenvalue analysis and participation factor analysis are performed. System initialization is taken based on steady state circuit analysis and load flow via YALMIP. By fault, P_{ref} and V_{pcc} are 1 pu.

Eigenvalue loci of a varying P for PV control analytical model is plotted in Fig. 3.4. All controller parameters are the same as EMT model. X_g is 0.75 pu. P increases from 0.1 to

1.25 pu by step size of 0.05 pu. The critical low-frequency modes in the red rectangular area are shown on the right in detail.

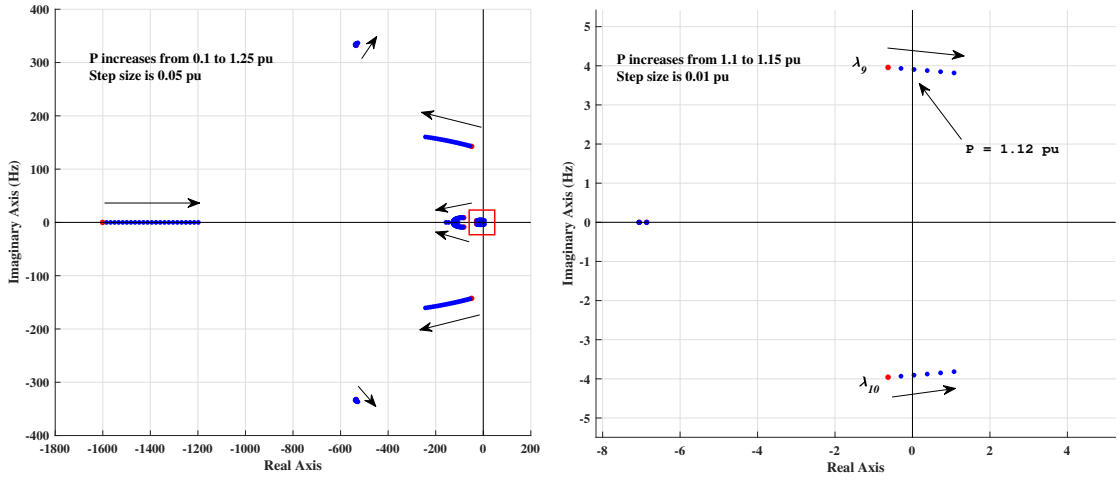

Figure 3.4: Eigenvalue loci of a varying P for PV control model.

From the Fig. 3.4, it can tell that the modes $\lambda_{9/10}$ appears on the right-hand side when P increases to 1.12 pu. and the corresponding oscillation frequency is about 4 Hz. Both are validated in the EMT simulation results shown in Fig. 3.2.

Then, the P_{ref} and V_{ref} are kept as 1 pu. The varying component is replaced by line impedance, X_g. The eigenvalue loci of a varying X_g for PV control model is shown in Fig. 3.5. The X_g varies from 0.1 to 1.05 pu by step size of 0.05 pu. Critical low-frequency modes in the red rectangular is shown on the right with smaller step size, 0.01 pu.

From the Fig. 3.5, it shows that PV control model is at unstable margin condition when $X_g = 0.85$ pu, which matches with EMT simulation results shown in Fig. 3.3. The oscillation frequency is around 4 Hz. In these case studies, the analytical model correctly reflects all the stability marginal condition when generation is increasing or the grid strength is weakened. Eigenvalue-base analyses addresses that increasing power and X_g pushes the mode pair (λ_9 and λ_{10}) from left-hand panel to the right-hand gradually.

Based on the same test bed and parameters, additional analysis of PLL's impact is examined. The original PLL gains are 60 for proportional gain and 1400 for integral gain.

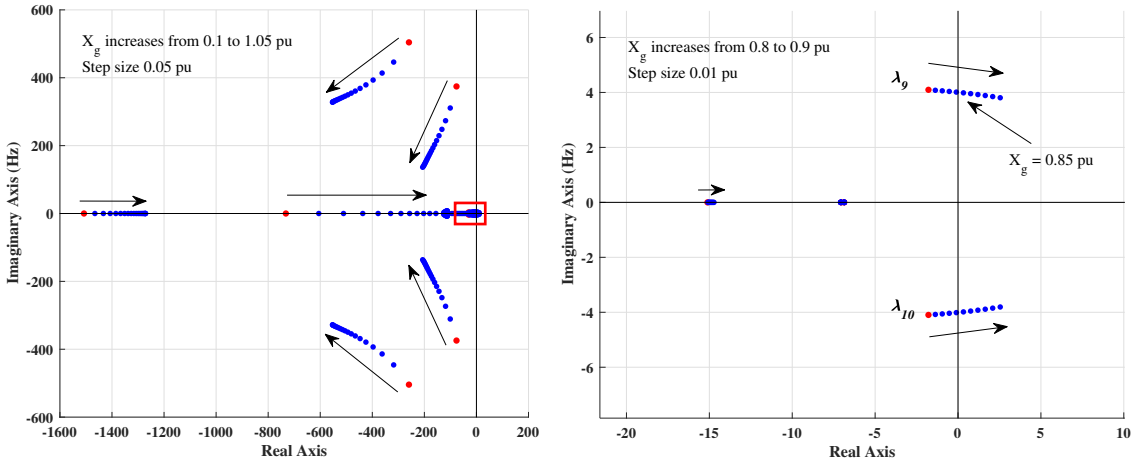

Figure 3.5: Eigenvalue loci of a varying X_g for PV control model.

Then, the integral gain is enlarged by 13 times. Such change increases the bandwidth of the PLL from 13 Hz to 34 Hz according to the Bode plot shown in Fig. 3.6. According the frequency responses, the bandwidth of PLL with larger integral gain is high, but its damping performance is lower due to the higher peak magnitude.

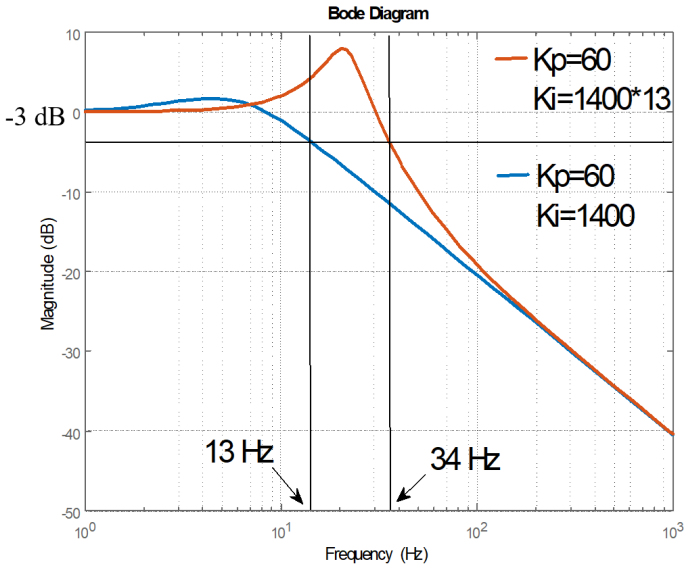

Figure 3.6: Bode plot of PLLs with original gains and enlarged gains.

In the stability analysis, the eigenvalue locus of the PLL with larger integral gain is plotted together with the original set up in Fig. 3.7. At a fixed grid impedance, the marginal

generation levels are different. With larger integral gain, the marginal stability point is lowered to 0.5 p.u. at an oscillating frequency of 19 Hz.

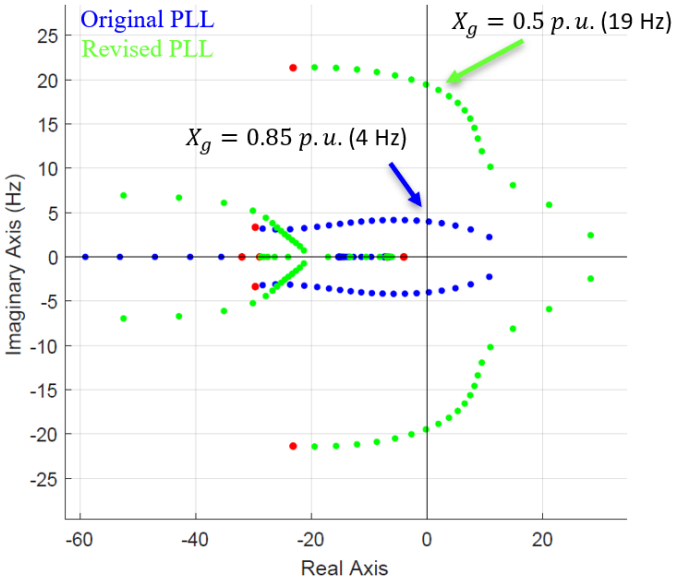

Figure 3.7: Eigenvalue-loci plots of the system with original PLL and PLL with enlarged integral gain.

To conclude, the generation level and grid strength both play an important role in the system stability of the GFL IBR in weak grids. In addition, the PLL's parameters are shown to have great impact on the oscillation mode and system stability margin.

In the hardware test bed, similar low-frequency oscillations are produced as well with both PQ and PV control [3]. The captured oscillations are presented in Fig. 3.8.

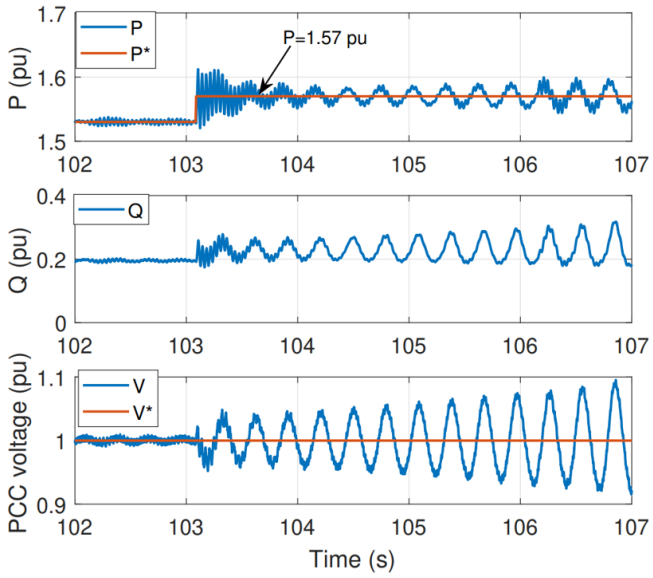

(a) PV control.

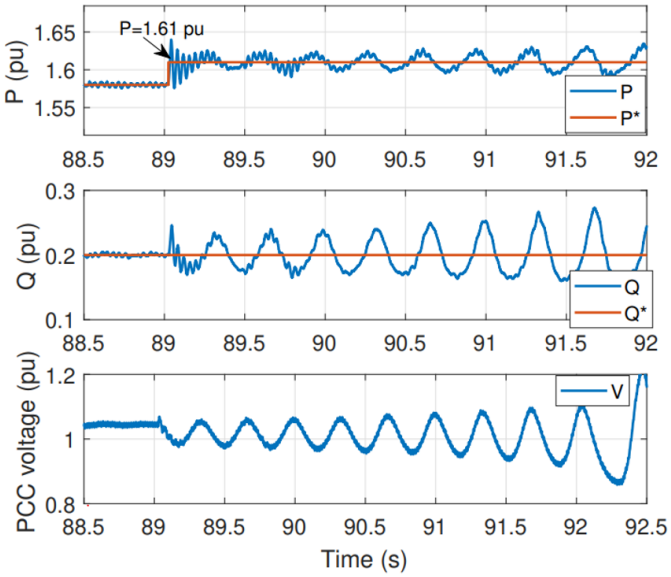

(b) PQ control.

Figure 3.8: Low-frequency weak grid oscillation due to high power generation with PV and PQ control.

3.3 Weak Grid Oscillation in Series-Compensated Network

In this part of dissertation, a procedure to obtain the DQ admittance of an IBR using event data for stability risk assessment is presented. The event data can be in two forms: three-phase instantaneous measurements or phasor measurement unit (PMU) data. Comparison of the resulting admittance against the admittance obtained from the conventional harmonic injection method shows a high matching degree in the range of 0.1 –100 Hz.

For event data, the instantaneous measurements can be obtained from digital fault recorders. On the other hand, the grid industry has implemented many PMUs to capture synchronized data at 30–60 samples per second. It would be ideal if PMU data can be used to characterize IBR admittance. While using three-phase instantaneous measurement data to obtain dq-frame measurement data has been examined in research literature, e.g., [42], using PMU data to obtain dq-frame data has not been explored in the current state-of-the-art.

Our research employs two critical technologies in two critical steps and they are (i) data fitting in time domain and frequency domain and (ii) dq-frame time-domain data derivation. The first critical step is to obtain the dq-frame data's Laplace transform or s-domain expressions of an IBR's terminal voltage and current. From there, the frequency-domain admittance measurements can be found and further fitted to the s-domain admittance model, which is suitable for the eigenvalue analysis. This step of Laplace transform can be realized by subspace methods, e.g., the eigensystem realization algorithm (ERA) or dynamic mode decomposition. The procedure has been thoroughly explained in [16] and shows superior performance in time-domain data fitting compared to the data fitting method adopted in [42]. Reference [16] mainly deals with step-response data and assumes that the voltage responses have known Laplace transforms; thus, an s-domain admittance model can be easily obtained. For transient response data, [16] does not offer the further steps on how to obtain the s-domain admittance model.

The second critical step is generating the dq-frame event data. While it is straightforward to convert data in the abc-frame to data in a dq-frame, it is not straightforward to convert PMU data into the dq-frame data. Accurate conversion requires non-trivial analytics. To the authors' best knowledge, using PMU data for admittance identification or converting PMU data to dq-frame voltage and current has not been investigated in the state-of-the-art.

To better illustrate the approach, we use a grid-tied wind power plant test bed for case studies. The wind power plant is operated in a series-compensated grid. This example is taken from [46]. The test bed is set up in an electromagnetic transient (EMT) simulation environment. Dynamic event data are generated by the EMT simulation model in the PSCAD/EMTDC environment. Three-phase voltage and current signals or PMU data are converted to those based on a synchronous dq-frame. Exported data are learned by the ERA via MATLAB to deliver the s-domain expression of each signal. Afterward, the DQ admittance measurements are computed, and their frequency-domain measurements are presented.

Once the frequency-domain admittance measurements are obtained, a method used in harmonic analysis, resonance mode analysis, proposed by W. Xu [8, 24], can be applied. This method requires first obtaining the frequency-domain network impedance. The network impedance's eigenvalues, or modal impedances, lead to information regarding oscillations. If the system is subject to oscillations, the magnitude of the modal impedance might show spikes at the oscillation frequencies.

In addition, the frequency-domain admittance measurement can be fitted using MATLAB's System Identification Toolbox [28] or the vector-fitting package [21] to arrive at the s-domain expression of the wind power plant admittance. Based on the wind power plant admittance model, the eigenvalue-based stability analysis is performed to examine the marginal condition for the system.

The study procedure is presented in Fig. 3.9.

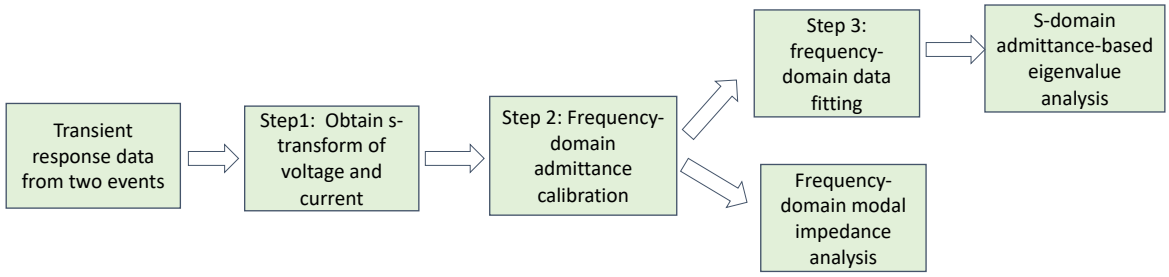

Figure 3.9: Overall procedure of event data-driven admittance identification and stability screening.

3.3.1 Weak Grid Oscillation in Series-Compensated Network

The studied test bed is a Type 4 wind power plant interconnected to a series-compensated network. The 200-MW wind power plant aggregated model consists of 40 identical 5-MW wind turbines [37]. Fig. 3.11 presents the structure of the wind power plant integrated system. The EMT test bed is built in PSCAD/EMTDC and includes a synchronous generator; three-phase back-to-back voltage-sourced converters; and the mechanical systems and control. The three-phase converters are represented by average models. Each turbine's terminal voltage level is 690 V, and it is increased to 220 kV via a step-up transformer before connecting to the main grid. The grid transmission network consists of a series-compensated line in parallel with another uncompensated line.

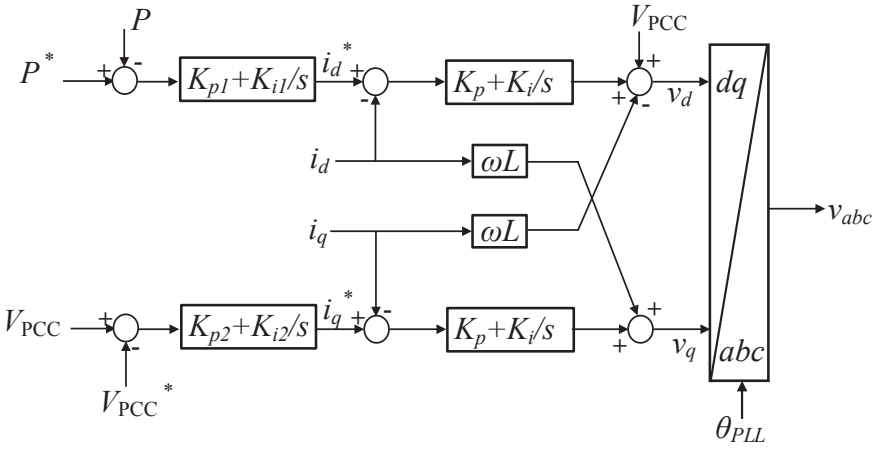

Figure 3.10: Power and ac voltage control structure.

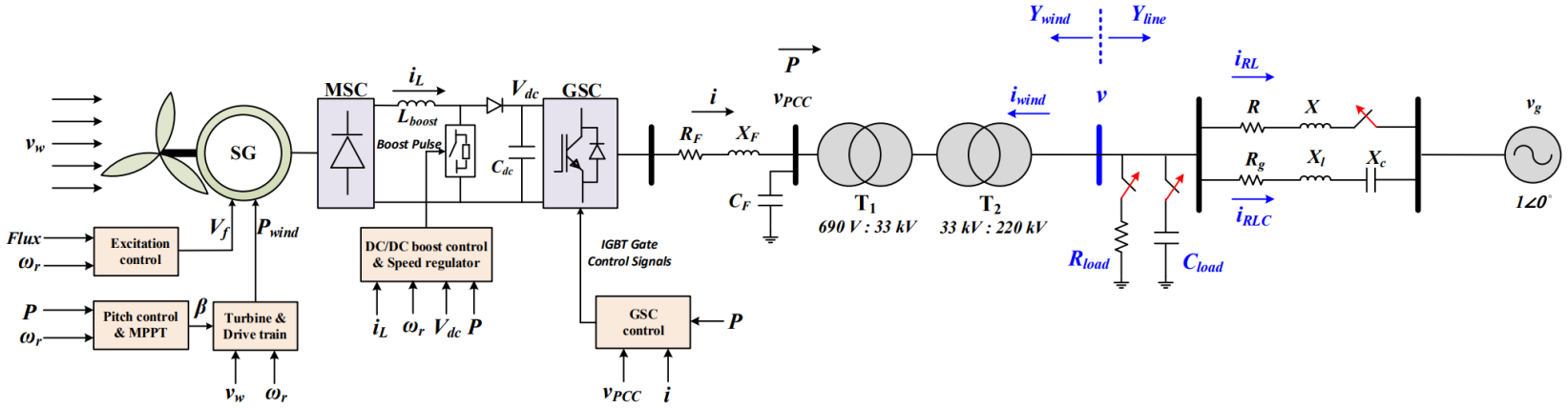

Figure 3.11: EMT test bed topology of a 200-MW Type 4 wind power plant in a series-compensated network.

Power and ac voltage control is adopted to operate the grid-side converter (GSC) to generate 1 p.u. of real power and 1 p.u. voltage at the point of common coupling (PCC) bus in steady state. Fig. 3.10 shows the control structure. In the controller, a three-phase phase-locked loop (PLL) is employed to synchronize the GSC with the grid by tracking the phase angle of the PCC bus voltage. The θ_{PLL} is the angle outputted by the PLL.

The total transmission line reactance $X_g = 0.75$ p.u. when both lines are connected, and it has an X/R ratio of 10. Without the series compensation, the line reactance, X_l, is designed as 1 p.u. Table 3.2 presents all the system parameters.

Table 3.2: Parameters of the Type-4 Wind Farm Test Bed

Category	Description	Parameter	Value
Single turbine System	Rated power		5 MW
	Rated power	S_b	200 MW
	Rated voltage	V_n	690 V, 220 kV
	Nominal frequency	f_n	60 Hz
Passives	Choke reactance	X_F	0.15 p.u.
	Choke resistance	R_F	0.003 p.u.
	Shunt capacitor susceptance	B_C	0.3 p.u.
	Transformer T	X_T	0.005 p.u.
	X/R ratio	X/R	10
	RL line reactance	X	8 p.u.
	RL line resistance	R	0.8 p.u.
	RLC line reactance	X_l	1 p.u.
	RLC line resistance	R_g	0.1 p.u.
	RLC line capacitor	X_c	0.20 p.u.
GSC Controller	Inner current control	K_p, K_i	0.4758, 3.2655
	Power control	K_{p1}, K_{i1}	0.25, 25
	AC voltage control	K_{p2}, K_{i2}	0.2, 20
	PLL	$K_{p,PLL}, K_{i,PLL}$	60, 1400

Series compensation has been widely used for decades to increase the power transfer capacity by reducing the equivalent reactance; thus, in the EMT test bed, various series compensation levels are examined to search for the system stability margin and low-frequency oscillations.

The dynamic event is designed to trip the transmission line represented by a series resistor and inductor (RL) component and to leave the series-compensated line (represented by a series-connected RLC circuit) alone to maintain 1 p.u. power from the wind power plant to

the grid. This system viewed by the wind power plant is a weak grid, and it could suffer stability issues

Fig. 3.12 presents the measurements of the Type 4 wind power plant system under the series compensation levels of 20% and 21% and the Fourier transform analysis of the real power signal. According to the simulation results shown in Fig. 3.12, when the series compensation level is less than 20%, the system is unstable with a critical low-frequency oscillation. The oscillation frequency is approximately 5 Hz. When the series compensation level is greater than 20%, the system is stable.

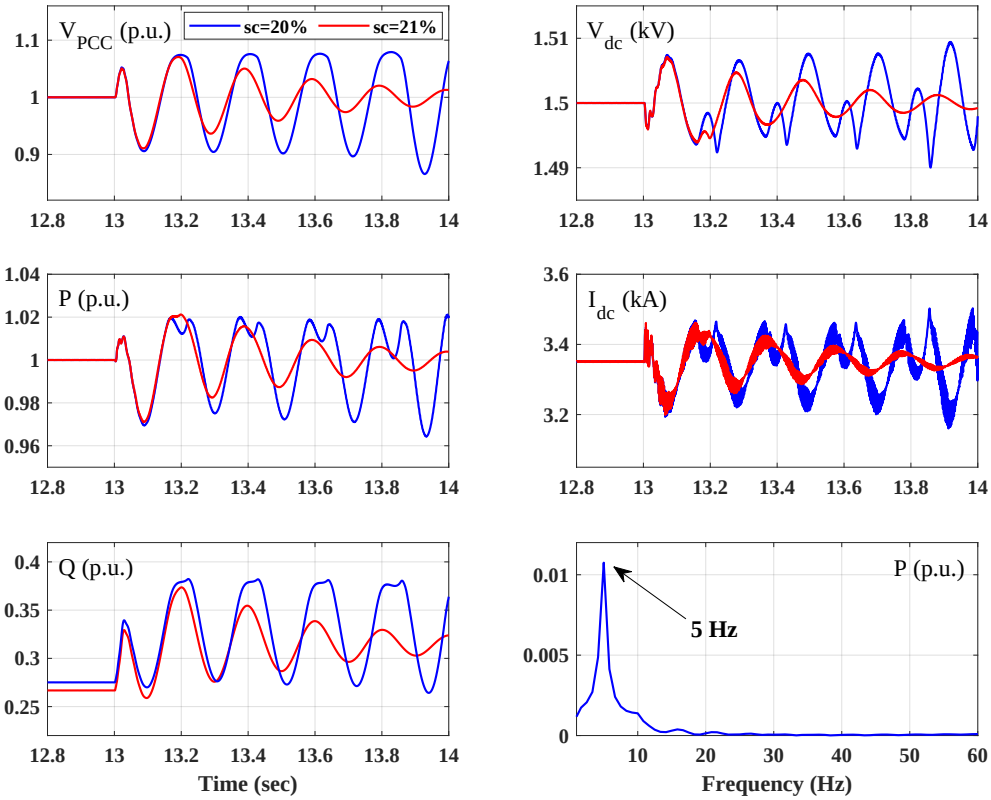

Figure 3.12: Simulation results when the series compensation level is 20% and 21%.

3.3.2 DQ Admittance Measurement

Two dynamic events are implemented separately when the two lines remain connected between the wind power plant and the infinite bus. As shown in Fig. 3.11, a resistive load is implemented on the high-voltage side of the step-up transformer, and it consumes 0.1 p.u.

real power in steady state. Disconnection of the resistive load causes transient responses in the voltage and current measurements and generates the first event data for the admittance measurement. The other event is to disconnect a capacitive load that provides 0.1 p.u. reactive power in steady state. Only one load is implemented in one event. Also, the operation condition must be the same when the resistive and capacitive loads are implemented.

For the admittance measurements, the required data include the dq-frame measurements of the voltages at the disconnection point, v; the currents flowing into the wind power plant, i_w; and the currents flowing into the transmission lines, i_{RL} and i_{RLC}. Superscripts (r) and (c) are used for the disconnection types. Additionally, when performing Park's transformation, the angle is fixed at the grid reference frame instead of from the PLL. Therefore, the post-event operating conditions are the same.

With the data v and i_w, the wind power plant admittance viewed from the disconnection point is carried out. Correspondingly, the RL and RLC line admittance are obtained from data v, i_{RL}, and i_{RLC}.

Prior to the first event, the resistive load is connected. It is then disconnected. At the same timestamp, the capacitive load is disconnected in the next event. The dq-frame measurements are presented in Fig. 3.13. The system simulation step size is 50 μs, and the plot step size is 250 μs.

Transient data that are 0.5-s long —from 0.5 s to 1 s—from each signal are captured and fed into the ERA to learn the s-domain expressions of the voltages and currents [2, 15]. The order of the estimated system is assumed to be 25. For general data processing, only transient parts of the data shall be applied and resampled. When the data include noise or ripples, a moving average filter should be considered to remove the noise.

The wind power plant operation condition is kept the same in both events; therefore, the admittance of the wind power plant shall be the same when computed from the voltage and current from different events. The wind power plant's DQ admittance measurement

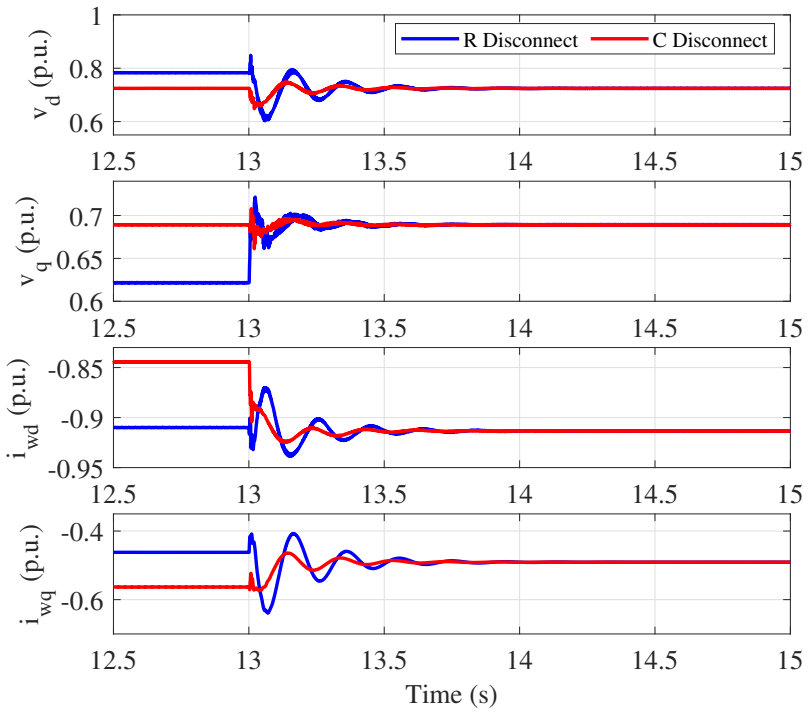

Figure 3.13: Data from two dynamic events: resistive or capacitive load disconnection.

expressions can be found from (3.1).

$$\underbrace{\begin{bmatrix} i_{w,d}^{(r)}(s) & i_{w,d}^{(c)}(s) \\ i_{w,q}^{(r)}(s) & i_{w,q}^{(c)}(s) \end{bmatrix}}_{I(s)} = Y_{wind}(s) \underbrace{\begin{bmatrix} v_{d}^{(r)}(s) & v_{d}^{(c)}(s) \\ v_{q}^{(r)}(s) & v_{q}^{(c)}(s) \end{bmatrix}}_{V(s)} \tag{3.1}$$

Further, in the frequency domain, the wind power plant admittance is found by using (3.2).

$$Y_{wind}(j\omega) = I(j\omega)V(j\omega)^{-1}. \tag{3.2}$$

The frequency scanning technique is employed to measure the admittance frequency-domain responses. The currents and voltages in the dq-frame are recorded after injecting a small-signal perturbation at the terminal. The obtained data are used to calculate the admittance model.

As Fig. 3.14 shows, the controllable voltage source is connected to the wind power plant at the interconnection point of 220 kV. Two perturbation voltages are superimposed into the voltage source, respectively. The voltages are defined in the dq-frame and converted to the abc-frame to form a three-phase voltage source. The resulting currents are recorded at the PCC bus. They are converted to dq-frame variables i_{dq}. Fast Fourier transform (FFT) is implemented to extract the phasor form of v_{dq} and i_{dq} at the frequency of the injected perturbation. Note that the injected perturbation needs to be small enough so that it has no influence on the system operation.

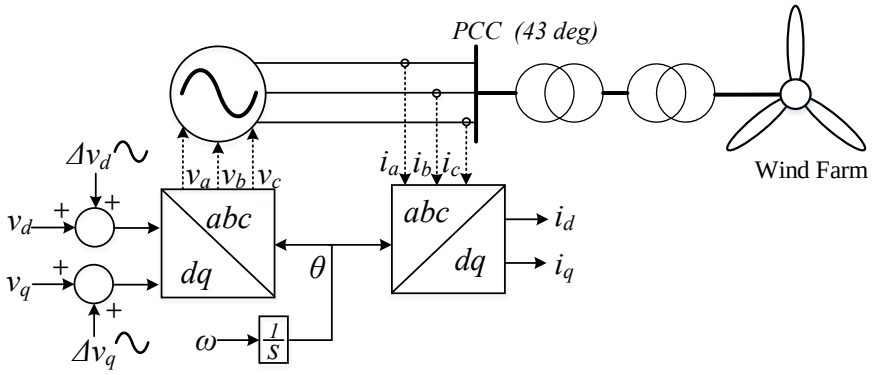

Figure 3.14: DQ-frame admittance measurement testbed.

The admittance at every frequency point is calculated as:

$$\begin{aligned} Y_{dd}(f_i) &= \frac{i_d^{(1)}(f_i)}{v_d^{(1)}(f_i)} \quad Y_{dq}(f_i) = \frac{i_d^{(2)}(f_i)}{v_q^{(2)}(f_i)} \\ Y_{qd}(f_i) &= \frac{i_q^{(1)}(f_i)}{v_d^{(1)}(f_i)} \quad Y_{qq}(f_i) = \frac{i_q^{(2)}(f_i)}{v_q^{(2)}(f_i)} \end{aligned} \tag{3.3}$$

where superscripts (1) and (2) are related to the voltage perturbation in the $d-$ and $q-$axes, respectively; f_i is the injected frequency.

The injection frequencies are swept from 1 to 100 Hz with a 1-Hz interval. The dq-frame voltages and currents are recorded and processed. The FFT window is long enough to reduce the impact of the spectral analysis.

The comparison between the DQ admittance measurements from the proposed transient response method and the frequency scanning method is shown in Fig. 3.15. The matching degree is very high.

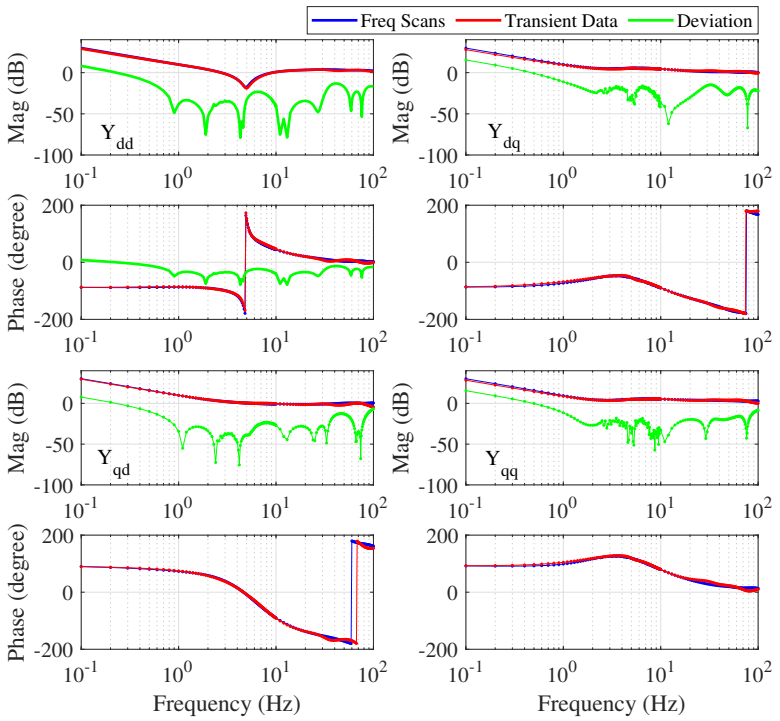

Figure 3.15: DQ admittance measurement comparison between the proposed transient response method and the conventional frequency scanning method.

One critical procedure during the admittance matching is to ensure that the same reference frame is used. In the transient response method, all DQ-frame measurement data are extracted based on the grid voltage phase angle, which is the same as the frequency scanning method. Fig. 3.16 presents the poor matching condition when the prefault voltage phase angle is applied to extract the DQ-frame transient data, instead of the grid angle.

To unify the reference frames, the angle difference needs to be compensated. In Fig. 2.24, the disconnection point voltage phase angle is identified as $\delta = 43°$ at steady state. The measurements in the prefault reference frame is compensated to refer to the grid frame

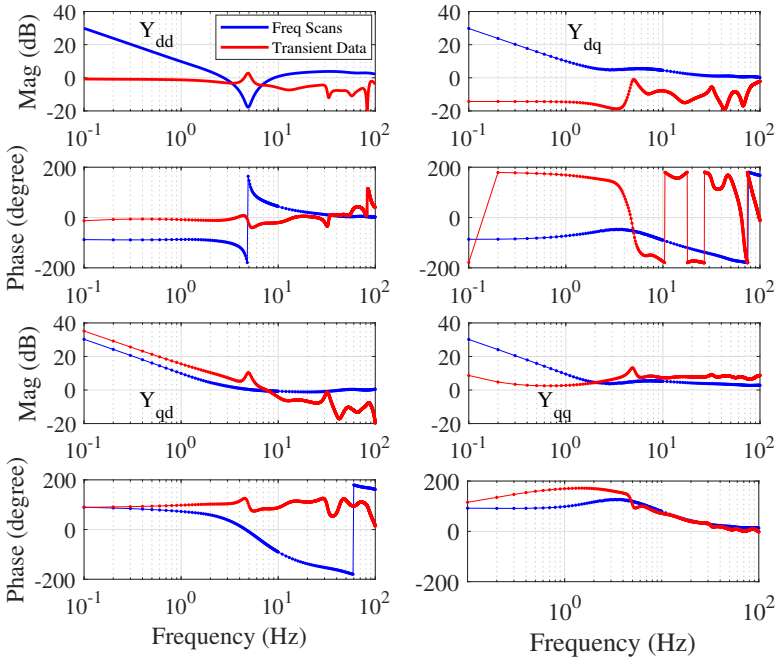

Figure 3.16: DQ admittance measurement comparison with different reference frames.

by the following compensation equation [15]:

$$Y^g = \begin{bmatrix} \cos\delta & \sin\delta \\ -\sin\delta & \cos\delta \end{bmatrix} Y^{PCC} \begin{bmatrix} \cos\delta & -\sin\delta \\ \sin\delta & \cos\delta \end{bmatrix} \tag{3.4}$$

3.3.3 PMU Data-Driven DQ Admittance

This section answers this question: Can PMU data also produce DQ admittance? PMUs are widely installed in bulk power systems. Each PMU provides data of root mean square (RMS) voltage, frequency, real power, reactive power, and phase angle with a certain resolution at its location; thus, the current measurements are not available. It becomes a challenge whether PMU data can also be applied to produce the DQ admittance via the proposed method. The key is to obtain the correct *dq*-frame voltage and current transient data from PMU data.

A PMU installed close to a bus on a line measures the following five measurements: real power, P; reactive power, Q; voltage RMS, V; voltage phase angle, θ; and frequency, f. In turn, we obtain the five variables' deviations from their initial steady-state values: ΔP, ΔQ, ΔV, $\Delta\theta$, and Δf.

PMUs rely on a global positioning system for synchronization; thus, θ is based on a global reference. If a dq-frame leads the global reference by an angle α, then the projections of the voltage phasor to the d-axis and the q-axis are as follows:

$$v_d = V\cos(\theta - \alpha) \tag{3.5}$$

$$v_q = V\sin(\theta - \alpha) \tag{3.6}$$

The dq-frame voltage deviations can be found from the following equations:

$$\Delta v_d = \cos(\theta_0 - \alpha)\Delta V - V_0\sin(\theta_0 - \alpha)\Delta\theta \tag{3.7}$$

$$\Delta v_q = \sin(\theta_0 - \alpha)\Delta V + V_0\cos(\theta_0 - \alpha)\Delta\theta \tag{3.8}$$

where ΔV and $\Delta\theta$ are required to construct Δv_d and Δv_q.

By adopting a dq-frame that leads the global reference with an angle the same as θ_0 ($\alpha = \theta_0$), we can construct the dq-frame voltage and their deviations as follows:

$$\begin{cases} v_d = V \\ v_q = 0 \end{cases}, \begin{cases} \Delta v_d = \Delta V \\ \Delta v_q = V\Delta\theta. \end{cases} \tag{3.9}$$

Next, we aim to obtain the deviations of the dq-frame current components. From the complex power S expression, real power, P, and reactive power, Q, can be expressed as

follows:

$$S = \bar{V}\bar{I}^* = (v_d + jv_q)(i_d - ji_q) \tag{3.10}$$

$$\Longrightarrow \begin{cases} P = v_d i_d + v_q i_q \\ Q = -v_d i_q + v_q i_d. \end{cases} \tag{3.11}$$

The deviations of power can be expressed as follows:

$$\begin{bmatrix} \Delta P \\ \Delta Q \end{bmatrix} = \begin{bmatrix} v_d & v_q \\ v_q & -v_d \end{bmatrix} \begin{bmatrix} \Delta i_d \\ \Delta i_q \end{bmatrix} + \begin{bmatrix} i_d & i_q \\ -i_q & i_d \end{bmatrix} \begin{bmatrix} \Delta v_d \\ \Delta v_q \end{bmatrix}. \tag{3.12}$$

Thus, the dq-frame current deviations can be found from the power deviations and the voltage deviations.

From the same grid-following Type 4 wind power plant PSCAD test bed, the PMU data are collected for the wind power plant admittance measurement. Two dynamic events (connecting the resistive load or connecting the capacitive load) are implemented to create transient data. The time-domain PMU data are presented in Fig. 3.17(a), where the blue lines are data from the first event, and the red lines record data from the second event.

Fig. 3.17(b) presents the constructed data of Δv_d, Δv_q, Δi_d, and Δi_q for further admittance measurement. Note that the dq-frame is assumed to be aligned with the measurement point voltage at steady state.

With the transient data constructed, ERA learning is performed to find the s-domain expressions of each signal. The system order is assumed to be 9. The DQ admittance's frequency responses are computed from 0.1 to 100 Hz for comparison. In the final step, the measurement point voltage angle is considered, and the angle compensation is conducted so that the admittance is now viewed from the grid dq-frame.

The comparison between the results from the proposed method with the PMU data and harmonic injection results are presented in Fig. 3.18. The matching condition shows that PMU data are feasible to obtain admittance.

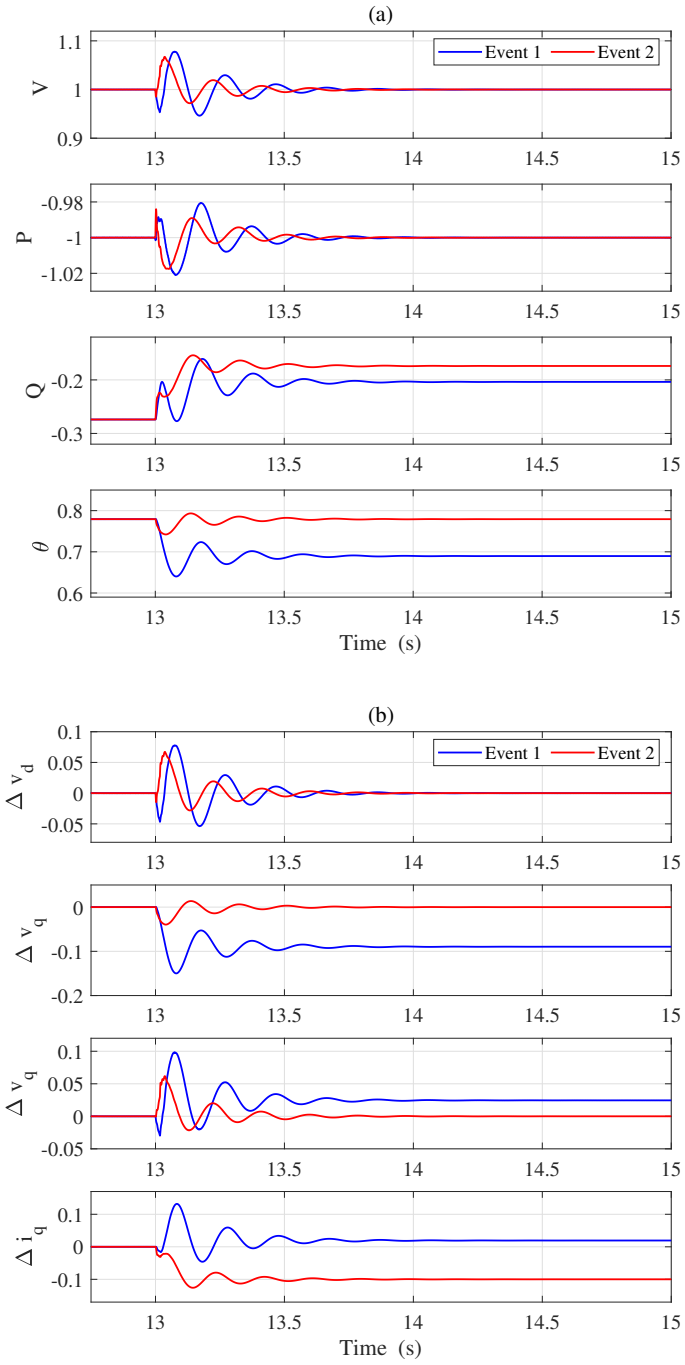

Figure 3.17: PMU measurement data for two load connection events and constructed *dq*-frame data.

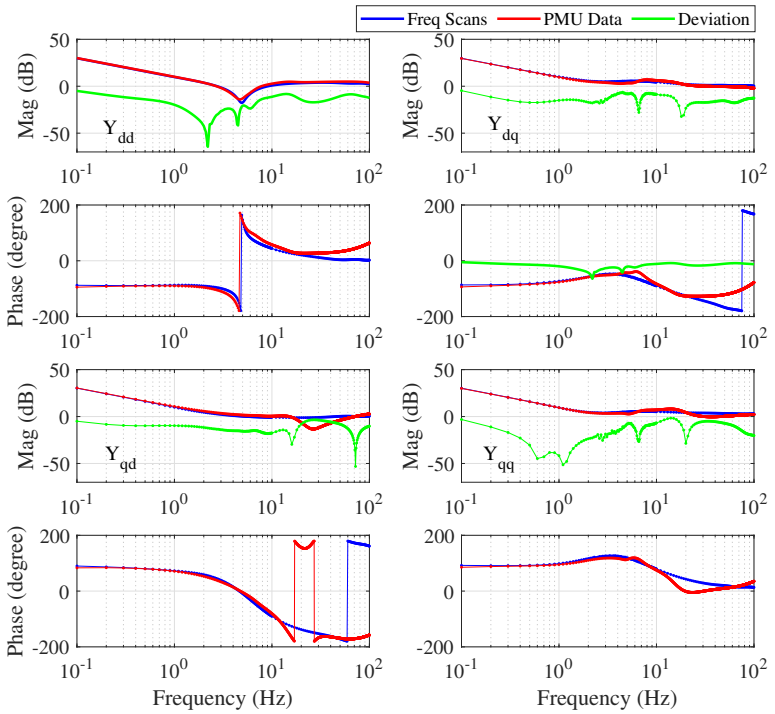

Figure 3.18: DQ-admittance measurement from PMU data by the proposed method compared to the frequency scanning results.

3.3.4 Admittance Identification and Stability Analysis

In this section, the s-domain admittance matrix of the EMT model will be identified based on the data from the ERA method. With the known admittance model, the eigenvalues can be found, and stability analysis will be carried out.

Frequency-domain data fitting is necessary to arrive at a linear time-invariant system or a transfer function. The technique of frequency-domain data fitting is mature. MALTAB's System Identification Toolbox [29] has such a function. In addition, the vector-fitting package [21], available in the public domain, also achieves the goal of data fitting.

The vector-fitting package [21] is used for the frequency-domain curve fitting to find the transfer functions. For a two-input, two-output system representing a DQ admittance, the frequency-domain responses are assumed to be generated from a single-input and four-output system. This system has an assumed order of 16. After the state-space linear model is found

from the vector fitting package, the 4×1 transfer function matrix is found. The matrix is then reshaped to become a 2×2 transfer function matrix. This system, after converting it to a state-space model, has an order of 32, even minimal realization is specified in the MATLAB function `ss`.

Fig. 3.19 presents the comparison of the linear model built by curve-fitting and the measurement data of the wind power plant obtained from the PMU data in Fig. 3.17.

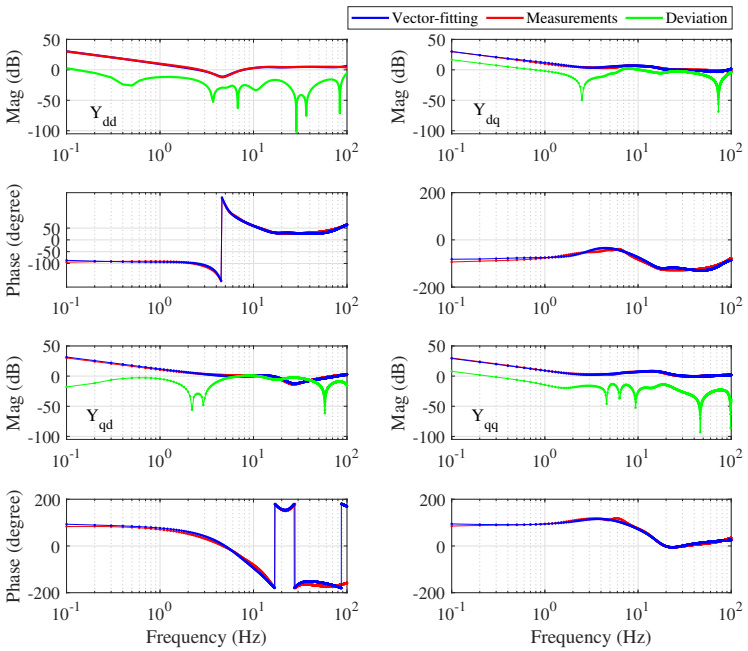

Figure 3.19: Comparison of the Bode plot of the DQ admittance from the PMU measurement and curve fitting.

For the post line-tripping operation, a wind power plant is connected to grid through a series-compensated transmission line. Viewed from the PCC bus, the system consists of two shunt admittance connected in parallel. The equivalent circuit of the system is shown in Fig. 3.20.

So the total admittance of the system is

$$Y = Y_{wind} + Y_{RLC}.$$

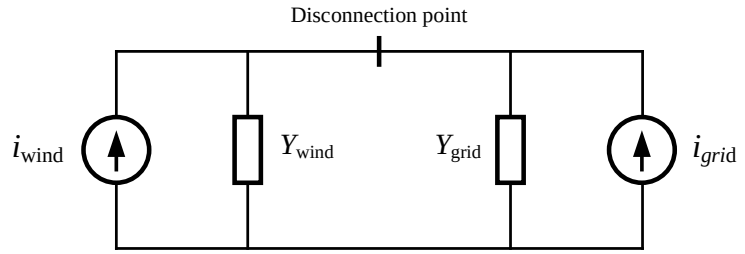

Figure 3.20: Equivalent impedance model of the grid-connected wind farm system.

where

$$Y_{RLC} = \begin{bmatrix} R_g + sL + \frac{s}{C(s^2+\omega_0^2)} & -X_l + \frac{\omega_0}{C(s^2+\omega_0^2)} \\ X_l - \frac{\omega_0}{C(s^2+\omega_0^2)} & R_g + sL + \frac{s}{C(s^2+\omega_0^2)} \end{bmatrix}^{-1},$$

$L = X_l/\omega_0$, $C = 1/(\omega_0 X_c)$, and $\omega_0 = 377$ rad/s.

The eigenvalues of the system are the roots of $\det(Y)$. The approach of eigenvalue analysis has been proposed in 1999 by Semlyen [35] and the method was recently expanded to three-phase IBR system stability analysis in [14].

Note that DQ admittance was introduced in 1997 for three-phase ac systems stability check [5]. In power electronics, to perform stability check, it is popular to use generalized Nyquist stability criterion relying on the frequency-domain measurements [38]. On the other hand, the eigenvalue-based analysis relying on the admittance requires admittances having a Laplace transform according to the method originally proposed by A. Semlyen in 1999 [35]. Fan and Miao expanded the method to the stability analysis of IBR-penetrated power grids relying on the DQ admittance. This method has been benchmarked against the conventional eigenvalue analysis approach and has been shown to be accurate [15]. In addition, the method is shown to have more advantages than the frequency-domain generalized Nyquist stability criterion [14].

Before the eigenvalue computing step, the balanced truncation is conducted on Y_{wind} to reduce the model size to 16. This step helps remove redundant poles. The frequency domain responses of the admittance before and after the balanced truncation are shown in Fig. 3.21.

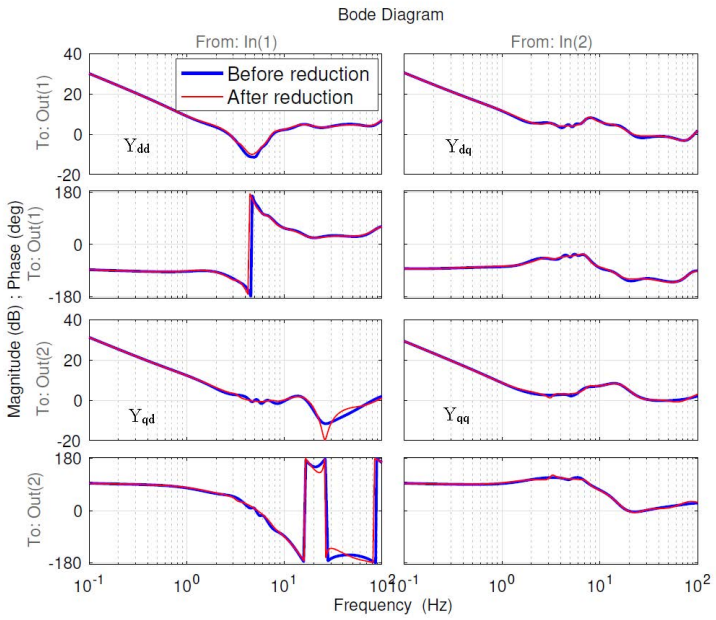

Figure 3.21: Admittance before and after the balanced truncation.

The stability analysis for the system can be carried out by eigenvalue loci, as shown in Fig. 3.22. When the series compensation level decreases, the system tends to be unstable. The eigenvalue loci presents various series compensation levels from 15% to 25%. An eigenvalue at approximately 6 Hz will move from the right-half plane to the left-half plane when the series compensation level increases and the system becomes stronger. The series compensation level 20% is identified as the stability margin condition. And this analysis result corroborates the EMT simulation results presented in Fig. 3.12.

We may further use the modal impedance method of [8] to quickly evaluate the risk of stability by examining the eigenvalues of the network impedance matrix $Z(j\omega)$ evaluated at frequency points: $Z(s) = Y(s)^{-1}$. Hence, a system eigenvalue, λ, is the pole of $Z(s)$ or the zero of $Y(s)$. If $Y(s)$ is evaluated at this eigenvalue notated as $\lambda = \sigma \pm j\omega$, $Y(\lambda)$ is singular. If this eigenvalue has a very small real part, then $Y(s)$ is close to singularity when s is evaluated at $j\omega$ and $Z(s)$ is expected to have a very large eigenvalue. W. Xu *et al* [8,24] used this reasoning to recommend plotting the eigenvalues of the network impedance. At

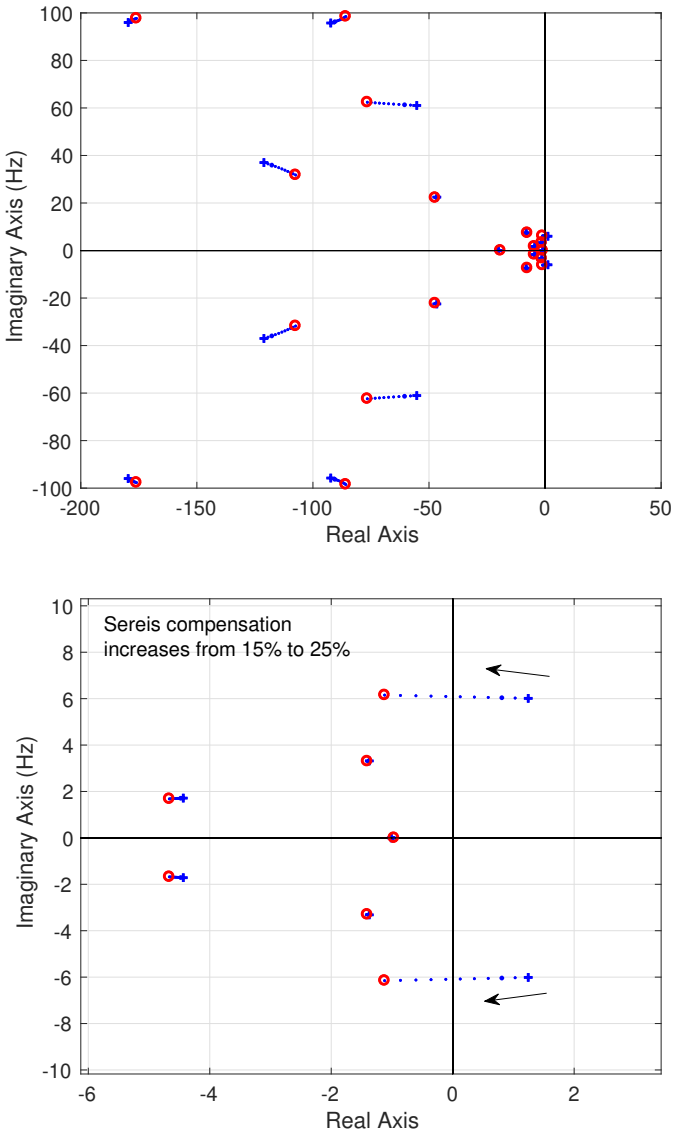

Figure 3.22: Eigenvalue loci for a system with different series compensation levels.

the oscillation frequency, if a system is close to the stability margin, we expect to see a spike in the eigenvalue's magnitude in the frequency domain.

Fig. 3.23 presents the eigenvalue plots for two cases: series compensation at 20% and at 30%. The spike occurs at 6 Hz. In addition, the first case shows a larger spike, indicating that the 20% case is closer to the marginal stability condition.

To conclude, this part of dissertation presents a process of online measurement of the DQ admittance of a Type 4 wind power plant using two sets of dynamic event data. A critical

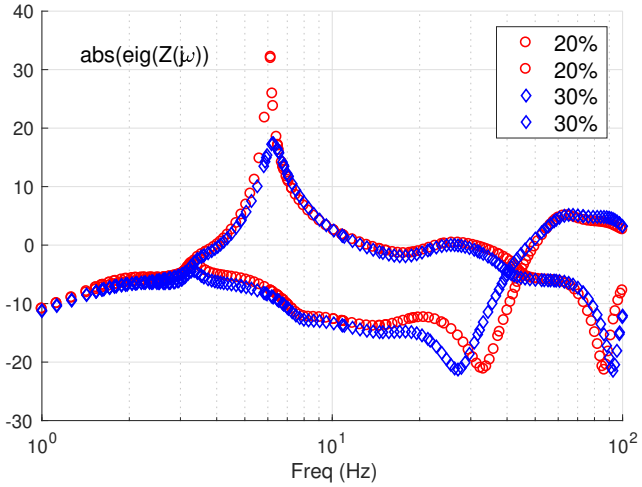

Figure 3.23: Magnitudes of the network impedance matrix's eigenvalues evaluated at every frequency point.

step is to obtain the s-domain expressions of the dq-frame voltage and current signals. This step leads to the DQ admittance frequency-domain measurements. Curve-fitting of the frequency-domain data further leads to the s-domain admittance model and can be used for the eigenvalue analysis. The paper also demonstrates that the dq-frame voltage and currents can be obtained from the PMU measurement data; thus, the proposed approach can lead to wide adoption by the electric grid industry for monitoring and stability screening.

3.4 Low Power Weak Grid Oscillation

Among the 19 real-world oscillation events associated with IBR from multiple countries reported in the recent PES Task Force report [7], it has quite a few events are associated with PLL. [45] points out that PLL introduces a negative resistance in the low-frequency range. Several recent research papers [12, 13, 17, 18, 27] show that PLL with insufficient damping may cause stability issues. Specifically, [18] shows that low-pass filters to smooth sensor measurements and filter out 2^{nd} harmonic components due to unbalance are the cause of insufficient damping in PLL.

Usually, low-frequency oscillations due to high power generation in weak grids can be mitigated by reducing the generation. However, in this study, a strange weak grid oscillation phenomenon is captured when curtailing the power exporting level. In the dq frame analytical model, the 2^{nd} order filter was not considered at the first place, which leads to analysis results failing to reflect the system stability condition observed in the EMT simulations. After PLL model benchmark, the stability analysis can correctly estimate the marginal operating points at both high power and low power levels.

Our contributions are developing the analytical model for PLL for accurate stability check, such as eigenvalue analysis. The study results indicate the causes for the captured stability issue are the insufficient damping of PLL and slow current control, and the system stability can be improved accordingly.

3.4.1 Captured Oscillations at Lower Generation

The topology of the study test bed is same as in previous chapters, where a grid-following VSC is connected to the grid voltage source through a transmission line. The adopted control strategy is PV vector control as shown in Fig. 3.10: the inner loop is current control and the outer loop is real power and ac voltage control. The controller is implemented on the PLL frame.

The system and controller parameters are listed in Tab. 3.3. Since the parameters were used in hardware test bed, additional 1^{st} order low-pass filters with 3 ms time constant are used to suppress the noises in the measurements [4, 44].

The EMT simulation test bed is carried out via MATLAB/Simscape with SimPower-Sytem toolbox. Fig. 3.24a presents the captured strange oscillation phenomenon that caused our attention. Initially, a 5 Hz weak grid oscillation appeared when the exporting power level is increased to 1 p.u. at 5 seconds. To suppress the oscillation and maintain system sta-

Table 3.3: List of Parameters in the Study System

Category	Description	Parameter	Value
System	Rated power	P_n	50 VA
	Rated voltage	V_n	20 V L-L RMS
	Nominal frequency	f_n	60 Hz
	DC voltage	V_{dc}	40 V
	Switching frequency	f_{sw}	5 kHz
Passives	Choke inductance	L_f	1.5 mH
	Choke resistance	R_f	70 mΩ
	Choke inductance	$L_f\prime$	2.5 mH
	Choke resistance	$R_f\prime$	44 mΩ
	Shunt capacitance	C_f	47 μF
	RL line inductance	L_g	1.5 mH
	RL line resistance	R_g	70 mΩ
Controller	Inner current control	$K_{p,I}, K_{i,I}$	0.4758, 3.2655
	Power control	$K_{p,P}, K_{i,P}$	0.25, 25
	AC voltage control	$K_{p,V}, K_{i,V}$	0.25, 25
	PLL	$K_{p,PLL}, K_{i,PLL}$	60, 1400
Filter	Measurement filter time constant	T_s	3 ms
	Natural frequency of PLL filter	f_n	25 Hz
	Damping ratio	ζ	0.707

bility, the output power level was curtailed by 50% next at 6.5 seconds. Unexpectedly, an undamped 10 Hz oscillation showed up.

To analyze the oscillation at a low exporting power level, an analytical model was implemented. However, the oscillation mode was not observed. After cross-validation, the only difference noticed was the PLL model. Simple SRF-PLL was first used for analysis. Thus, in the EMT simulation test bed, the basic PLL structure was examined under the same dynamic events. As shown in Fig. 3.24b, no oscillation is observed after curtailing the output power. Therefore, PLL is one of the critical causes of stability issues. Based on the previous PLL model benchmark, the 2^{nd} order filter was added. As result, the 10 Hz oscillation is reproduced and presented in Fig. 3.24c.

Among the 19 real-world sub-synchronous oscillation events collected in [7], such oscillation phenomenon is similar to the 20 Hz oscillation reported in Hydro One's solar PV farm, which is more visible in the morning when generation is low. According to the report, the mentioned oscillation is mitigated by applying faster current control. This strategy is examined in our study test bed, and the simulation results shown in Fig. 3.25 do indicate that faster current control can suppress the 10 Hz oscillation at low power exporting level.

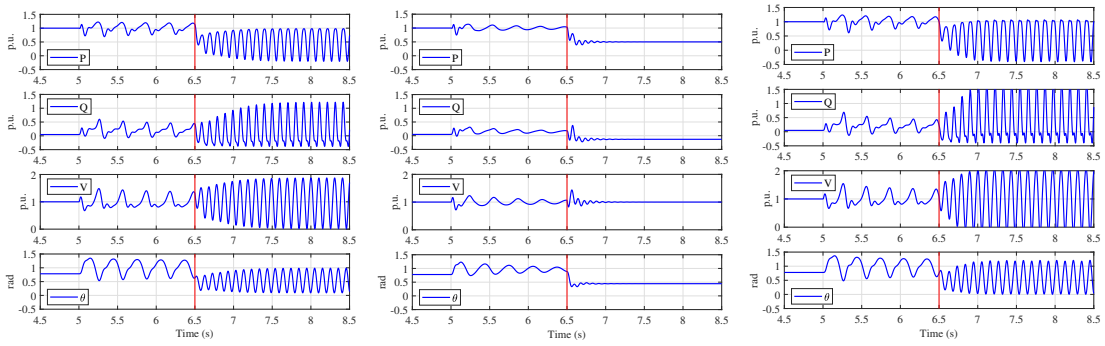

(a) Simscape PLL in use (b) SRF-PLL in use (c) 2^{nd} order filter PLL

Figure 3.24: EMT simulation results.

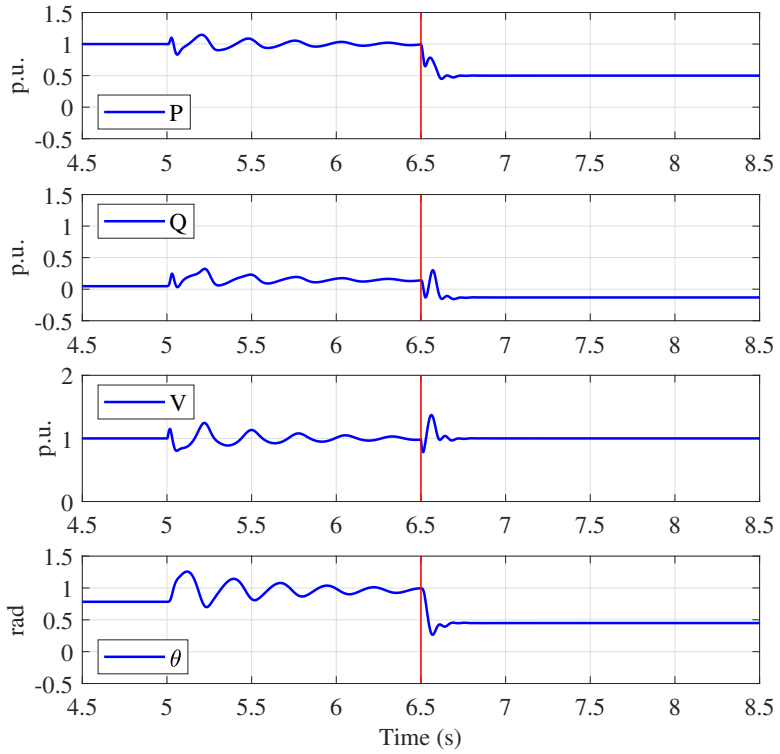

Figure 3.25: EMT simulation results with faster current control.

On the other hand, based on the EMT study results shown in Fig. 3.24 regarding the PLL model structure, it also points out that filters in PLL plays an important role in this stability issue.

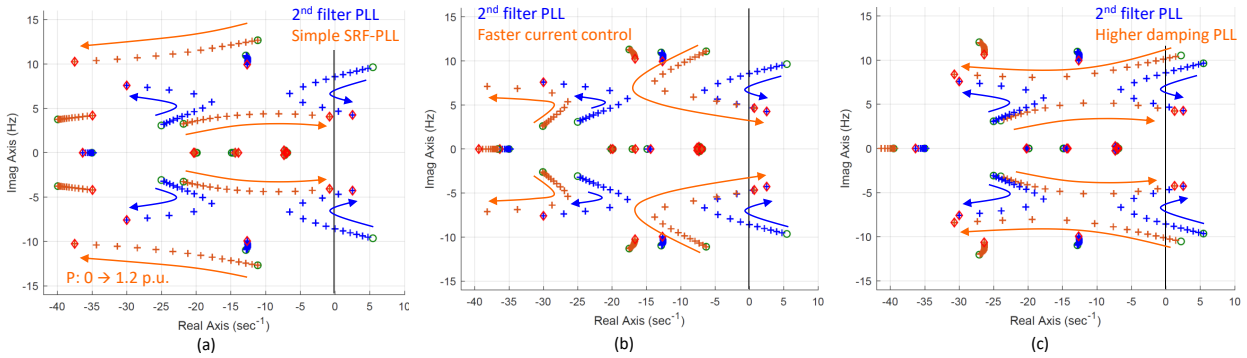

Figure 3.26: Eigenvalue analysis results when output power increases from 0 to 1.2 p.u. with fixed X_g

3.4.2 Analytical Model and Stability Analysis

To compare and analyze the impact of the PLL structure, the *dq*-frame analytical model is carried out. The modeling process has been documented in [12], and it is also described in the previous chapters.

Different PLL models and control parameter setups are examined within the analytical model to verify their influences on the system stability. Fig. 3.26 presents the eigenvalue-loci analysis results for the sensitivity study under four circumstances when the output power increases from 0 to 1.2 p.u.. Only the dominated modes are shown.

Fig. 3.26a shows the SRF-PLL with 2^{nd} order filter can correctly reflect the system is unstable at low and high power levels, whereas the model with Simscape PLL cannot. And the oscillation frequencies matched with the EMT simulation results shown in Fig. 3.24a: 10 Hz oscillation when exporting 0.5 p.u. of power and 4 Hz oscillation when exporting 1 p.u. of power.

The influences from simple SRF-PLL and faster current control compared to the correct original model are presented in Fig. 3.26b and 3.26c respectively. From the comparisons, the traces of eigenvalues with simple SRF-PLL and faster current control both show the system stability margins are improved, which validates the observation from EMT simulation study shown in Fig. 3.24b and 3.24c. Moreover, the rightmost mode in blue separates into one mode moving to the left at a lower frequency and one other mode moving to the right at

a higher frequency as generation increases. Such phenomena are analyzed and presented in our recent study [18].

In addition, a SRF-PLL with 2^{nd} order low-pass filter with stronger damping parameters is examined and compared to the original parameter as shown in Fig. 3.26d. Based on the eigenvalue analysis, it is found that insufficient PLL damping is harmful to the system stability.

To conclude, insufficient damping of PLL due to the filters is analyzed to be one cause of weak oscillation when generation is curtailed. Based on the developed analytical model, stronger PLL damping capability and faster current control are indicated as effective mitigation approaches.

Chapter 4: Weak Grid Oscillation of SVC

4.1 Introduction

Static var compensators (SVCs) have been popularly installed in weak grids to provide voltage support, including a few recent projects in central China. It is well known by the grid industry that large voltage control gain may lead to instability. Analytical models are usually used for eigenvalue analysis, which require additional modeling efforts besides the electromagnetic transient (EMT) simulation test bed setup. In this paper, we use measurements obtained from an EMT simulation test bed to extract the linear model that reflects the relationship between SVC's susceptance command and the point of connection voltage magnitude. Analysis based on the open-loop system consisting of the voltage controller and the learned linear model shows that oscillations are mainly due to the half-cycle time delay introduced by Thyristor switching devices. Increasing voltage control and reducing the system strength push the oscillation mode towards the right half plane (RHP). The measurement-based stability analyses accurately match the simulation results.

Static VAR Compensator, as a controllable power electronics-based reactive power bank, has been widely installed as a type of flexible alternating current transmission systems (FACTs) for voltage support, power factor correction, and system stabilizing.

In 1980s, American Electric Power (AEP) placed two 125-MVAr SVCs in Kentucky to reinforce a 138-kV transmission system [22, 23]. Maine Electric Power Company installed a -125/+425MVAR SVC in the 345-kV system at Chester Maine to support 700 MW importing into the New England network [9].

Oscillation phenomena associated with SVC have also been reported. Both the AEP and the Maine projects reported that harmonics and oscillations may occur along with the

installations of SVCs. Research carried out in 1990s pointed out that the most critical factors are the compensation level, the voltage control parameters, the grid strength, and the time delay due to controller and thyristor firing units [33, 34].

Most recently, the Central Tibet Interconnection Project (CTAIP) in China observed oscillations in EMT simulations of SVCs installed in a long-chain network from center Tibet to Chengdu, Sichuan power grid [39]. Additionally, oscillations appeared in the study of Zangzhong Interconnection in China due to two sets of 60-MVAr SVCs in weak grid [40].

The stability analysis conducted from the above research requires analytical models. Analytical model building, e.g., [25], requires additional efforts for not only modeling but also validation and benchmarking with the EMT test bed. In this paper, we completely rely on a EMT test bed with full details of SVC control and thyristor firing for both time-domain simulation and linear system analysis. Our paper presents measurement-based stability analysis to investigate why large voltage gain and weak grid strength may lead to instability.

4.2 Captured Oscillation of SVC in EMT Simulation

To study an SVC in the weak grid, an EMT testbed shown in Fig. 4.1 is implemented via MATLAB/Simulink with SimPowerSystems Toolbox. This test bed is adapted from the demo SVC detailed model in SimPowerSystem by Pierre Giroux and Gibert Sybille (Hydro-Quebec) [19]. A 200-MW resistive load is connected to a 735-kV infinite bus through a long chain network. The simulation sampling time is 50 μs.

The 16-kV, -100/3000-MVAr SVC structure includes one six-pulse thyristor-controlled reactor (TCR) and three thyristor-controlled capacitors in Δ-connected topology. The SVC is connected to the load bus through an $Y_g - \Delta$ connected 735-kV/16-kV transformer. The SVC is controlled by firing pulses generated according to the voltage regulator shown in Fig. 4.2.

The model is modified to serve the research purpose. Original transmission line short-circuit power is 6000 MVA, and it is lowered to 2000 MVA to represent a weaker grid

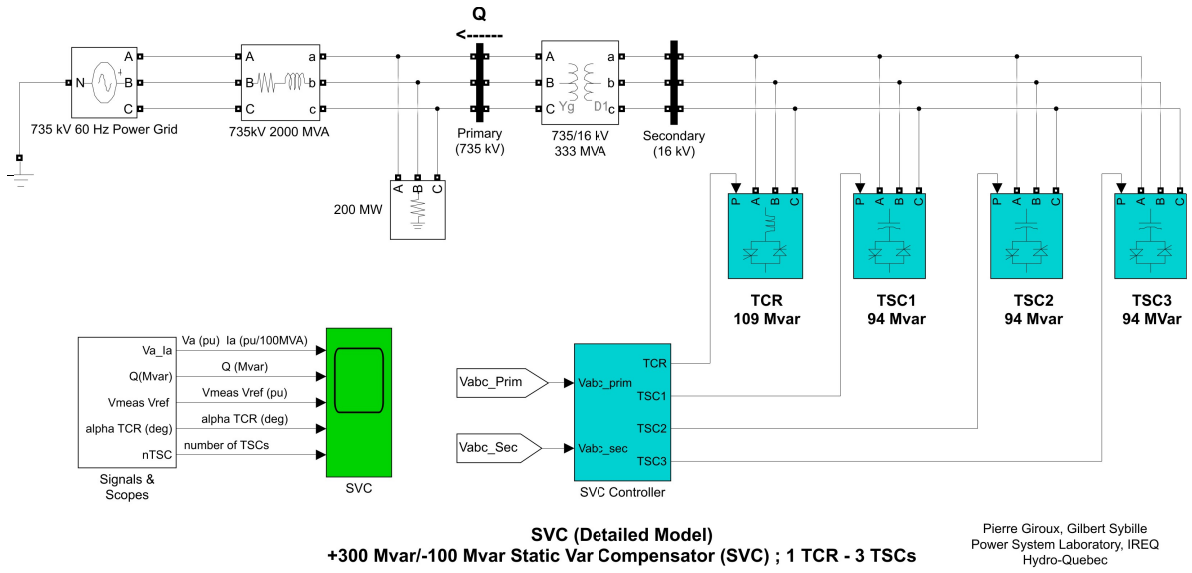

Figure 4.1: Model structure of SVC supported radial network in the demo by Hydro-Quebec with modified short-circuit power of 2000 MVA.

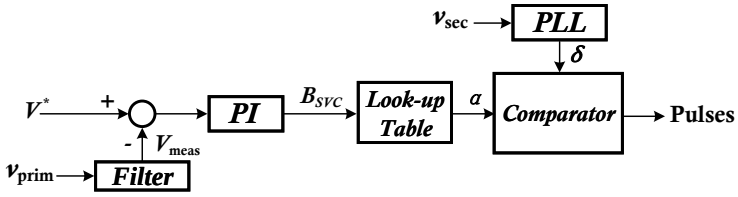

Figure 4.2: SVC controller structure.

connection. The droop gain is set to zero so that the controller only includes the voltage regulator. Default control parameters are $k_p = 0$ and $k_i = 800$, and they are changed to present the oscillation phenomenon. All the modeling parameters are listed in Table. 4.1.

The default line impedance, X_g, is 0.05 p.u. at 100 MVA power base, which is 1 p.u. at short-circuit power base indicates a weak grid strength. Fig. 4.3 presents the simulation results after a step increase of 0.03 p.u. on the voltage reference. The voltage gains are $k_p = 45$ and $k_i = 900$. The spectrum plot shown in Fig. 4.4 indicates that only 36-Hz sub-synchronous oscillation appears in the measurements of voltage magnitude and reactive power output by SVC, and both 24-Hz and 96-Hz oscillations exist in the ac current flows from the SVC.

Table 4.1: Parameters of the EMT Testbed

Category	Description	Parameter	Value
System	Rated Power	P_n	100 MVA
	Short-circuit Power	P_{sc}	2000 MVA
	Rated Voltage	V_n	735 kV, 16 kV
	Nominal Frequency	f_n	60 Hz
Passives	X/R ratio	X/R	10
	Line reactance	X_g	0.05 p.u.
	Line resistance	R_g	0.005 p.u.
	Load	P_{load}	200 MW
Controller	PLL-driven Filter	$k_{p,pll1}, k_{i,pll1}$	60, 1400
	Comparator PLL	$k_{k,pll2}, k_{i,pll2}$	120, 2800
	Voltage Regulator	k_p, k_i	10, 200
	Average Switching Delay	T_d	2.5 ms

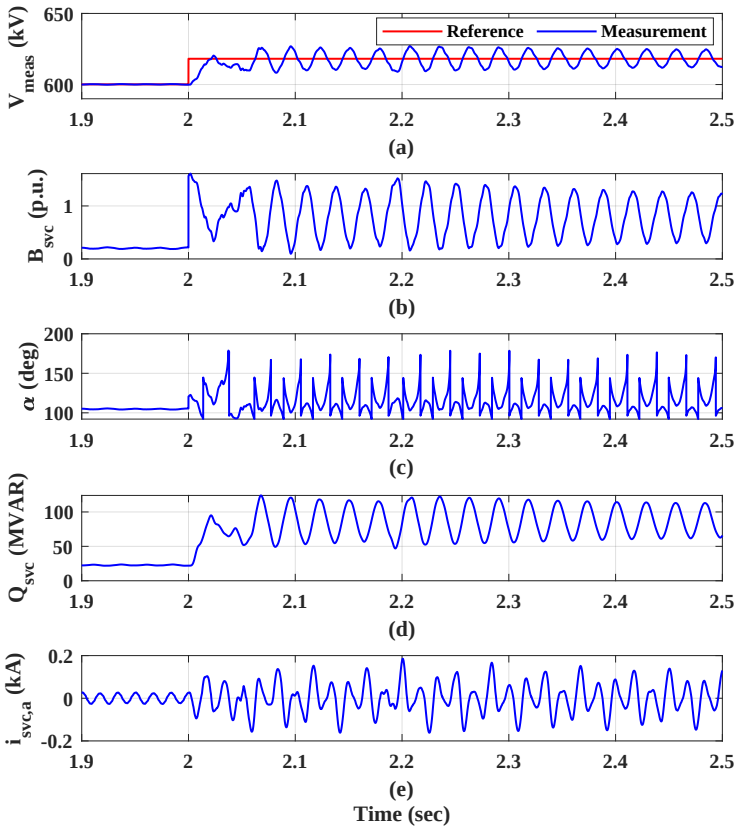

Figure 4.3: Voltage reference increases by 0.03 p.u..

4.2.1 Critical Factors

In order to understand the potential causes of the oscillation and tackle this problem, time-domain experiments are done within the EMT simulation. The following critical factors and their influences are presented and compared.

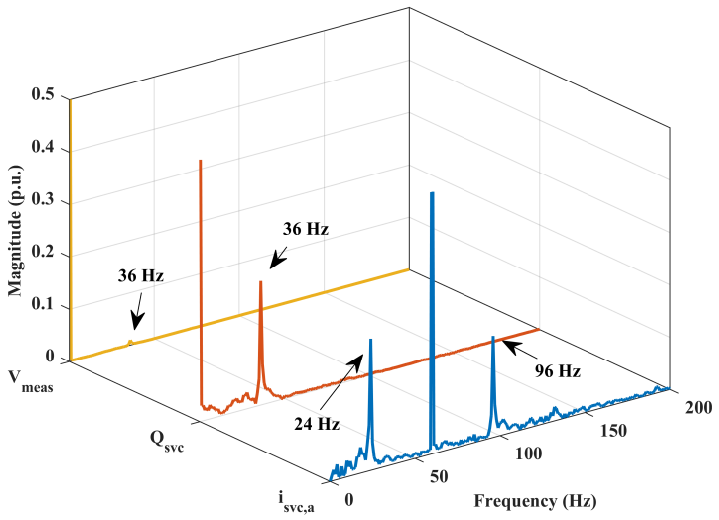

Figure 4.4: Spectrum of each time-domain measurement.

4.2.1.1 Control Parameters

At 2 seconds, the voltage regulator gains are increased to as the following $k_p = 64$, $k_i = 1280$. At 3 seconds, both the proportional and integral gains are enlarged again to $k_p = 65$ and $k_i = 1300$. The simulation results are shown in Fig. 4.5. According to the measurements, undamped oscillation appears and stays after the gains are enlarged. The oscillation frequencies did not change by much before and after the gain increase. Therefore, the tuning of the voltage regulator's control parameters can cause the system instability, and the oscillation frequency will not be affected by much.

4.2.1.2 Grid Strength

On the network side, the grid strength is also important. To investigate the impact of grid strength, the line impedance (X_g) is set to 0.075 and 0.1 p.u. respectively with the same control parameters: $k_p = 25$ and $k_i = 500$. The simulation results of voltage magnitude (V_{meas}) are compared and presented in Fig. 4.6. According to the observation, the system remains stable in both scenarios. However, the oscillation frequency is higher when X_g is higher.

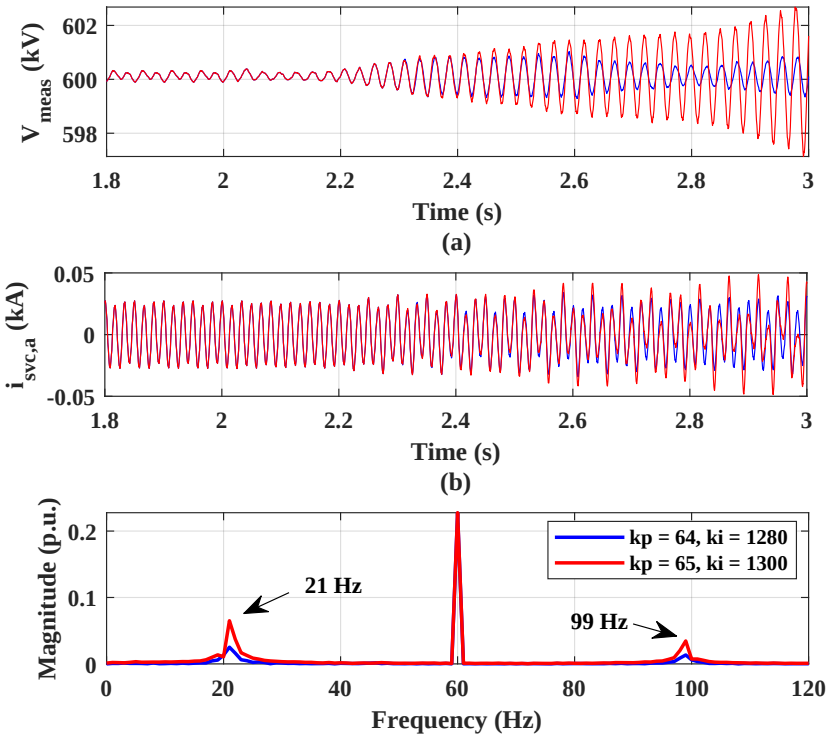

Figure 4.5: Control parameters increase at 2 seconds.

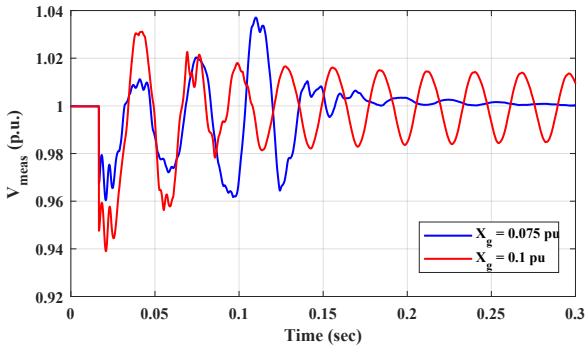

Figure 4.6: Plot of V_{meas} when line impedance are 0.075 p.u..

4.3 Measurement-based Linear Model Extraction

In order to conduct further analysis to investigate the oscillation phenomena, the linear model of the system is essential. In this paper, the linear models are obtained via both time-domain and frequency-domain data for a measurement test bed. The feedback system structure is shown in Fig. 4.7, where the circuit model and firing unit are considered as one

SISO model, $G(s)$. $G(s)$ will be estimated using measurement data. The measurement test bed is built by disabling the voltage control of the SVC. The only control signal from the SVC is the fixed B_{SVC} command. A step response or sinusoidal harmonic will be injected into this command. The system's response, e.g., the POI voltage magnitude, will be recorded.

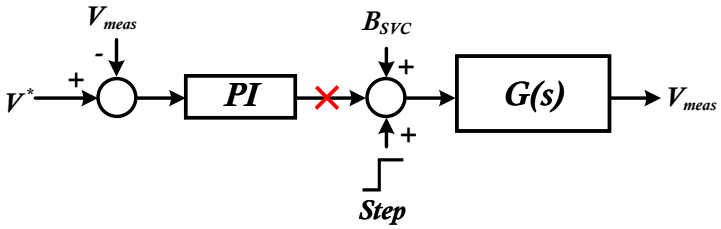

Figure 4.7: Block diagram of measurement testbed topology.

4.3.1 Time-domain Data and Processing

At steady-state, an 0.1 p.u. of step change is given on B_{SVC} after the PI controller is disconnected. The measurement of the filtered voltage magnitude from the EMT simulation is taken as the output signal. Fig. 4.8 presents the measurement data of the susceptance command B_{SVC} and the POI voltage V_{meas} at different line impedance levels.

The System Identification Toolbox's `tfest` function is applied to estimate the input and output model $G(s)$. The estimation results are compared with the measurement data in Fig. 4.9, and the degree of matching is `94.95%` and indicates the accuracy of the estimated model.

In Fig. 4.9, the measurement data from the simulation due to the step change does not include many dynamic impacts, thus the estimation order shall be low. After a few attempts, it is found that the estimation provides better fitting result when the IO delay is considered, which also allows a lower order for the estimation. The final setup is a second-order linear model with 2 poles, 1 zero, and an 0.0025 seconds of IO delay, and estimated model is shown

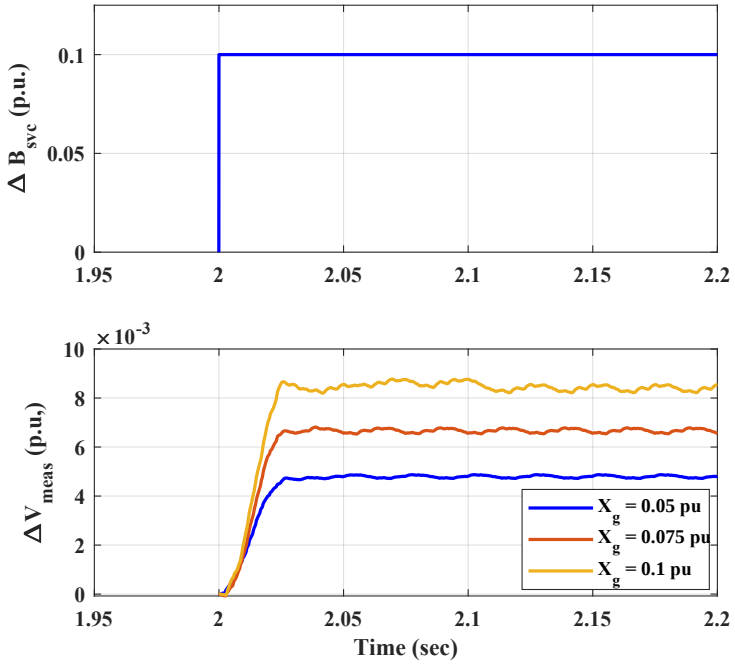

Figure 4.8: EMT simulation measurements corresponding to step change events at different X_g.

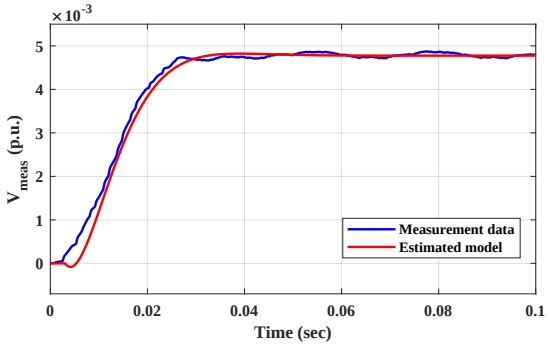

Figure 4.9: Step responses matching among the EMT simulation measurement data and estimated model.

as follows.

$$G(s) = \mathbf{exp}(-0.0025s)\frac{-1.256s + 1198}{s^2 + 262.3s + 2.502e04}. \tag{4.1}$$

The obtained model is a second-order system with delay for $G(s) = \frac{V_{meas}}{B_{SVC}}$. For the widely adopted CIGRE model for RMS-based dynamic simulation, the transfer function between

the susceptance and the commend is as follows [1]:

$$B_{SVC} = \frac{e^{-T_d s}}{1 + Ts} B^*_{SVC} \tag{4.2}$$

where T_d is related to digital control delay and is assumed to be 1 ms. T includes thyristor firing delay and is in the range of 3 ms to 6 ms.

If this model is adopted, it can be seen $G(s)$ is also in the format of a first-order system with a delay. Apparently, from measurement-based estimation, a second-order system with a delay can better capture the dynamics. In our future research, why the second-order system with a delay can provide a better representation will be further investigated using analytical derivation approach.

4.3.2 Stability Analysis

Three sets of stability analysis (the root-locus method, the Bode plots, and the closed-loop eigenvalue analysis) are performed to validate the estimated model and produce detailed assessment on the major critical impact factors mentioned previously.

4.3.3 Root-locus Analysis

As the controller dynamic is separated from the system when performing the frequency-scan, $G(s)$ obtained from estimation does not include the control dynamic, expressed as $C(s) = 10 + 200/s$. Therefore, Root-locus analysis is performed on the open-loop system $OL(s)$ after adding back the control dynamics:

$$OL(s) = G(s) \cdot C(s).$$

The root-locus method can easily examine the impact the controller gain on stability. Note that MATLAB's `rlocus` command does not work with model includes IO delay. Thus,

the IO delay was manually removed and added back in the Pade approximation expression $T_d(s) = \frac{1-T_d/2s}{1+T_d/2s}$, where T_d is the 0.0025 seconds delay time [20].

Fig. 4.10 presents the root-locus analysis plot, where the blue trajectory indicates the closed-loop system pole location while voltage regulator gain increases with the original firing delay, and the red trajectory addresses that when an additional 0.0025 seconds delay is implemented. The marginal point of the blue line shows that the system is unstable and oscillating at 42.1 Hz when the controller gains are increased by 6.6 times, which agrees with the EMT simulation results shown in Fig. 4.5. Moreover, the root-locus plot comparison clearly points out the time delay significantly lowered the stability margin on control gains and the oscillation frequency.

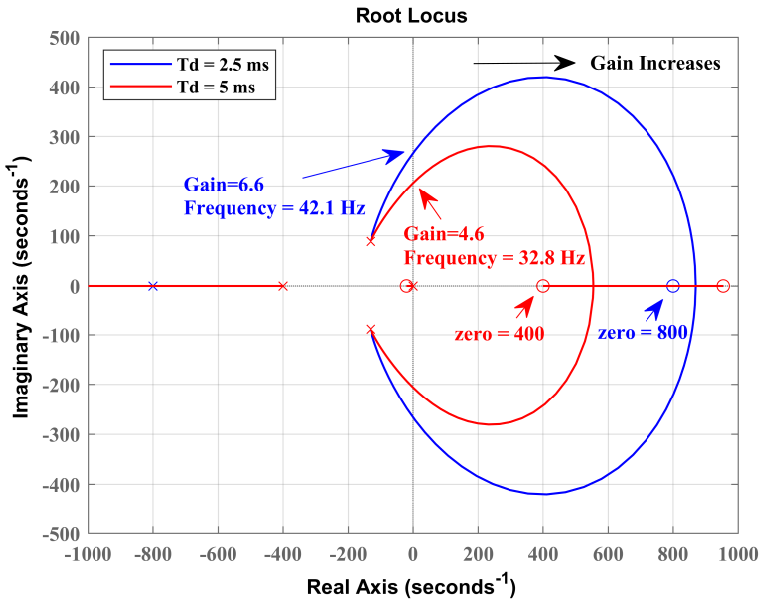

Figure 4.10: Root locus plot of the system with various delay.

It can be seen clearly in the root loci plots that the system has an open-loop zero located in the RHP. This zero is introduced by the delay and attracts a pair of complex conjugate eigenvalues (the oscillation mode) moving toward the RHP. Increasing the delay makes the RHP zero more close to the original point and provides more attracting force to the oscillation modes.

4.3.4 Bode Plot Analysis

Sensitivity analysis can also be performed via frequency responses comparison. In Fig. 4.11, the open-loop system ($G(s)$) frequency-responses with 0.05 and 0.1 p.u. line impedance are plotted together with the inverse of control dynamic ($1/C(s)$) with enlarged gains of 2.5 and 6.5 times respectively. The marked intersection points closely match to EMT simulation results shown in Fig. 4.5 (dotted blue line vs solid red line) and 4.6 (solid blue line vs dotted red line) respectively.

It can be seen that increasing the line impedance or increasing the controller gain all lead to larger cross-over frequencies with larger phase difference, indicating worse stability.

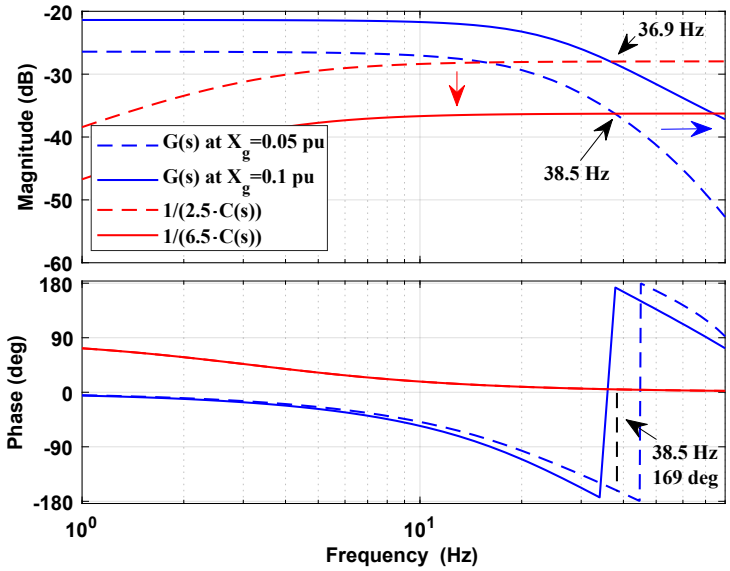

Figure 4.11: Bode plots for sensitivity analysis against control parameters and grid impedance.

4.3.5 Eigenvalue-loci Analysis

In addition to the stability analysis conducted to identify the impact of major aspects, the following eigenvalue-based analysis based on the closed-loop system ($CL(s)$) reveals the stability influences due to the proportional gain and integral gain respectively. Based on the estimated linear model $G(s)$, the controller transfer function $C(s)$, the closed-loop system is

as follows:

$$CL(s) = \frac{C(s)G(s)}{1 + C(s)G(s)}.$$

By increasing the proportional and integral gain individually, the system eigenvalues move to the right-half plane gradually as shown in Fig. 4.12. From comparison, it presents that system becomes unstable when proportional gain is increased by 7 times, while the increased integral gain did not cause instability. Also, the unstable marginal oscillation frequency is observed to be seriously affected by the value of the proportional gain. It is indicated that the proportional gain tuning is more sensitive and critical than the integral gain, which agrees with other literature [33, 34, 39].

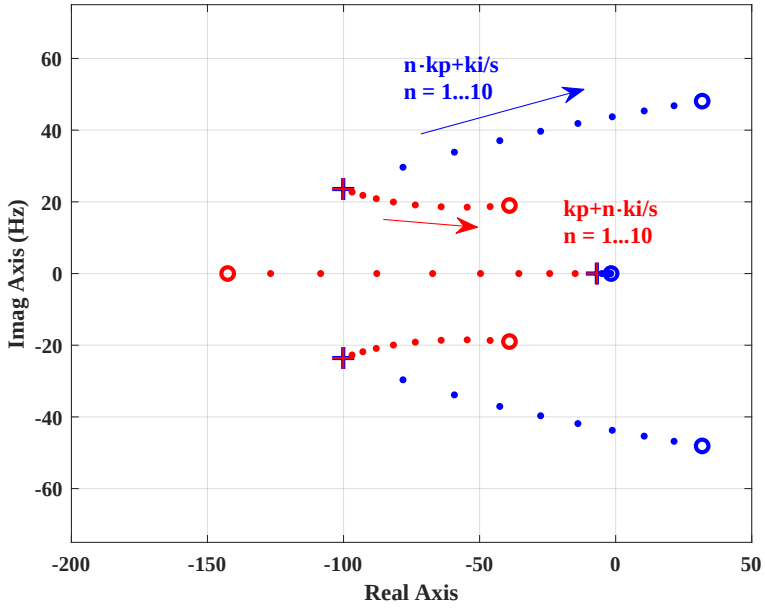

Figure 4.12: Eigenvalue-loci plot of the closed-loop system to compare impacts of proportional gain and integral gain.

To summarize, the sub-synchronous oscillations in SVC integrated weak grid is investigated and presented in this part of dissertation. Based on the linear model extracted from the measurement data based on an EMT testbed, it can be concluded that the root causes of oscillations are mainly due to the thyristor firing unit delay at a scale of 2.5 ms. This

delay contributes a zero in the RHP. Increasing the voltage control gain will make a pair of eigenvalues move toward the RHP.

Chapter 5: Conclusion and Future Work

5.1 Conclusion

This dissertation is motivated by real-world stability events regarding inverter-based renewable energy resources. And the research behind the dissertation is committed to conducting stability analysss of grid-connected IBRs in various operation conditions. Accomplished work that is presented includes the dynamic studies in single-IBR integrated systems and FACT device integrated systems. Research approach starts with replications of low-frequency events under different operating scenarios, then conducting stability analyses based on extracted linear models, and finally cross-validated with experiments. The major causes of instability in GFL IBR integrate systems from documented research incorporates grid strength, tuning of controllers, time delay, synchronization tool design, etc.

The dissertation work reveals the following critical factors that can lead to IBR integrated system instability: weak grid strength due to long transmission lines, poor controller gain tuning, and insufficient damping of PLL. Reinforcing the grid strength by upgrading the existing transmission network should be the best option. However, due to the high cost, appropriate controller and PLL tuning shall be required. The value of this dissertation work is to bring multiple sets of examples of some of the most observed weak grid oscillations in the grid-connected IBR integrated systems, as well as mitigation guidelines.

5.2 Future Work

In the future, more investigations on a few different topics have been planned. First of all, there are more PLLs with different implementation structures that are used in the

real-world inverter controller. One of the future study topics will focus on the investigation of different PLLs and their characters and influences. Secondly, the current dissertation work only presents one type of weak grid stability issue, where more types of events are reported. Investigations on other types of oscillations, interactions, etc are also planned in future work.

References

[1] Static var compensator models for power flow and dynamic performance simulation. *IEEE Transactions on Power Systems*, 9(1):229–240, 1994.

[2] Anas Almunif, Lingling Fan, and Zhixin Miao. A tutorial on data-driven eigenvalue identification: Prony analysis, matrix pencil, and eigensystem realization algorithm. *International Transactions on Electrical Energy Systems*, 30(4):e12283, 2020.

[3] Li Bao, Lingling Fan, Zhixin Miao, and Zhengyu Wang. Hardware demonstration of weak grid oscillations in grid-following converters. In *2021 North American Power Symposium (NAPS)*, pages 01–06, 2021.

[4] Li Bao, Lingling Fan, Zhixin Miao, and Zhengyu Wang. Hardware demonstration of weak grid oscillations in grid-following converters. In *2021 North American Power Symposium (NAPS)*, pages 01–06, 2021.

[5] Mohamed Belkhayat. *Stability criteria for AC power systems with regulated loads*. PhD thesis, Purdue University West Lafayette, NI, 1997.

[6] Yunzhi Cheng, Lingling Fan, Jonathan Rose, Fred Huang, John Schmall, Xiaoyu Wang, Xiaorong Xie, Jan Shair, Jayanth Ramamurthy, Nilesh Modi, Chun Li, Chen Wang, Shahil Shah, Bikash Chandra Pal, Zhixin Miao, Andrew Isaacs, Jean Mahseredjian, and Zheng Jenny Zhou. Real-world subsynchronous oscillation events in power grids with high penetrations of inverter-based resources. *IEEE Transactions on Power Systems*, pages 1–1, 2022.

[7] Yunzhi Cheng, Lingling Fan, Jonathan Rose, Fred Huang, John Schmall, Xiaoyu Wang, Xiaorong Xie, Jan Shair, Jayanth Ramamurthy, Nilesh Modi, Chun Li, Chen Wang, Shahil Shah, Bikash Chandra Pal, Zhixin Miao, Andrew Isaacs, Jean Mahseredjian, and Zheng Jenny Zhou. Real-world subsynchronous oscillation events in power grids with high penetrations of inverter-based resources. *IEEE Transactions on Power Systems*, pages 1–1, 2022.

[8] Yu Cui and Wilsun Xu. Harmonic resonance mode analysis using real symmetrical nodal matrices. *IEEE Transactions on Power Delivery*, 22(3):1989–1990, 2007.

[9] D.L. Dickmander, B.H. Thorvaldsson, G.A. Stromberg, D.L. Osborn, A.E. Poitras, and D.A. Fisher. Control system design and performance verification for the chester, maine static var compensator. *IEEE Transactions on Power Delivery*, 7(3):1492–1503, 1992.

[10] Huazhao Ding, Zhengyu Wang, Lingling Fan, and Zhixin Miao. Modeling and control of grid-following single-phase voltage-sourced converter. In *2020 52nd North American Power Symposium (NAPS)*, pages 1–6, 2021.

[11] Lingling Fan. Modeling type-4 wind in weak grids. *IEEE Transactions on Sustainable Energy*, 10(2):853–864, 2018.

[12] Lingling Fan. Modeling type-4 wind in weak grids. *IEEE Transactions on Sustainable Energy*, 10(2):853–864, 2019.

[13] Lingling Fan and Zhixin Miao. Wind in weak grids: 4 hz or 30 hz oscillations? *IEEE Transactions on Power Systems*, 33(5):5803–5804, 2018.

[14] Lingling Fan and Zhixin Miao. Admittance-based stability analysis: Bode plots, Nyquist diagrams or eigenvalue analysis? *IEEE Transactions on Power Systems*, 35(4):3312–3315, 2020.

[15] Lingling Fan and Zhixin Miao. A modular small-signal analysis framework for inverter penetrated power grids: Measurement, assembling, aggregation, and stability assessment. https://arxiv.org/abs/2003.03860, 2020.

[16] Lingling Fan and Zhixin Miao. Time-domain measurement-based *dq*-frame admittance model identification for inverter-based resources. *IEEE Transactions on Power Systems*, 36(3):2211–2221, 2021.

[17] Lingling Fan, Zhixin Miao, Shahil Shah, Yunzhi Cheng, Jonathan Rose, Shun-Hsien Huang, Bikash Pal, Xiaorong Xie, Nilesh Modi, Song Wang, and Songzhe Zhu. Real-world 20-hz ibr subsynchronous oscillations: Signatures and mechanism analysis. *IEEE Transactions on Energy Conversion*, pages 1–11, 2022.

[18] Lingling Fan, Zhixin Miao, and Zhengyu Wang. A new type of weak grid ibr oscillations. *IEEE Transactions on Power Systems*, pages 1–4, 2022.

[19] Pierre Giroux and Gibert Sybille. Svc detailed model.

[20] Gene H Golub and Charles F Van Loan. Matrix computations. johns hopkins studies in the mathematical sciences.

[21] B. Gustavsen and A. Semlyen. Rational approximation of frequency domain responses by vector fitting. *IEEE Transactions on Power Delivery*, 14(3):1052–1061, 1999.

[22] R. Gutman, J. J. Keane, M. E. Rahman, and O. Veraas. Application and operation of a static var system on a power system american electric power experience, part i: System studies experience, system. *IEEE Power Engineering Review*, PER-5(7):55–56, 1985.

[23] R. Gutman, J. J. Keane, M. Ea. Rahman, and O. Veraas. Application and operation of a static var system on a power system americal electric power experience part ii: Equipment design and installation. *IEEE Transactions on Power Apparatus and Systems*, PAS-104(7):1875–1881, 1985.

[24] Zhenyu Huang, Yu Cui, and Wilsun Xu. Application of modal sensitivity for power system harmonic resonance analysis. *IEEE Transactions on Power Systems*, 22(1):222–231, 2007.

[25] Dragan Jovcic, Nalin Pahalawaththa, Mohamed Zavahir, and Heba A Hassan. Svc dynamic analytical model. *IEEE transactions on power delivery*, 18(4):1455–1461, 2003.

[26] Yin Li, Lingling Fan, and Zhixin Miao. Wind in weak grids: Low-frequency oscillations, subsynchronous oscillations, and torsional interactions. *IEEE Transactions on Power Systems*, 35(1):109–118, 2020.

[27] Yin Li, Lingling Fan, and Zhixin Miao. Wind in weak grids: Low-frequency oscillations, subsynchronous oscillations, and torsional interactions. *IEEE Transactions on Power Systems*, 35(1):109–118, 2020.

[28] L. Ljung. State of the art in linear system identification: time and frequency domain methods. In *Proceedings of the 2004 American Control Conference*, volume 1, pages 650–660 vol.1, 2004.

[29] Lennart Ljung. Frequency domain versus time domain methods in system identification–revisited. In *Control of Uncertain Systems: Modelling, Approximation, and Design*, pages 277–291. Springer, 2006.

[30] NERC. Reliability guideline forced oscillation monitoring and mitigation. 2017.

[31] Joint NERC and WECC Staff. 900 mw fault induced solar photovoltaic resource interruption disturbance report:southern california event: October 9, 2017. 2018.

[32] Joint NERC and WECC Staff. San fernando disturbance, south california event: July 7, 2020. 2020.

[33] M Parniani and MR Iravani. Voltage control stability and dynamic interaction phenomena of static var compensators. *IEEE transactions on power systems*, 10(3):1592–1597, 1995.

[34] A.J.P. Ramos and H. Tyll. Dynamic performance of a radial weak power system with multiple static var compensators. *IEEE Transactions on Power Systems*, 4(4):1316–1325, 1989.

[35] AI Semlyen. S-domain methodology for assessing the small signal stability of complex systems in nonsinusoidal steady state. *IEEE Transactions on Power Systems*, 14(1):132–137, 1999.

[36] A Shafiu, O Anaya-Lara, G Bathurst, and N Jenkins. Aggregated wind turbine models for power system dynamic studies. *Wind engineering*, 30(3):171–185, 2006.

[37] A. Shafiu, O. Anaya-Lara, G. Bathurst, and N. Jenkins. Aggregated wind turbine models for power system dynamic studies. *Wind Engineering*, 30(3):171–185, 2006.

[38] Shahil Shah, Przemyslaw Koralewicz, Vahan Gevorgian, Hanchao Liu, and Jian Fu. Impedance methods for analyzing stability impacts of inverter-based resources: Stability analysis tools for modern power systems. *IEEE Electrification Magazine*, 9(1):53–65, 2021.

[39] Huabo Shi, Xinwei Sun, Gang Chen, Hua Zhang, Yonghong Tang, Lin Xu, Lijie Ding, Chengwei Fan, and Yin Xu. Optimization strategy of svc for eliminating electromagnetic oscillation in weak networking power systems. *Energies*, 12(18):3489, 2019.

[40] Xinwei Sun, Bo Zhou, Pengyin Liu, Xiaorong Xie, Jan Shair, Xiaoqing Chang, and Wei Wei. Investigating sub-and super-synchronous interaction between static var compensators and a weak ac grid. In *The 16th IET International Conference on AC and DC Power Transmission (ACDC 2020)*, volume 2020, pages 639–644. IET, 2020.

[41] IEEE PES WindSSO Taskforce. PES TR-80: Wind energy systems subsynchronous oscillations: Events and modeling. 2020.

[42] Virgilio Valdivia, Antonio Lázaro, Andrés Barrado, Pablo Zumel, Cristina Fernández, and Marina Sanz. Impedance identification procedure of three-phase balanced voltage source inverters based on transient response measurements. *IEEE Transactions on Power Electronics*, 26(12):3810–3816, 2011.

[43] Zhengyu Wang, Li Bao, Lingling Fan, Zhixin Miao, and Shahil Shah. From event data to wind power plant dq admittance and stability risk assessment. *IEEE Transactions on Power Systems*, pages 1–1, 2022.

[44] Zhengyu Wang, Zhixin Miao, and Lingling Fan. Practical start-up process of multiple grid-tied voltage-sourced inverters in laboratory. In *2021 North American Power Symposium (NAPS)*, pages 1–6, 2021.

[45] Bo Wen, Dushan Boroyevich, Rolando Burgos, Paolo Mattavelli, and Zhiyu Shen. Analysis of dq small-signal impedance of grid-tied inverters. *IEEE Transactions on Power Electronics*, 31(1):675–687, 2015.

[46] Y. Xu, M. Zhang, L. Fan, and Z. Miao. Small-signal stability analysis of type-4 wind in series-compensated networks. *IEEE Transactions on Energy Conversion*, 35(1):529–538, 2020.

[47] Amirnaser Yazdani and Reza Iravani. *Voltage-sourced converters in power systems: modeling, control, and applications*. John Wiley & Sons, 2010.

[48] L. Zhang, L. Harnefors, and H. P. Nee. Power-synchronization control of grid-connected voltage-source converters. *IEEE Transactions on Power Systems*, 25(2):809–820, May 2010.

[49] Miao Zhang, Zhixin Miao, and Lingling Fan. Reduced-order analytical models of grid-connected solar photovoltaic systems for low-frequency oscillation analysis. *IEEE Transactions on Sustainable Energy*, 12(3):1662–1671, 2021.

Appendix A: Copyright Permissions

The permission below is for the reproduction of material in Chapter 2.

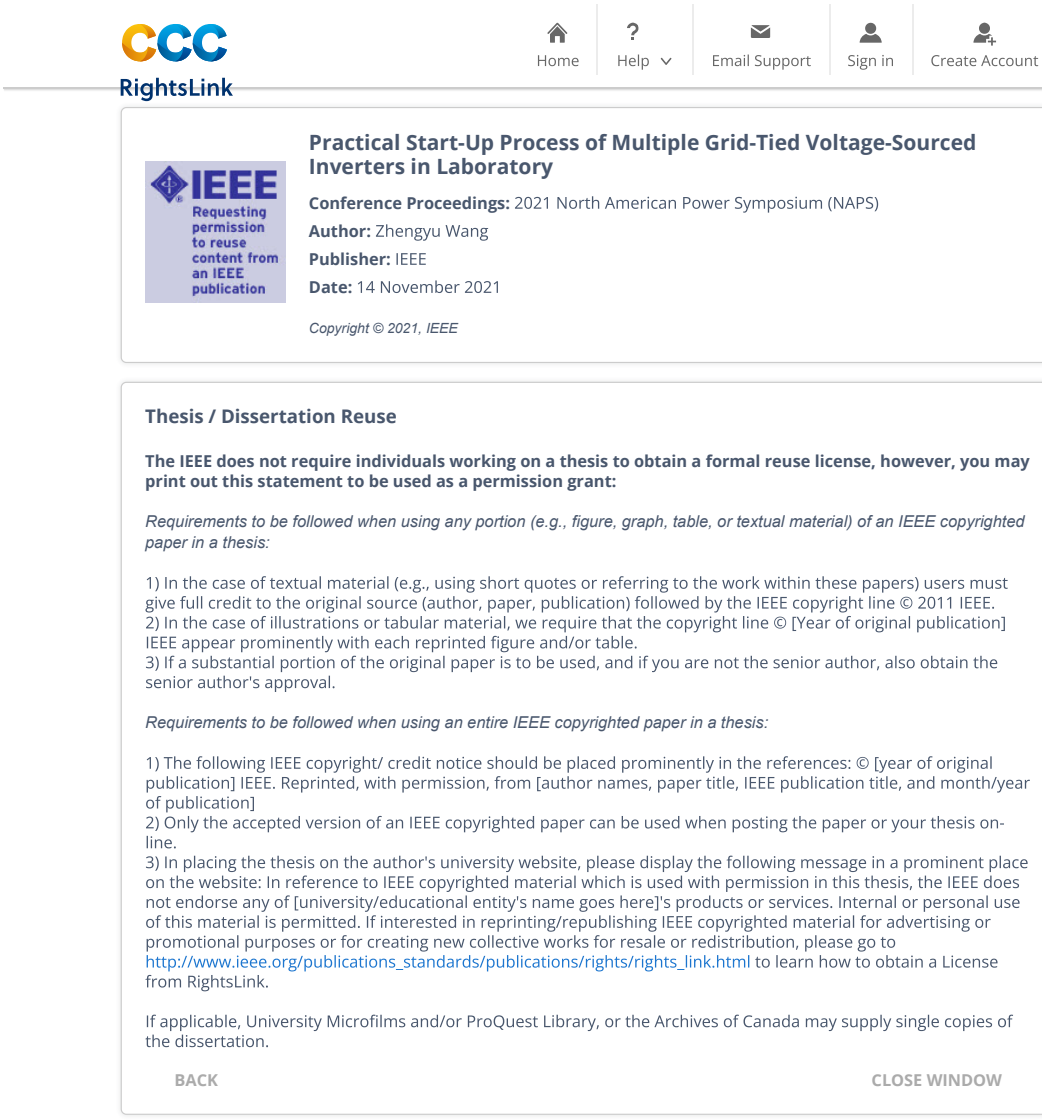

CCC RightsLink

Home | Help | Email Support | Sign in | Create Account

IEEE Requesting permission to reuse content from an IEEE publication

Practical Start-Up Process of Multiple Grid-Tied Voltage-Sourced Inverters in Laboratory

Conference Proceedings: 2021 North American Power Symposium (NAPS)
Author: Zhengyu Wang
Publisher: IEEE
Date: 14 November 2021

Copyright © 2021, IEEE

Thesis / Dissertation Reuse

The IEEE does not require individuals working on a thesis to obtain a formal reuse license, however, you may print out this statement to be used as a permission grant:

Requirements to be followed when using any portion (e.g., figure, graph, table, or textual material) of an IEEE copyrighted paper in a thesis:

1) In the case of textual material (e.g., using short quotes or referring to the work within these papers) users must give full credit to the original source (author, paper, publication) followed by the IEEE copyright line © 2011 IEEE.
2) In the case of illustrations or tabular material, we require that the copyright line © [Year of original publication] IEEE appear prominently with each reprinted figure and/or table.
3) If a substantial portion of the original paper is to be used, and if you are not the senior author, also obtain the senior author's approval.

Requirements to be followed when using an entire IEEE copyrighted paper in a thesis:

1) The following IEEE copyright/ credit notice should be placed prominently in the references: © [year of original publication] IEEE. Reprinted, with permission, from [author names, paper title, IEEE publication title, and month/year of publication]
2) Only the accepted version of an IEEE copyrighted paper can be used when posting the paper or your thesis on-line.
3) In placing the thesis on the author's university website, please display the following message in a prominent place on the website: In reference to IEEE copyrighted material which is used with permission in this thesis, the IEEE does not endorse any of [university/educational entity's name goes here]'s products or services. Internal or personal use of this material is permitted. If interested in reprinting/republishing IEEE copyrighted material for advertising or promotional purposes or for creating new collective works for resale or redistribution, please go to http://www.ieee.org/publications_standards/publications/rights/rights_link.html to learn how to obtain a License from RightsLink.

If applicable, University Microfilms and/or ProQuest Library, or the Archives of Canada may supply single copies of the dissertation.

BACK CLOSE WINDOW

The permission below is for the reproduction of material in Chapter 2 and 3.

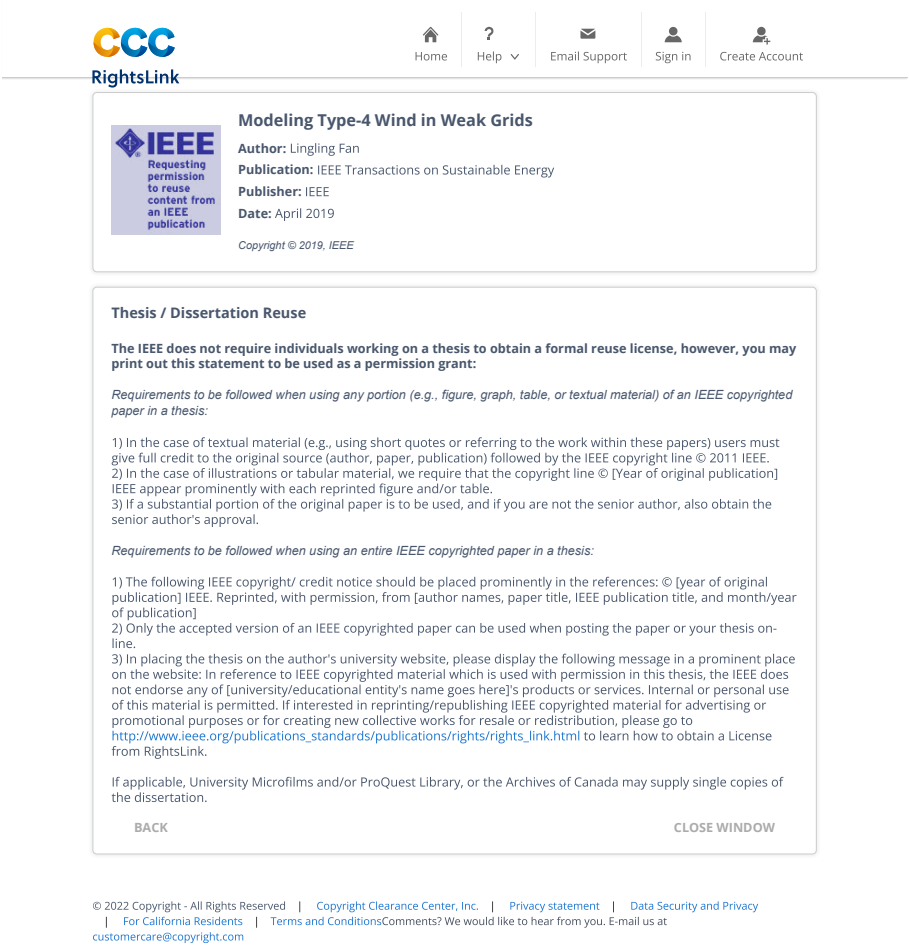

CCC RightsLink

Home | Help | Email Support | Sign in | Create Account

IEEE Requesting permission to reuse content from an IEEE publication

Modeling Type-4 Wind in Weak Grids

Author: Lingling Fan
Publication: IEEE Transactions on Sustainable Energy
Publisher: IEEE
Date: April 2019

Copyright © 2019, IEEE

Thesis / Dissertation Reuse

The IEEE does not require individuals working on a thesis to obtain a formal reuse license, however, you may print out this statement to be used as a permission grant:

Requirements to be followed when using any portion (e.g., figure, graph, table, or textual material) of an IEEE copyrighted paper in a thesis:

1) In the case of textual material (e.g., using short quotes or referring to the work within these papers) users must give full credit to the original source (author, paper, publication) followed by the IEEE copyright line © 2011 IEEE.
2) In the case of illustrations or tabular material, we require that the copyright line © [Year of original publication] IEEE appear prominently with each reprinted figure and/or table.
3) If a substantial portion of the original paper is to be used, and if you are not the senior author, also obtain the senior author's approval.

Requirements to be followed when using an entire IEEE copyrighted paper in a thesis:

1) The following IEEE copyright/ credit notice should be placed prominently in the references: © [year of original publication] IEEE. Reprinted, with permission, from [author names, paper title, IEEE publication title, and month/year of publication]
2) Only the accepted version of an IEEE copyrighted paper can be used when posting the paper or your thesis on-line.
3) In placing the thesis on the author's university website, please display the following message in a prominent place on the website: In reference to IEEE copyrighted material which is used with permission in this thesis, the IEEE does not endorse any of [university/educational entity's name goes here]'s products or services. Internal or personal use of this material is permitted. If interested in reprinting/republishing IEEE copyrighted material for advertising or promotional purposes or for creating new collective works for resale or redistribution, please go to http://www.ieee.org/publications_standards/publications/rights/rights_link.html to learn how to obtain a License from RightsLink.

If applicable, University Microfilms and/or ProQuest Library, or the Archives of Canada may supply single copies of the dissertation.

BACK CLOSE WINDOW

The permission below is for the reproduction of material in Chapter 3.

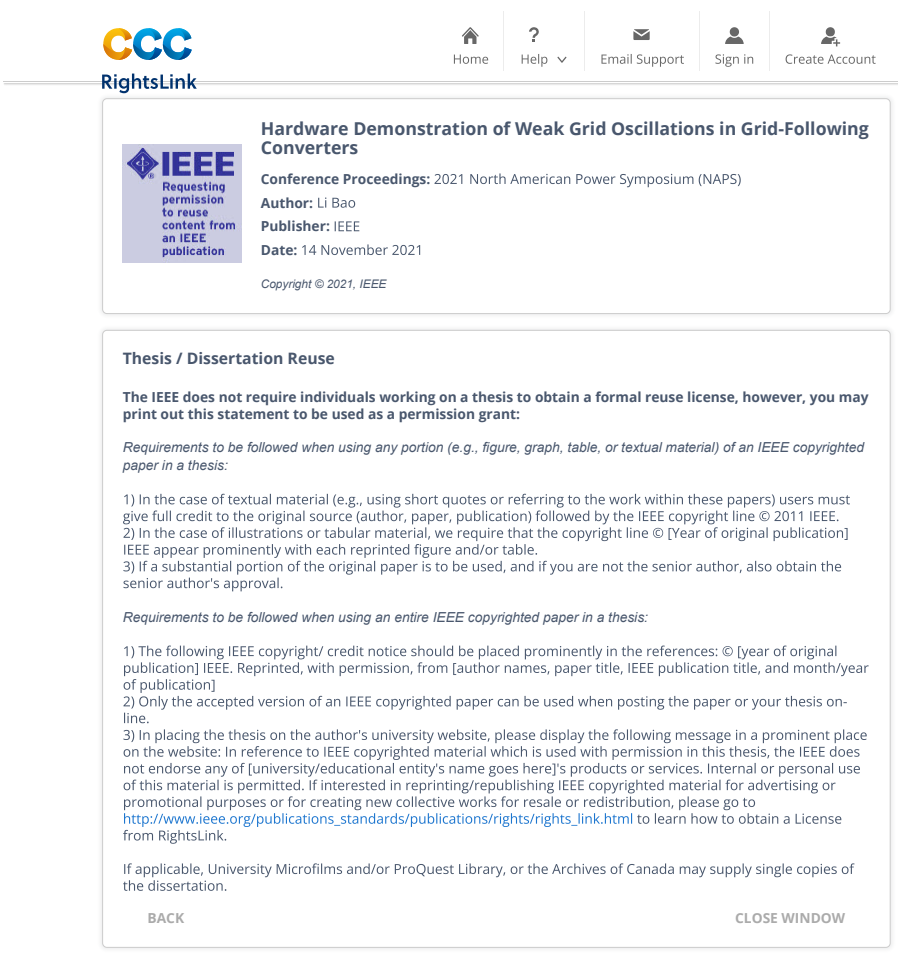

CCC RightsLink

Home | Help | Email Support | Sign in | Create Account

IEEE Requesting permission to reuse content from an IEEE publication

Hardware Demonstration of Weak Grid Oscillations in Grid-Following Converters

Conference Proceedings: 2021 North American Power Symposium (NAPS)

Author: Li Bao

Publisher: IEEE

Date: 14 November 2021

Copyright © 2021, IEEE

Thesis / Dissertation Reuse

The IEEE does not require individuals working on a thesis to obtain a formal reuse license, however, you may print out this statement to be used as a permission grant:

Requirements to be followed when using any portion (e.g., figure, graph, table, or textual material) of an IEEE copyrighted paper in a thesis:

1) In the case of textual material (e.g., using short quotes or referring to the work within these papers) users must give full credit to the original source (author, paper, publication) followed by the IEEE copyright line © 2011 IEEE.
2) In the case of illustrations or tabular material, we require that the copyright line © [Year of original publication] IEEE appear prominently with each reprinted figure and/or table.
3) If a substantial portion of the original paper is to be used, and if you are not the senior author, also obtain the senior author's approval.

Requirements to be followed when using an entire IEEE copyrighted paper in a thesis:

1) The following IEEE copyright/ credit notice should be placed prominently in the references: © [year of original publication] IEEE. Reprinted, with permission, from [author names, paper title, IEEE publication title, and month/year of publication]
2) Only the accepted version of an IEEE copyrighted paper can be used when posting the paper or your thesis on-line.
3) In placing the thesis on the author's university website, please display the following message in a prominent place on the website: In reference to IEEE copyrighted material which is used with permission in this thesis, the IEEE does not endorse any of [university/educational entity's name goes here]'s products or services. Internal or personal use of this material is permitted. If interested in reprinting/republishing IEEE copyrighted material for advertising or promotional purposes or for creating new collective works for resale or redistribution, please go to http://www.ieee.org/publications_standards/publications/rights/rights_link.html to learn how to obtain a License from RightsLink.

If applicable, University Microfilms and/or ProQuest Library, or the Archives of Canada may supply single copies of the dissertation.

BACK CLOSE WINDOW

The permission below is for the reproduction of material in Chapter 3.

CCC RightsLink

Home | Help | Email Support | Sign in | Create Account

IEEE Requesting permission to reuse content from an IEEE publication

From Event Data to Wind Power Plant DQ Admittance and Stability Risk Assessment

Author: Zhengyu Wang
Publication: IEEE Transactions on Power Systems
Publisher: IEEE
Date: Dec 31, 1969

Copyright © 1969, IEEE

Thesis / Dissertation Reuse

The IEEE does not require individuals working on a thesis to obtain a formal reuse license, however, you may print out this statement to be used as a permission grant:

Requirements to be followed when using any portion (e.g., figure, graph, table, or textual material) of an IEEE copyrighted paper in a thesis:

1) In the case of textual material (e.g., using short quotes or referring to the work within these papers) users must give full credit to the original source (author, paper, publication) followed by the IEEE copyright line © 2011 IEEE.
2) In the case of illustrations or tabular material, we require that the copyright line © [Year of original publication] IEEE appear prominently with each reprinted figure and/or table.
3) If a substantial portion of the original paper is to be used, and if you are not the senior author, also obtain the senior author's approval.

Requirements to be followed when using an entire IEEE copyrighted paper in a thesis:

1) The following IEEE copyright/ credit notice should be placed prominently in the references: © [year of original publication] IEEE. Reprinted, with permission, from [author names, paper title, IEEE publication title, and month/year of publication]
2) Only the accepted version of an IEEE copyrighted paper can be used when posting the paper or your thesis on-line.
3) In placing the thesis on the author's university website, please display the following message in a prominent place on the website: In reference to IEEE copyrighted material which is used with permission in this thesis, the IEEE does not endorse any of [university/educational entity's name goes here]'s products or services. Internal or personal use of this material is permitted. If interested in reprinting/republishing IEEE copyrighted material for advertising or promotional purposes or for creating new collective works for resale or redistribution, please go to http://www.ieee.org/publications_standards/publications/rights/rights_link.html to learn how to obtain a License from RightsLink.

If applicable, University Microfilms and/or ProQuest Library, or the Archives of Canada may supply single copies of the dissertation.

BACK CLOSE WINDOW

The permission below is for the reproduction of material in Chapter 3.

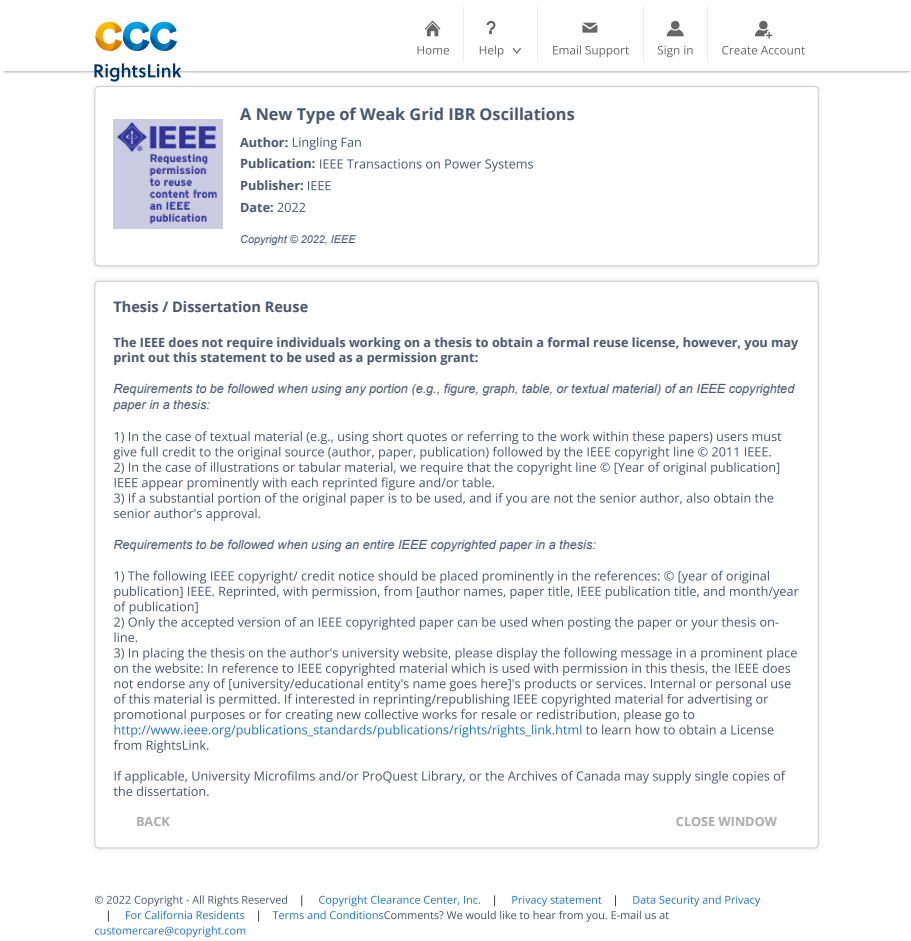

CCC RightsLink

Home | Help | Email Support | Sign in | Create Account

IEEE Requesting permission to reuse content from an IEEE publication

A New Type of Weak Grid IBR Oscillations

Author: Lingling Fan
Publication: IEEE Transactions on Power Systems
Publisher: IEEE
Date: 2022

Copyright © 2022, IEEE

Thesis / Dissertation Reuse

The IEEE does not require individuals working on a thesis to obtain a formal reuse license, however, you may print out this statement to be used as a permission grant:

Requirements to be followed when using any portion (e.g., figure, graph, table, or textual material) of an IEEE copyrighted paper in a thesis:

1) In the case of textual material (e.g., using short quotes or referring to the work within these papers) users must give full credit to the original source (author, paper, publication) followed by the IEEE copyright line © 2011 IEEE.
2) In the case of illustrations or tabular material, we require that the copyright line © [Year of original publication] IEEE appear prominently with each reprinted figure and/or table.
3) If a substantial portion of the original paper is to be used, and if you are not the senior author, also obtain the senior author's approval.

Requirements to be followed when using an entire IEEE copyrighted paper in a thesis:

1) The following IEEE copyright/ credit notice should be placed prominently in the references: © [year of original publication] IEEE. Reprinted, with permission, from [author names, paper title, IEEE publication title, and month/year of publication]
2) Only the accepted version of an IEEE copyrighted paper can be used when posting the paper or your thesis on-line.
3) In placing the thesis on the author's university website, please display the following message in a prominent place on the website: In reference to IEEE copyrighted material which is used with permission in this thesis, the IEEE does not endorse any of [university/educational entity's name goes here]'s products or services. Internal or personal use of this material is permitted. If interested in reprinting/republishing IEEE copyrighted material for advertising or promotional purposes or for creating new collective works for resale or redistribution, please go to http://www.ieee.org/publications_standards/publications/rights/rights_link.html to learn how to obtain a License from RightsLink.

If applicable, University Microfilms and/or ProQuest Library, or the Archives of Canada may supply single copies of the dissertation.

BACK CLOSE WINDOW

About the Author

Zhengyu Wang was born in 1994; Nanjing, China. He received his bachelor's degree in Eletrical Engineering from the Iowa State University in 2017. He obtained the Master of Science degree in Electrical Engineering from the University of South Florida in 2019 while pursuing Ph.D. degree from Fall 2017. His research focus is the study and analysis of inverter-based renewable energy resources and devices includes dynamic modeling, hardware testbed experiments, data-driven system identification, stability analysis, and etc.